MATERIALS AND STRATEGIES FOR FLEXIBLE, STRETCHABLE AND LARGE AREA PHOTONIC DEVICES

BY

LI GAO

DISSERTATION

Submitted in partial fulfillment of the requirements
for the degree of Doctor of Philosophy in Materials Science and Engineering
in the Graduate College of the
University of Illinois at Urbana-Champaign, 2014

Urbana, Illinois

Doctoral Committee:

Professor John A. Rogers, Chair, Director of Research
Professor Paul V. Braun
Assistant Professor Shen J. Dillon
Professor Xiuling Li

ABSTRACT

Various electronic devices have been realized in flexible and stretchable formats that can open up huge applications in biomedical industry. Other than electronic signals, photons can also interact with matters intensely and provide valuable information about the underlying substrates and immediate medium. However, photonic components have been rarely demonstrated in a flexible and stretchable format, due to the complicated fabrication process and rigid substrates involved in most photonic devices. The photonic device function is limited when flexibility and curvature features are requested in operation, and they also have rare applications as epidermal sensors. This dissertation aim to demonstrate functional photonic devices in a flexible and stretchable format by using unconventional fabrication techniques such as soft nanoimprint lithography and nanotransfer printing etc. One example is fabricating flexible, large area, multilayerd negative index metamaterials which are unattainable with conventional fabrication techniques and have high figure of merit in the visible range of operation. Optical modeling by finite domain time domain simulations will be incorporated to achieve optimized device design. Similarly, large area and highly stretchable plasmonic nanoparticle arrays will be obtained to show large resonance tuning for the first time with unusual three dimensional buckled structure beyond critical strain. The mechanics and plasmonic resonance associated with such large strains will be investigated by both experiment and analytical modeling. Another example is to design novel schemes for stretchable thermochromic liquid crystal sensors that have excellent mechanical property and are well-suited for high precision epidermal thermographic applications.

ACKNOWLEDGEMENTS

I have been extremely fortunate to come to University of Illinois and can never express my gratitude adequately to my advisor Professor John A. Rogers, who has given me the opportunity to take a fantastic research journey with him and all the brilliant people in the group. Professor Rogers has offer generous support and guidance during these years, without whom my graduate work on the flexible and stretchable photonics would never become possible, I could not have asked for a better advisor and research experience which I will cherish for my entire life. I am also extremely grateful to Professor Yonggang Huang, Dr. Yihui Zhang and Professor Debashis Chanda who have provided invaluable collaboration and guidance in the mechanics and optics associated in my research topic. They have developed many theoretical models that comprise many chapters of this dissertation. I would give sincere thanks to my committee members, Professor Paul V. Braun, Professor Xiuling Li and Professor Shen J. Dillon, for their important comments and advice. I would also thank all my group members and the staff in Materials Science and Engineering Department, Frederick Seitz Materials Research Laboratory, Micro and Nanotechnology Laboratory and Beckman Institute, for their kind help and expertise provided though the years.

Finally, I would like to thank my husband Dr. Xinran Wang. It has been destiny that brought us together in Illinois and all his love and support warmed me through my Ph.D journey. I am also very grateful for having our son Yifan Wang come to our life and bring us countless joys. Lastly, thanks to my mom Suzhi Xie, who has been the most wonderful

person to me in the world, gave me everything she could to get me through my education and life.

TABLE OF CONTENTS

CHAPTER 1

INTRODUCTION

1.1 Negative Index Metamaterials

Negative index metamaterials (NIMs) are engineered structures that exhibit negative permeability $\mu = \mu' + i\mu''$ and permittivity $\varepsilon = \varepsilon' + i\varepsilon''$ satisfy $\varepsilon'\mu'' + \varepsilon''\mu' < 0$, potential device applications are superlens, eletromagnetic cloaking and perfect absorber etc. Some of these potential applications would require certain flexibility and device curvature to focus light or guide light around curvilinear objects. In the past decade, various important classes of NIMs have been experimentally demonstrated, with operation in the microwave regime [1, 2], at terahertz frequencies [3, 4] and optical wavelengths [5-9]. Fishnet geometry is one of the most attractive designs for visible wavelength operation with high figures of merit (low loss). Nanotransfer printing (nTP) [9] has been developed recently to realize flexible, multilayered NIMs that operate in telecommunication band with large-area and high-throughput capability. However, it is quite challenging to use the same technique to scale down the fishnet unit sizes and achieve negative index of refraction in the visible wavelength regime.

A critical step in this type of fabrication involves collimated physical vapor deposition (PVD) of alternating layers of metals and dielectrics onto substrates with features of relief that define the fishnet layouts. Detailed mechanisms for film growth depend strongly on materials properties, such as surface mobility, sticking coefficient,

crystallinity and grain structure [10, 11] and on conditions for deposition, such as rate and base pressure. A behavior of particular relevance here is that the films grow often in a direction that is not entirely perpendicular to the patterned substrate surface (stamp), even for normally incident flux of material. As a result, angled sidewall profiles develop at the edges of deposits near features of relief on the substrate. For the case of NIMs that consist of multilayer stacks of silver (Ag) and magnesium fluoride (MgF_2) formed by nTP for operation in the NIR, the sidewall slopes are 6–12 ° [9] depending on deposition conditions. For operation in the visible, however, the required dimensions of the openings in the fishnet structures can be as small as 200 nm [12-14]. As shown subsequently, in such cases, angular growth can lead to substantial or even complete elimination of the fishnet geometry at the top surfaces of the multilayer stacks. In this dissertation, two approaches based on nanoimprint lithography (NIL) technique (chapter 2) and nanotransfer printing (nTP) technique (chapter 3) with improved materials growth condition would be introduced to obtain flexible, large area NIMs that can operate in visible regime with unit cell size down to 300nm.

1.2 Stretchable Plasmonic Nanodot Array

Plasmonics takes advantage of the coupling of light to charges like electrons in metals, and allows breaking the diffraction limit for the localization of light into subwavelength dimensions enabling strong field enhancements. They have found extensive applications in biosening and Surface Enhanced Raman Spectroscopy (SERS) etc. Recent advances have realized flexible, stretchable plasmonic nanoparticle array by

self-assembled gold nanoparticle array [15, 16] or irregular nanoaggregates [17] transferred onto elastomeric substrates, or by using nano-stencil lithography where plasmonic materials are deposited through small openings in the stencil mask onto elastomeric substrates [18]. These techniques have enabled stretchability up to 30-40%, however, they are still limited to small area, irregular or sparse nanoparticle array geometry which is less effective in achieving plasmonic coupling and tuning. Practical applications of such devices have been demonstrated for SERS recently [17, 20] and more discussion of the related field can be found a recent perspective [21]. New concept of conformal surface plasmons (CSPs), surface plasmon waves that can propagate on ultrathin and flexible films to long distances in a wide broadband range from microwave to mid-infrared frequencies have been also introduced [22]. This subject has become important in the last couple of years, however, large stretchability and tunability are still missing; detailed study of the nanoparticle array deformation and its effect on the resonance has also not been investigated. In chapter 4, we will report a simple and powerful technique based on the soft lithography and physical lift-off technique to form ultra large area; highly dense nanoparticle array on elastomeric substrates that are able to achieve reversible stretchability over 100%, and show good stretch induced plasmonic anisotropy and enhanced interparticle interactions.

1.3 Stretchable Liquid Crystal Array for Thermography

Spatio-temporal imaging of skin temperature offers experimental and investigational value for detection of breast cancers and other syndromes, as an adjunctive

screening tool to mammography [23-25]. The required milli-Kelvin levels of precision and milli-meter scale resolution are most commonly achieved by use of sophisticated infrared digital imaging cameras. Widespread adoption of such technology is limited, however, by high capital costs, motion artifacts, and inability for use outside of clinical or laboratory settings. Low cost liquid crystal thermography techniques has been exploited much earlier, for potential screening of deep venous thrombosis [26-29], breast cancer [30-32], spinal root syndromes [33, 34], chronic back pain [35] and even pulmonological diagnostics [36]. Recent work [37, 38] demonstrates that electronic temperature evaluation and mapping devices can be constructed in ultathin, soft and compliant formats, sometimes referred to as 'epidermal' due to the similarity of the physical characteristics to the skin itself. Such systems offer impressive capabilities that bypass many limitations of infrared cameras, but provide only modest spatial resolution and imaging fidelity, limited by multiplexing systems needed to address large sensor arrays.

In chapter 5, we will introduce an alternative scheme that combines colorimetric temperature indicators with wireless stretchable electronics to produce an epidermal device for precision mapping of thermal characteristics of the skin. The colorimetric temperature indicators are thermochromic liquid crystals (TLC), with increasing temperature, the phase varies from crystalline solid to sematic, cholestoric and, finally, isotropic liquid, all over a range of a few degrees, dictated by the chemistry [39, 40]. In the cholestoric phase, light that reflects from the TLC pixels spans a narrow wavelength range defined by phase coherent interactions with the liquid crystal assemblies. Increases in temperature decrease the pitch, thereby leading to blue-shifts in the peak wavelengths of this reflected light. This

behavior provides the basis for colorimetric optical readout. Other phases have no chiral nematic orientation of molecular planes and thus do not yield any strong wavelength dependence to the reflection. Co-integration with electronics provides a means for controlled, local heating by RF signals, to enable not only mapping of temperature but also intrinsic thermal constitutive properties. Uniform layers of TLCs in water impermeable, non-stretchable thick plastic sheaths, and without electronics, have been explored for skin thermography[41-43] but without the ability to conform sufficiently well to the curved, textured surface of the skin for accurate, reproducible measurements. Such devices also frustrate transepidermal water loss. They also thermally load the skin and cause irritation at the skin interface, thereby preventing reliable, accurate evaluation or use in continuous modes over long periods of time. Thermochromic textiles are available for cosmetic and fashion purposes [44-46] but their inability to maintain intimate contact with the skin and the limited capacity to use known thermochromic dyes for precision temperature evaluation prevent their use in the sorts of applications envisioned here. The devices reported in chapter 5 not only avoid these drawbacks but they also allow precise measurement of thermal conductivity and thermal diffusivity through analysis of spatio-temporal images obtained during operation of integrated RF components. Conventional digital cameras and RF transmission systems enable simultaneous readout of thousands of pixels at resolutions that exceed those needed to image temperature and thermal property variations on the skin. The epidermal format induces minimal perturbations on the natural mechanical and thermal properties of the skin. Results presented in the following establish the foundational aspects in materials, mechanics and thermal physics for both electronically active and passive epidermal TLC (e-TLC) devices, including algorithms for extracting precision, calibrated data from

colour digital images. Demonstrations in reactive hyperaemia assessments of blood flow, as it relates to cardiovascular health, and hydration analysis, as it relates to skin-care, provide two examples of use in clinically meaningful tests.

1.4 References

1. Shelby, R. A., Smith, D. R. & Schultz, S. Experimental verification of a negative index of refraction. *Science* **292**, 77–79 (2001).
2. Schurig, D. *et al.* Metamaterial Electromagnetic Cloak at Microwave Frequencies. *Science* **314**, 977-980 (2006).
3. T. J. Yen *et al.* Terahertz magnetic response from artificial materials. *Science* **303**, 1494-1496 (2004).
4. Paul, O., Imhof, C., Reinhard, B., Zengerle, R. & Beigang, R. Negative index bulk metamaterial at terahertz frequencies. *Opt. Express* **16**, 6736-6744 (2008).
5. Dolling, G., Enkrich, C. & Wegener, M. Low-loss negative-index metamaterial at telecommunication wavelengths. *Opt. Lett.* **31**, 1800-1802 (2006).
6. Zhang, S. *et al*. Optical negative-index bulk metamaterials consisting of 2D perforated metal-dielectric stacks. *Opt. Express* **14**, 6778–6787 (2006).
7. Shalaev, V. M. Optical negative-index metamaterials. *Nat. Photonics* **1**, 47 (2007).
8. Soukoulis, C. M., Linden, S. & Wegener, M. Negative refractive index at optical frequencies. *Science* **315**, 47-49 (2007).
9. Chanda, D. *et al.* Large-area flexible 3D optical negative index metamaterial formed by nanotransfer printing. *Nature Nanotechnol.* **6**, 402-407 (2011).

10. Hawkeye, M. M. & Brett, M. J. Glancing angle deposition: Fabrication, properties, and applications of micro- and nanostructured thin films. *J. Vac. Sci. Technol. A* **25**, 1317-1335 (2007).
11. Dirks, A. G. & Leamy, H. J. Columnar microstructure in vapor-deposited thin-films. *Thin Solid Films* **47**, 219-233 (1977).
12. Xiao, S. M., Chettiar, U. K., Kildishev, A. V., Drachev, V. P. & Shalaev, V. M. Yellow-light negative-index metamaterials. *Opt. Lett.* **34**, 3478-3480 (2009).
13. Dolling, G., Wegener, M., Soukoulis, C. M. & Linden, S. Negative-index metamaterial at 780 nm wavelength. *Opt. Lett.* **32**, 53-55 (2007).
14. Chettiar, U. K. *et al.* Dual-band negative index metamaterial: double negative at 813nm and single negative at 772nm. *Opt. Lett.* **32**, 1671-1673 (2007).
15. Chiang, Y.-L. *et al.* Mechanically tunable surface plasmon resonance based on gold nanoparticles and elastic membrane polydimethylsiloxane composite. *Appl. Phys. Lett.* **96**, 041904 (2010).
16. Millyard, M. G. *et al.* Stretch-induced plasmonic anisotropy of self-assembled gold nanoparticle mats. *Appl. Phys. Lett.* **100**, 073101 (2012).
17. Hossain, M. K., Willmott, G. R., Etchegoin, P. G., Blaikie, R. J. & Tallon, J. L. Tunable SERS using gold nanoaggregates on an elastomeric substrate. *Nanoscale* **5**, 8945-8950 (2013).
18. Aksu, S. *et al.* Flexible Plasmonics on Unconventional and Nonplanar Substrates. *Adv. Mater.* **23**, 4422 (2011).

19. Vazquez-Mena, O. *et al.* High-Resolution Resistless Nanopatterning on Polymer and Flexible Substrates for Plasmonic Biosensing Using Stencil Masks. *ACS Nano* **6**, 5474-5481 (2012).

20. Kang, H., Heo, C.-J., Jeon, H. C., Lee, S. Y. & Yang, S.-M. Durable Plasmonic Cap Arrays on Flexible Substrate with Real-Time Optical Tunability for High- Fidelity SERS Devices. *ACS Appl. Mater. Interfaces* **5**, 4569-4574 (2013).

21. Polavarapu, L. & Liz-Marzan, L. M. Towards low-cost flexible substrates for nanoplasmonic sensing. *Phys. Chem. Chem. Phys.* **15**, 5288-5300 (2013).

22. Shen, X., Cui, T. J., Martin-Cano, D. & Garcia-Vidal, F. J. Conformal surface plasmons propagating on ultrathin and flexible films. *P. Natl. Acad. Sci USA.* **110**, 40-45 (2013).

23. Arora, N. *et al.* Effectiveness of a noninvasive digital infrared thermal imaging system in the detection of breast cancer. *Am. J. Surg.* **196**, 523-526 (2008).

24. Kennedy, D. A., Lee, T. & Seely, D. A Comparative Review of Thermography as a Breast Cancer Screening Technique. *Integr. Cancer. Ther.* **8**, 9-16 (2009).

25. Kerr, J. Review of the effectiveness of infrared thermal imaging (thermography) for population screening and diagnostic testing of breast cancer. *NZHTA Tech Brief Series* **3** (2004).

26. Cameron, E. W., Sachdev, D., Gishen, P. & Martin, J. F. Liquid-crystal thermography as a screening-test for deep-vein thrombosis in patients with cerebral infarction. *Eur. J. Clin Invest.* **21**, 548-550 (1991).

27. Kohler, A., Hoffmann, R., Platz, A. & Bino, M. Diagnostic value of duplex ultrasound and liquid crystal contact thermography in preclinical detection of deep

vein thrombosis after proximal femur fractures. *Arch. Orthop. Trauma Surg.* **117**, 39-42 (1998).

28. Pochaczevsky, R., Pillari, G. & Feldman, F. Liquid crystal contact thermography of deep venous thrombosis. *AJR. Am. J. Roentgenol.* **138**, 717-723 (1982).
29. Thomas, E. A., Cobby, M. J. D., Davies, E. R., Jeans, W. D. & Whicher, J. T. Liquid-crystal thermography and c-reactive protein in the detection of deep venous thrombosis. *Brit. Med. J.* **299**, 951-952 (1989).
30. Bakan, J. A. & Schaab, C. K. Liquid-crystal microcapsule medical device used for thermographic examination of the human female breast. *Appl. Biochem. and Biotech.***10**, 289-299 (1984).
31. Davison, T. W. *et al.* Detection of breast-cancer by liquid-crystal thermography - preliminary report. *Cancer* **29**, 1123-&, (1972).Pochaczevsky, R. & Meyers, P. H. Vacuum contoured, liquid-crystal, dynamic breast thermoangiography as an aid to mammography in the detection of breast- cancer. *Clin. Radiol.* **30**, 405-411 (1979).
32. Pochaczevsky, R. The value of liquid-crystal thermography in the diagnosis of spinal root compression syndromes. *Orthop. Clin. N. Am.* **14**, 271-288 (1983).
33. Pochaczevsky, R., Wexler, C. E., Meyers, P. H., Epstein, J. A. & Marc, J. A. Liquid-crystal thermography of the spine and extremities - its value in the diagnosis of spinal root syndromes. *J. Neurosurg.* **56**, 386-395 (1982).
34. Newman, R. I., Seres, J. L. & Miller, E. B. Liquid-crystal thermography in the evaluation of chronic back pain - a comparative-study. *Pain* **20**, 293-305 (1984).
35. Klosowicz, S. J., Jung, A. & Zuber, J. in *Optical Sensing for Public Safety, Health, and Security* Vol. 4535 *P. Soc. Photo-Opt. Inst.* 24-29 (2001).

36. Kim, D.-H. *et al.* Epidermal Electronics. *Science* **333**, 838-843 (2011).

37. Webb, R. C. *et al.* Ultrathin conformal devices for precise and continuous thermal characterization of human skin. *Nat. Mater.* **12**, 1078-1078 (2013).

38. Dolphin, D., Muljiani, Z., Cheng, J. & Meyer, R. B. Low-temperature chiral nematic liquid-crystals derived from beta-methylbutylaniline. *J. Chem. Phys.* **58**, 413-419 (1973).

39. Sage, I. *et al.* Thermochromic liquid crystals. *Liq. Cryst.* **38**, 1551-1561 (2011).

40. Brull, S. J. *et al.* Comparison of crystalline skin temperature to esophageal temperatures during anesthesia. Anesthesiology 73, A472 (1990).

41. Ikeda, T. et al. Influence of thermoregulatory vasomotion and ambient temperature variation on the accuracy of core-temperature estimates by cutaneous liquid crystal thermometers. *Anesthesiology* **86**, 603 (1997).

42. Wisniewski, C. M. A comparison of esophageal temperature readings and liquid crystal temperature readings in the pediatric population. *CRNA Masters Thesis*, Virginia Commonwealth Univ. (1991).

43. Aitken, D. et al. Textile applications of thermochromic systems. *Rev. Prog. Coloration* **26**, 1–8 (1996).

44. Chowdhury, M. A. et al. Application of thermochromic colorants on textiles: temperature dependence of colorimetric properties. *Color. Technol.* **129**, 232–237 (2012).

45. Chowdhury, M. A. et al. Photochromic and thermochromic colorants in textile applications. *J. Eng. Fiber. Fabr.* **9**, 107–123 (2014).

CHAPTER 2

NANOIMPRINTING TECHNIQUES FOR LARGE-AREA FLEXIBLE NEGATIVE INDEX METAMATERIALS WITH OPERATION IN THE VISIBLE BAND

2.1 Introduction

Nanoimprint lithography (NIL) [1-3] is capable of forming small dimension 3D visible NIMs when performed with an additional subtractive, physical liftoff processing step. The scheme is related to those that reported based on nanotransfer printing (nTP) [4], but with significantly improved properties, and ability to realize structures with high figure of merit operation at wavelengths deeper into the visible than those possible with many other approaches [4-10]. NIL has been used in the past with standard lift-off processes to fabricate single layer, or 2D, metamaterials [11]. 3D multi-layer metamaterials are different and demand different approaches that utilize NIL with physical liftoff as a route to such 3D metamaterials. The overall sizes of the 3D NIMs and the fabrication throughputs and more than ten million (10^7) times larger than those based on focused ion beam milling [9, 10], and are comparable to those enabled by nTP. [4] In particular, this past work used a multi-layer metal/dielectric stack grown on a stamp, with subsequent printing of this structure to a target substrate. The process in NIL is different, but complementary, in which an imprinted polymeric pattern serves as scaffold to grow 3D material stacks. This scheme does not involve any transfer printing step. Instead, the shape of the pattern is governed by interstitial space of the imprinted scaffold. Material grown on top of the scaffold is removed and discarded using a physical lift-off process. By comparison to nTP [4], however, the methods introduced here offer

improved robustness in operation, primarily because the stack remains untouched throughout the process; only unwanted material is removed from the top of the scaffold. The process flow is quite different, in a way that enables significantly smaller dimensions, and higher yields than previously possible. Improved resolution over large areas (> 4 cm^2), with high figure of merit (low loss) for visible bands represent key advances.

2.2 Experiments

2.2.1 An Overview of Device Fabrication Scheme

Nanoimprint lithography, as used here, offers advantages over other fabrication options in terms of low-cost, high-throughput, and reliable scalability of pattern size without processing steps like exposure, development, or etching. A simple modification of NIL, involving a physical liftoff process, enables large-area composite metal/dielectric structures in multilayer fishnet geometries for a class of NIMs, often referred to as 3D-NIMs. The steps for fabrication appear in **Figure 2.1**. The first involves a soft NIL process [1-3] with an elastomeric mold of poly(dimethylsiloxane) (PDMS) to form features of surface relief on a spin-cast photocurable pre-polymer (NOA63, Norland) (n =1.53; thickness ~1 μm) on a glass substrate. This implementation of NIL has been demonstrated to offer resolution that extends into the molecular size regime, i.e. 1-2 nm [12, 13]. The mold in this case presents a rectangular grid pattern of narrow, raised regions with high aspect ratio, formed in a casting and curing process against a silicon master template formed by reactive ion etching with a mask of photoresist patterned by electron beam lithography. Passing ultraviolet light through the PDMS mold while it is in

contact with the liquid pre-polymer cures the material into a solid form with relief in a pattern of rectangular posts in a rectangular array (i.e. the inverse geometry of the relief on the PDMS). Peeling the PDMS away completes the NIL process. The lateral dimensions of the raised regions on the PDMS, which ultimately define the dimensions of the bars in the fishnet NIMs are shown in **Figure 2.2**, W_Y and W_X are both 120 nm, and P is 300 nm and 400 nm for NIMs that operate in the visible (VIS) band, obtained from finite difference time domain (FDTD) simulations. Next, a thin protective layer of fluorocarbon CF_n is introduced with C_4F_8 fluorination step [14] to reduce the adhesion between the polymer template and deposited materials. Collimated deposition of 11 alternating layers of silver (Ag, 35 nm) and magnesium fluoride (MgF_2, 15 nm) by electron beam evaporation onto the nanoimprinted polymer forms physically separated multilayer stacks on the raised and recessed regions. A bilayer of Ti (5 nm) and SiO_2 (30 nm) evaporated on top of these stacks prepares the substrate for the next step of the fabrication, which is critically important in the scheme described here. Here, contact of a uniform slab of PDMS activated to generate hydroxyl functionality on its surface leads to condensation reactions that bond the PDMS to the SiO_2, to yield strong adhesion. Physically peeling the PDMS away removes selectively the multilayer stacks on the raised regions. The result of this subtractive, physical liftoff process is a fishnet NIM structure, corresponding to multilayers deposited only into the recessed areas. As a final procedure, oxygen plasma etching removes the polymer posts that exist in the holes of this mesh. The key distinction of this approach, compared to the nTP process described previously, is that the materials that form the 3D-NIMs are not manipulated by transfer. This difference leads to improved yields and resolution.

2.2.2 Detailed Experiment Steps

The silicon daughter master pattern was etched using a Bosch process (94mTorr, etch/passivation: cycle time, 5 s/5 s; RIE power, 20 W/0W; SF_6/C_4F_8 flow rate, 35 sccm/110 sccm for constant ICP power of 600 W; etch rate 1 μm/80 s) with SF6 gas, to a depth between 600 and 700 nm, through a combination of Si_3N_4 layer and photoresist mask formed by soft nanoimprint lithography. Controlling the etching conditions allowed variation of fishnet line widths (Wx and Wy). The original large-area master pattern was defined on a silicon wafer by deep ultraviolet projection mode photolithography and electron beam lithography for telecom and visible band, respectively. Use of electron beam lithography and glass etching methods employed by Photronics Inc. allows for larger structures with fine feature size to be more easily fabricated. Leveraging current nfrastructure for the semiconductor industry reduces development costs for proof of concept. The molds for this process consisted of elements of PDMS (Dow Corning, Sylgard) formed by casting and curing against the large area silicon master. Many molds can be produced from one silicon master.

We used a commercially available photocurable polyurethane material (NOA 63, Norland Inc.) for the NIL resist. A liquid prepolymer of this material was drop-cast onto a clean glass substrate. Next, a high aspect ratio PDMS mold was pressed against the liquid, and any trapped bubbles were allowed to permeate through the PDMS. Passing UV light (Osram Sylvania 100 W MV PAR38, power density 8.4 mW/cm^2) through the

PDMS while in contact with the NOA for 1 h cures the NOA into a solid form. The PDMS mold was then peeled away to complete the NIL process. Next, the imprinted NOA was fluorinated by exposure to C_4F_8 in an ICP-RIE system (SPTS Inc., RIE power = 0 W, ICP power = 600 W, 15 s, chamber pressure = 94 mTorr, C4F8 flow rate = 110 sccm) which formed a crosslinked polymer on the surface to reduce the surface adhesion.

Multilayer stacks were deposited using a Temescal (FC-1800) six-pocket electron beam evaporation system. For optimal collimation, a small filament (6 mm) was used; the sample was mounted perpendicular to the flux from the source, and the distance between the sample and source was maximized (~2 ft). For deposition of Ag, MgF_2, Ti, and SiO_2, average chamber base pressures of 1.5 $x10^6$ Torr and deposition rates f 0.1-0.15 nm/s were found to yield the best results.

A low modulus, tacky form of PDMS, created by mixing in a 25:1 ratio by weight base and curing agent of a commercial material (Sylgard 184, Dow Corning), was used for the liftoff slab. The surface of this material was activated by exposing it to ozone created by deep ultraviolet light (BHK Inc., grid lamp, model 88-9102-02) for 3.5 min. Contact with the surface of multilayer stack condensation reactions between the hydroxyl groups on the PDMS and those on the top exposed layer of SiO_2 on the substrate led to strong adhesion. Peeling the PDMS away physically removes the stacks, in their entirety, from raised regions of the substrate. The NOA scaffold was removed by oxygen reactive ion etching (PlasmaLab Master Slave dualchamber reactive ion etcher, power = 50W,

pressure = 50 mTorr, flow rate = 50 sccm, time = 300 s). The results leave a fishnet multilayer stack at the recessed regions.

Transmission/reflection spectra were collected using a 4x-4x, 0.1 numerical aperture objective on an optical microscope (Hyperion 1000) coupled to a Fourier transform infrared spectrometer (Vertex 70) and outfitted with a spatial aperture with a diameter of 3.75 mm. Reflection spectra were normalized to a silver mirror with 96% reflectivity. Transmission spectra were normalized using a bare substrate.

Transmission and reflection spectra were calculated using experimental parameters for the printed 3D NIM structures, with commercial FDTD software package (Lumerical, Lumerical Solutions Inc.). A Drude model was used for the dielectric parameters of silver in the FDTD simulation, with a plasma frequency of 1.37×10^{16} s^{-1} and scattering frequency of 85×10^{12} s^{-1}. The scattering frequency was increased by a factor of 3 compared with that of bulk silver to account for the additional surface scattering loss. The FDTD simulations used averages of transmission/reflection separately computed with plane wave sources of TE and TM polarizations to compare with the unpolarized light used in the spectrometer. In particular, due to our present optics, our microscope-coupled FTIR system (Bruker Vertex 70-Huperion 1000) is capable of making high-quality transmission and reflection measurements without polarizer analyzer arrangement. To remain consistent with measurements, we used averaging of TE and TM polarization to achieve the response of an unpolarized light in FDTD simulation. These simulations used precise geometries extracted from images such as the one in Figure 2c and Figure 3c,

but without any line edge roughness (LER). The partial infiltration of openings in the mesh structure with adhesive material (NOA) used in the NIL process increases the background refractive index, ns. The effect moves the optical response to higher wavelength range compared to the case with air as the background medium. In the proposed technique, the 3D multilayer stack is embedded and supported inside a polymeric scaffold. An O_2 plasma etch removes the polymeric scaffold in the exposed regions. The effective index of the surroundings is defined by the polymer that remains. This value corresponds to ns. The best match between FDTD and experiment occurs between n_S = 1.2-1.3. We used n_S ~ 1.25 and 1.2 for telecom and visible bands respectively in the FDTD modeling (greater polymer infiltration inside larger open holes of telecom structure raises the background index by slightly larger number compared to visible case). These modeling results are consistent with those that use vertical sidewalls but depth-averaged dimensions. The good agreement between experiment and FDTD results, which assume ideal geometries and zero LER suggests that the observed losses are intrinsic to the materials. Slight variability in the dimensions of the structures, the properties of the constituent materials, and the levels of control (such as uniformity and edge roughness) associated with the fabrication are the probable causes of the 10-15% overall discrepancy between experimental observation and FDTD simulation.

2.3 Results and Discussions

The results of this simple process appear as SEM images in **Figure 2.2a-c**. The left set of images corresponds to the nanoimprinted polymer; the middle images show the sample after deposition of 11 layers of Ag/MgF_2 and a top bilayer of Ti/SiO_2; and the right set of images shows fishnet NIMs in the recessed regions of the nanoimprinted polymer, after physical liftoff of the top layers and removal of exposed polymer posts with reactive ion etching. The multilayer deposit shows expected angular growth (12-15 deg) [4, 15,16] such that stacks on the polymer posts exhibit mushroom-like shapes in which new layers sequentially overhang previous layers. Shadowing from the top layers leads to fishnet NIMs in the recessed regions, with sharply defined edges and overall trapezoidal cross sectional shapes. The base and top have $W_y = W_X = 120$ nm and $W_y = W_X \sim 15$ nm, respectively (**Fig. 2.2c**). These selections of line widths are based on engineered optical responses as described in the following section. As shown in the SEM images of **Fig. 2.2c**, the subtractive liftoff process yields well-defined fishnet NIMs with high levels of structural uniformity. Observed ~5-10% variations in fishnet line widths (W_X and W_y) arise primarily from variations in angular stack growth. Negligible line width variation arises from the NIL process. A corresponding VIS (P = 400 nm) sample (also large area (~6.5 cm^2) and with 11 layers) appears in **Fig. 2.2d** and corresponding micrograph images is shown in **Fig. 2.2e**. In such examples, the sample areas are limited only by the sizes of the PDMS molds, and not by any intrinsic constraint associated with the process. An important aspect of this fabrication scheme is that the

critical patterning step can be conducted with widely available, commercial tools for NIL, unlike the more specialized systems required for nanotransfer printing.

For the VIS structure, the design goal was to shift the negative index band deep into the visible wavelength range while maintaining high levels of transmission. Studies using FDTD indicate that both requirements scale together, i.e. narrower fishnet line width (W_X) enhances transmission and also the transmission peak moves to lower wavelength range due to excitation of symmetric plasmonic resonances at metal/dielectric interfaces as can be observed in **Figure 2.3a** and **Figure 2.3b** for P = 400 nm and P = 300 nm fishnets respectively. Experimentally, this type of operation can be achieved by reducing the line width ($W_X = W_Y = W_1$) of the fishnet scaffold by changing dimension of the NIL mold. Effects of angular growth limit the average stack line width W_{av} to 70 nm, corresponding to line widths of W_2 ~15 nm and W_1 ~120 nm at the top and the base of the structure, respectively (**Fig. 2.2c**). Optical characterization reveals broadband transmission peaks at 850 nm and 650 nm for 11-layer 3D fishnets with P = 400 nm and P = 300 nm, respectively, as shown in **Figure 2.3c**. Previous results indicate that at least 3 unit cells are needed to achieve a bulk-like negative index response [4, 17,18]. Hence, for the present case, 11-alternating metal/dielectric layers are sufficient to experimentally and computationally achieve a 3D metamaterial response.

$$\boldsymbol{n' = \pm\frac{1}{kd}Re[cos^{-1}(\frac{1-r^2+t^2}{2t})]} \quad (1)$$

$$\boldsymbol{n'' = \pm\frac{1}{kd}Im[cos^{-1}(\frac{1-r^2+t^2}{2t})]} \quad (2)$$

The real and negative part of the refractive index can be extracted by FDTD with the measured transmission and reflection data (equation 1 and 2) [19] indicates that the P = 300 nm structure has a negative index between 529 nm and 710 nm with a maximum of the real part Re (n) = -0.73 at a wavelength of 710 nm (**Fig. 2.3d**). The maximum negative index is achieved in the present case is -0.73 which indicates a group velocity that can exceed speed of light in free-space [10] due to the nature of wavelength dependent dispersion of the propagating mode. The losses for these types of structures are typically reported in terms of a figure of merit (FOM) defined by -Re (n)/Im (n). The material loss Im(n) can be estimated from the measured transmittance and reflectance data of assuming a single pass of light through the metamaterial, as $Im(n)=(\lambda/4\pi d)\ln[(1-R)/T]$. The maximum FOM for the visible (P = 300 nm) NIM is 4.3, as shown in **Figure 2.3e**. The wavelengths and the figures of merit are shorter and higher, respectively, than those previously achieved in related, multilayer 3D type NIMs [10].

The agreement between measured and FDTD predicted transmission (T) is excellent for the VIS sample (**Fig. 2.3c**) due to reduced impact of angular growth in the small feature sizes associated with this structure. There is no observed significant changes in transmission due to the presence of the substrate or the slight tapered geometry of the stack, consistent with previous results [10]. Hence, a bi-anisotropy coefficient of unity is used during parameter extraction. A key feature of the fabrication approaches described here is that they avoid etching steps that can otherwise lead to detrimental parasitic

effects associated with sidewall roughness and/or introduction of foreign chemical species.

2.4 Conclusions

The results described here demonstrate that simple NIL techniques, when combined with a physical liftoff process, provide access to large-area, high-quality 3D metamaterials. The reported NIMs operate in wavelength regimes shorter than those previously possible using nanotransfer printing, an alternative large-area patterning approach. The practical ease and wide availability of the NIL procedures and the liftoff processes, their ability to accommodate both critical feature sizes deep into the nanometer range and macroscale areas, and their compatibility with wide ranging classes of materials represent a combination of attributes that suggest a strong potential for use in both engineering development and exploratory research in fishnet and other emerging classes of metamaterials.

2.5 Figures

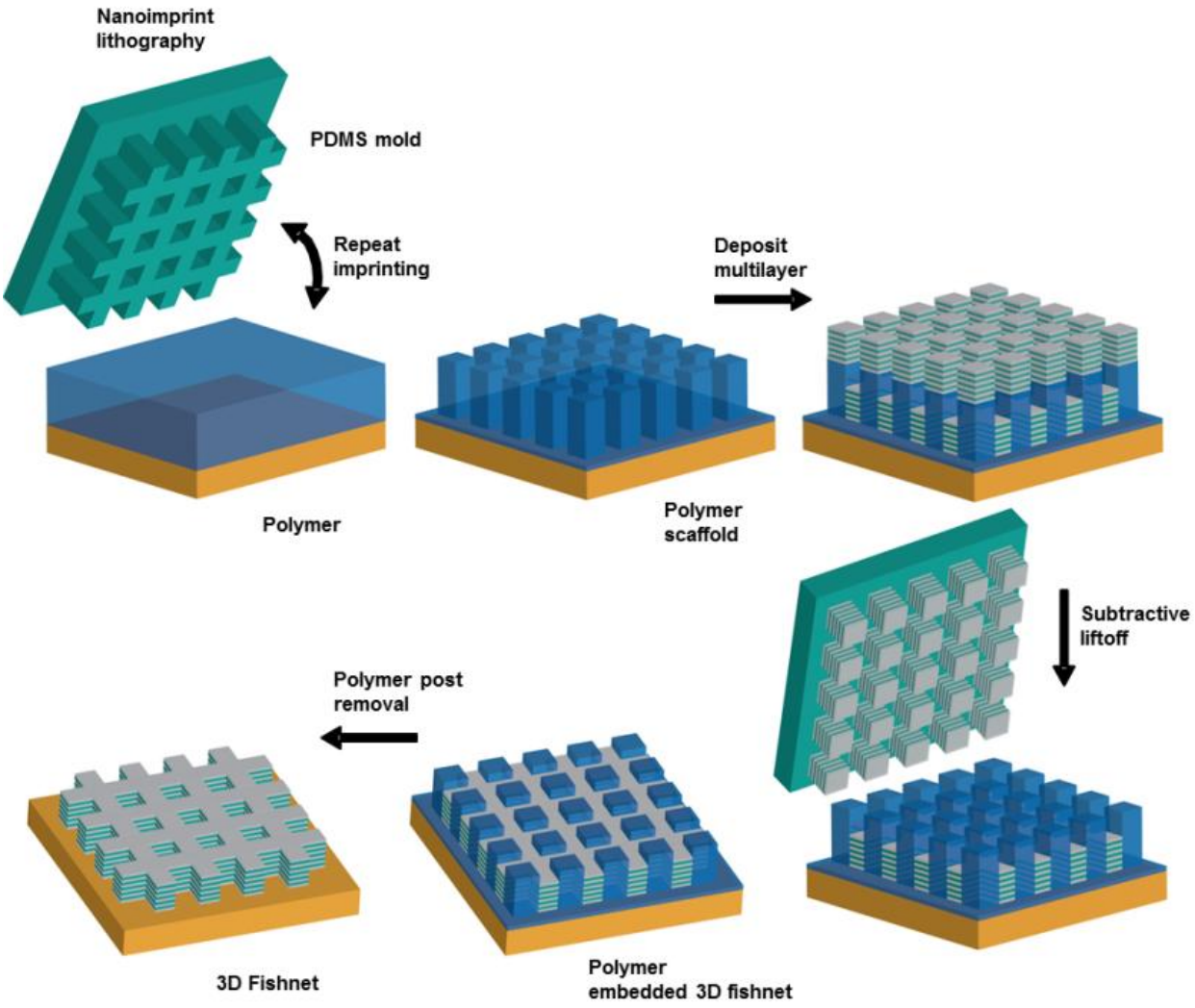

Figure 2.1 Fabricating large area 3D negative index metamaterials by combination of nanoimprint lithography and subtractive liftoff process. Schematic illustration of the steps for nanoimprint lithography and subtractive liftoff process.

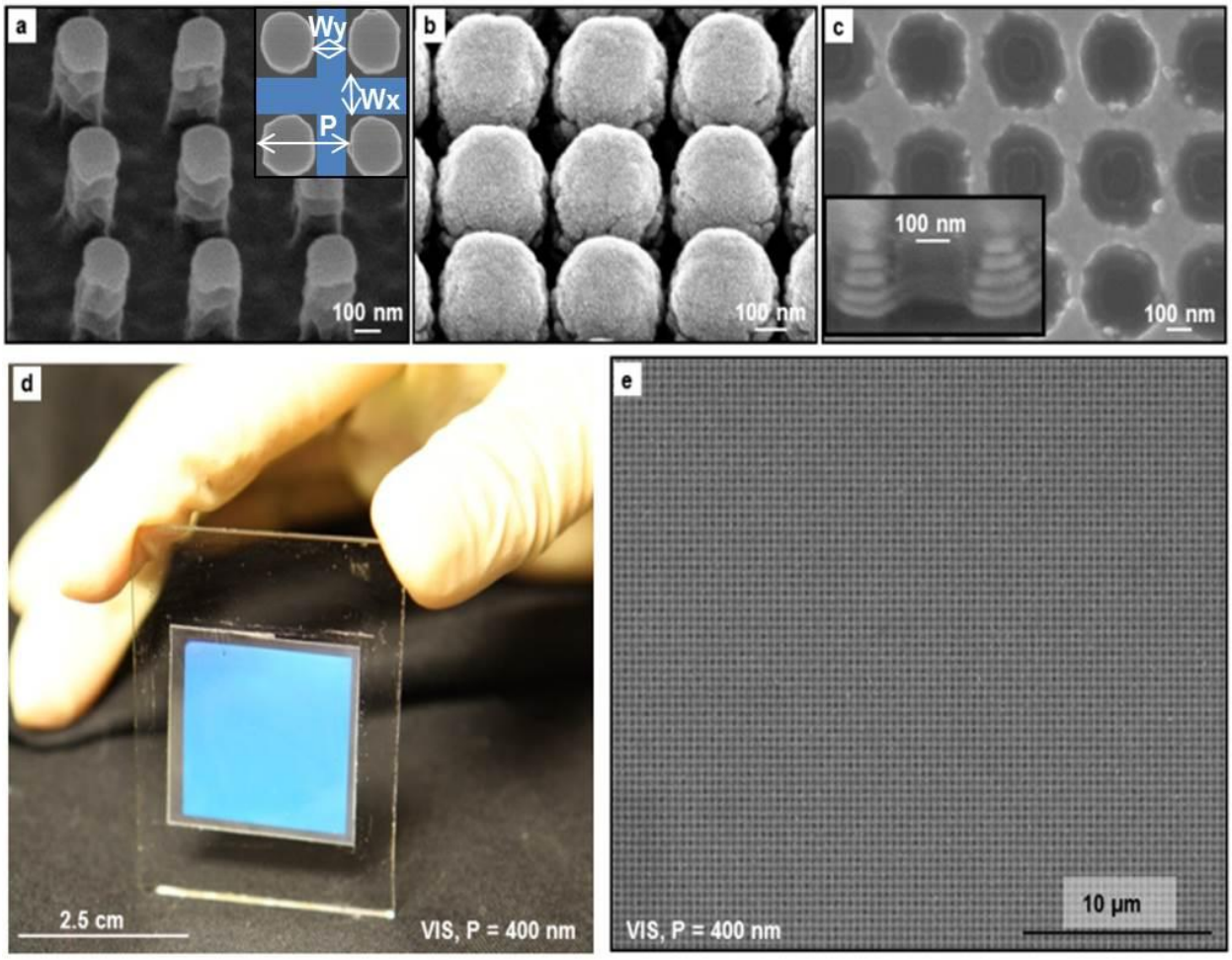

Figure 2.2 Large area visible 3D negative index metamaterial. Top view SEM image of nanoimprint lithography formed polymeric visible fishnet (P = 400 nm) (a) before deposition, (b) after deposition of 11-alternating layers of Ag/MgF_2 layers and (c) after removal of polymer posts, (c, inset) tilted view (52^0) SEM image of a stack of alternating layers of Ag and MgF_2 cross sectioned by FIB. Macroscopic optical image of a large (~2.5 cm x 2.5 cm) 3D NIM (d) and corresponding large area top view SEM is shown in (e).

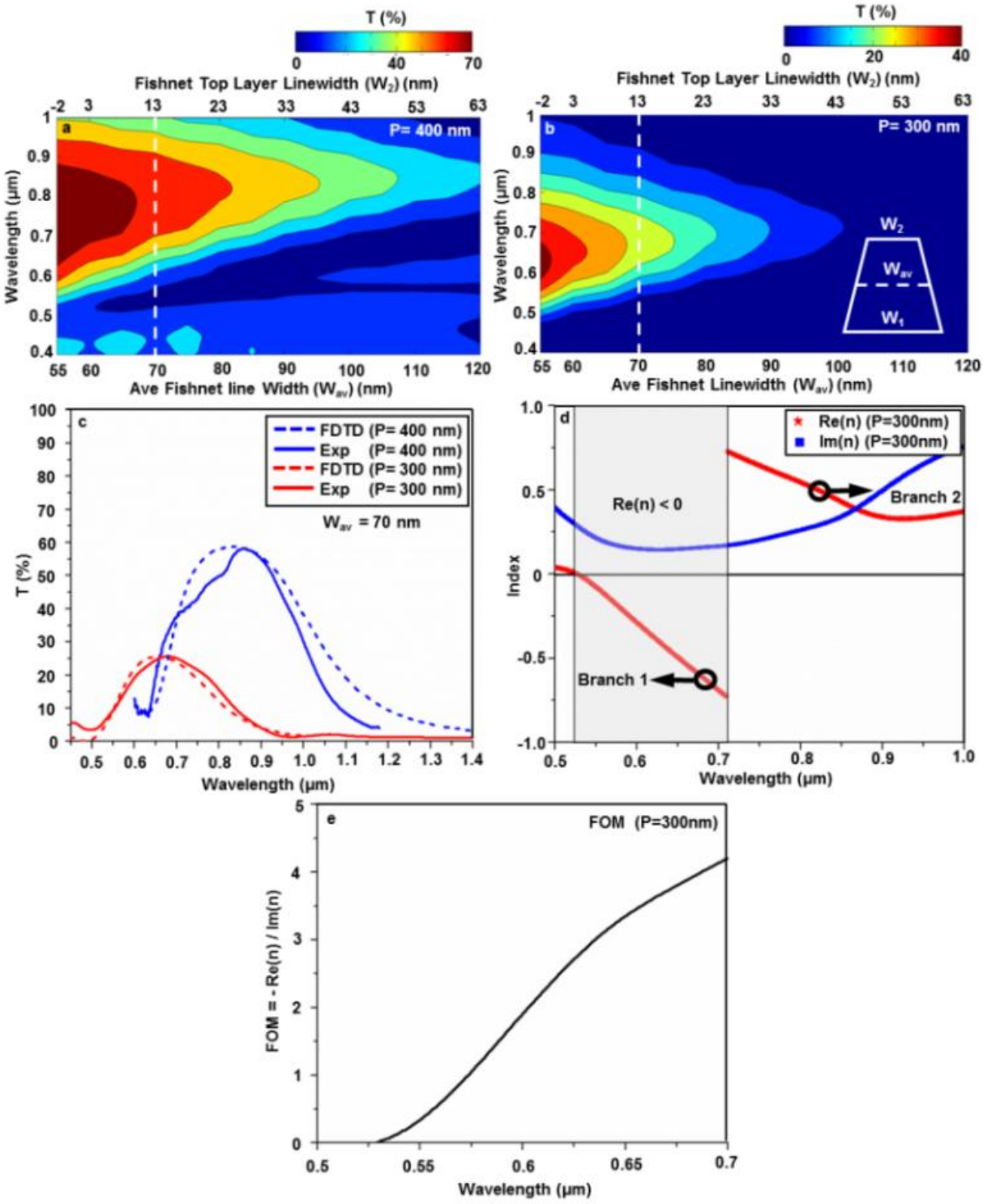

Figure 2.3 Experimental measurements and simulation results for transmission and refractive indices of 3D visible negative index metamaterials. FDTD predicted

(Fig. 2.3 continued) transmission as a function of depth averaged fishnet line width (W_{av}) for (a) P = 400 nm and (b) P = 300 nm. (c) FDTD predicted and experimentally measured transmission for the chosen depth averaged fishnet line width W_{av} = 70 nm and the corresponding (d) retrieved refractive indices and (e) FOM for P = 300 nm fishnet.

2.6 References

1. Chou, S. Y., Krauss, P. R. & Renstrom, P. J. Nanoimprint lithography. *J. Vac. Sci. Technol. B* **14**, 4129-4133 (1996).
2. Xia, Y., Rogers, J. A., Paul, K. E. & Whitesides, G. M. Unconventional Methods for Fabricating and Patterning Nanostructures. *Chem. Rev.* **99**, 1823-1848 (1999).
3. Gates, B. D., Xu, Q., Love, J. C., Wolfe, D. B. & Whitesides, G. M. Unconventional Nanofabrication. *Annu. Rev. Mater. Res.* **34**, 339-372 (2004).
4. Chanda, D. *et al.* Large-area flexible 3D optical negative index metamaterial formed by nanotransfer printing. *Nature Nanotechnol.* **6**, 402-407 (2011).
5. Dolling, G., Enkrich, C. & Wegener, M. Low-loss negative-index metamaterial at telecommunication wavelengths. *Opt. Lett.* **31**, 1800-1802 (2006).
6. Shalaev, V. M. Optical negative-index metamaterials. *Nat. Photonics* **1**, 47 (2007).
7. Soukoulis, C. M., Linden, S. & Wegener, M. Negative refractive index at optical frequencies. *Science* **315**, 47-49 (2007).
8. Dolling, G., Wegener, M. & Linden, S. Realization of a three-functional-layer negative-index photonic metamaterial. *Opt. Lett.* **32**, 551-553 (2007).

9. Valentine, J. *et al.* Three-dimensional optical metamaterial with a negative refractive index. *Nature* **455**, 376-380 (2008).

10. Garcia-Meca, C., Hurtado, J., Marti, J. & Martinez, A. Low-Loss Multilayered Metamaterial Exhibiting a Negative Index of Refraction at VisibleWavelengths. *Phys. Rev. Lett.* **106,** 067402 (2011).

11. W. Wu *et al.* Optical metamaterials at near and mid-IR range fabricated by nanoimprint lithography. *Appl. Phys. A* **87**, 143–150 (2007).

12. Hua, F. *et al.* Polymer Imprint Lithography with Molecular-Scale Resolution. *Nano Lett.* **4**, 2467-2471 (2004).

13. Hua, F. *et al.* Processing Dependent Behavior of Soft Imprint Lithography on the 1-10 nm Scale. *IEEE T. Nanotechnol.* **5**, 301-308 (2006).

14. Han, J. *et al.* Surface energy approach and AFM verification of the (CF)n treated surface effect and its correlation with adhesion reduction in microvalves. *J. Micromech. Microeng.* **19**, 085017 (2009).

15. Hill, D. N., Lee, J. D., Cochran, J. K. & Chapman, A. T. Vapour deposited cone formation during fabrication of low voltage field emitter array cathods. *J. of Mater. Sci.* **31**, 1789-1796 (1996).

16. Lee, H., Park, Y., Kim, J., Choi, J. & Kim, J. Investigation of the formation mechanism of Spindt-type cathode by simulation and experiments. *J. Vac. Sci. Technol. B* **17**, 547-551 (1999).

17. Zhang, S. *et al.* Optical negative-index bulk metamaterials consisting of 2D perforated metal-dielectric stacks. *Opt. Express* **14**, 6778–6787 (2006).

18. Zhang, S. *et al.* Near-infrared double negative metamaterials. *Opt. Express* **13**, 4922-4930 (2005).

19. Smith, D. R., Schultz, S., Markos, P. & Soukoulis, C. M. Determination of effective permittivity and permeability of metamaterials from reflection and transmission coefficients. *Phys. Rev. B* **65**, 5, (2002).

CHAPTER 3

MATERIALS SELECTIONS AND GROWTH CONDITIONS FOR LARGE AREA FLEXIBLE VISIBLE NEGATIVE INDEX METAMATERIALS FORMED BY NANOTRANSFER PRINTING

3.1 Introduction

As discussed in chapter 2, although nanoimprint lithography has forced the fishnet holes to open wide after the metal-dielectric multilayer growth, we still observed a large dimension change for the starting and ending fishnet layers, which means there is large angular growth profile associated with physical vapor deposition techniques. Such intrinsic limitation is inevitable in fishnet metamaterials fabrications if layer by layer material growth is involved. In order to remove the hindrance for growing more layers in 3D fishnet metamaterials, we have explored aspects of PVD growth in previously reported materials for multilayered fishnet NIMs, and introduce alternative dielectrics and deposition conditions that enable nearly ideal geometries by nTP.

3.2 Experiments

3.2.1 An Overview of Device Fabrication Scheme

Figure 3.1 provides schematic illustrations of the key steps for fabricating multilayered NIMs by nTP, as implemented here. A silicon wafer with a square array of periodic holes (period, P, edge-to-edge separation, W, and depth ,H) serves as a stamp which is shown in **Figure 3.1a**. The schematic shows the top view of fishnet features of relief and the cross sectional view of the fishnet relief cut at the red dash line. Electron-

beam evaporation forms multilayer stacks of metals and dielectrics (**Fig. 3.1b**) on the top and bottom regions of relief, with negligible deposition on the sidewalls. Transfer of material from the top regions to a target substrate, here facilitated by a photocurable polymer as an adhesive, completes the process (**Fig. 3.1c**). Previous multilayered fishnet NIMs formed by nTP exploited Ag as the metal and MgF2 as the dielectric, [1] due to their favorable plasmonic properties and established uses in optical coatings, respectively. Although Ag deposited by electron-beam evaporation with a material flux collimated in a direction perpendicular to the substrate surface grows in a nearly vertical fashion, MgF_2 exhibits angular growth with columar grain structure. [1] This latter behavior defines the overall growth profiles of the Ag/MgF2 multilayers. **Figure 3.1b** illustrates the key parameters: the angular profile of the growth, θ, and the characteristic widths at the bottom, W, and top, W´, of a multilayer stack with trapezoid height t. The thickness, T, corresponds to the distance from the base to the highest point on the top surface. The thickness-averaged value of θ is, therefore, simply given by $\tan\theta=(W´ - W) / 2t$.

3.2.2 Detailed Experiment Steps

The silicon was etched using a Bosch process (94 mTorr, etch/passivation: cycle time, 5 s/5 s; RIE power 20 W/0 W, SF_6/C_4F_8 flow rate 35 sccm/110 sccm for constant ICP power of 600 W; etch rate 1 μ m/80 s) with SF 6 gas, to a depth of ~ 500 nm. A layer of photoresist patterned by soft nanoimprint lithography served as the resist. Exposure to C_4F_8 in an ICP-RIE system (STS Inc., RIE power = 0 W, ICP power = 600 W, 15 s, chamber pressure = 94 mTorr, C_4F_8 flow rate 110 sccm) formed a cross-linked polymer on the

surface of the silicon to facilitate release in the transfer process by reducing the degree of adhesion between the deposited multilayer stacks and the substrate.

Multilayer stacks of Ag and MgF_2, and single layers of MgF_2, Al_2O_3, SiO_2, and TiO_2 were deposited using a six-pocket electron-beam evaporation system (AJA International). The sample was mounted close to the center of the dome in the chamber; where the distance between the sample (~ 2 cm) and source (~ 2.5 cm) was maximized (~ 60 cm). The angle between the sample and source was estimated to be less than 5 °. Due to the evaporation profile and the spherical dome shape, the incident flux was considered to be uniform over the 2 cm × 2 cm sample area. During deposition of Ag, MgF_2, Al_2O_3, SiO_2 and TiO_2 the average base pressures and growth rates were 1×10^{-8} Torr and 0.1–0.15 nm/s, respectively. The chamber pressure increased by about one order of magnitude during evaporation for most dielectrics except for titania, where the increase was more than two orders of magnitude. Experiments with physical collimators involved a Temescal (FC-1800) six-pocket electron-beam evaporation system, with the sample at one end of a cylindrical metal tube whose other end aligned to the source. The chamber geometry and sample orientation were similar to AJA International electron- beam evaporation system. Sequential thermal evaporation formed stacks of Ag and the MG alpha, alpha, alpha'-tris(4-hydroxyphenyl)-1-ethyl-4-isopropylbenzene with a base pressure of 1.0×10^{-6} Torr and rate 0.05–0.1 nm/s using a thermal evaporator (TCI International). The other MG material, 5 5 6 6 -tetrahydroxy-3 3 3 3 -tetramethyl-1 1 -spirobisindane, was deposited in similar fashion. Pentacene was deposited at 0.03–0.05 nm/s. All samples were mounted perpendicular to the fl ux in the thermal evaporator. The

distance between the sample (~ 2 cm) and source (~ 1 cm) was ~ 50 cm and the angle between them was less than 2 °. A 20 nm thick layer of SiO 2 deposited by electron-beam evaporation (AJA International) on the top layer of Ag served as a resist to wet etching of the Ag from the sidewalls.

A mixture of sodium thiosulfate (anhydrous, 1.581 g), potassium ferricyanide (0.042 g), potassium hexacyanoferrate (0.329 g) dissolved in DI water (100 ml) served as the etchant. Immersion times were 15, 30, 40, and 60 s, each followed immediately by rinsing in DI water.

A liquid pre-polymer to polyurethane (NOA 63, Norland Inc.) spin-casted onto a clean glass plate served as an adhesive. A silicon stamp coated with multilayer stacks was pressed into contact with this substrate. Passing UV light (Osram Sylvania 100 W MV PAR38, power density 8.4 mW/cm 2) through the glass for 1 h cured the NOA into a solid form, to form a strong bond with the multilayer stack. Removing the stamp completed the process.

Transmission spectra were collected using Varian Cary 5G UV-Vis-NIR spectrophotometer where the photo-detector is changed right at 800 nm where a small step-like response is always artificially added to the measured spectrum by the instrument.

The data was collected over a slit with a diameter of 2 mm. Transmission spectra were normalized using a glass substrate with cured NOA. Transmission spectra were

calculated using experimental parameters for the printed NIMs structures, with a commercial FDTD software package (Lumerical FDTD, Lumerical Solutions Inc.). A Drude model was used for the dielectric parameters of Ag in the FDTD simulation, with a plasma frequency of 1.37×10^{16} s^{-1} and scattering frequency of 8.5×10^{13} s^{-1}. The scattering frequency was increased by a factor of 3 compared with that of bulk Ag to account for the additional surface scattering loss. The FDTD simulations used averages of transmission separately computed with plane wave sources of TE and TM polarizations, to compare with the unpolarized light used in the spectrometer. These simulations used precise geometries extracted from images obtained in the experiment but without any line edge roughness (LER). The partial infiltration of openings in the mesh structure with adhesive material (NOA) used in the nTP process increases the background refractive index, ns. The effect moves the optical response to higher wavelength range compared to the case with air as the background medium. We used $n_S \sim 1.4$ in the FDTD modeling. The good agreement between experiment and FDTD results, which assume ideal geometries and zero LER, suggests that the observed losses are intrinsic to the materials. Slight variability in the dimensions of the structures, the properties of the constituent materials and the levels of control (such as uniformity and edge roughness) associated with the fabrication are the probable causes of the 10–15% overall discrepancy between experimental observation and FDTD simulation.

3.3 Results and Discussions

For purpose of fabricating fishnet NIMs by nTP, the ideal stack has $\theta = 0$. All observations in real systems show $\theta > 0$, dominated by angular growth in the dielectric material. **Figure 3.1d-f** presents SEM images of cross sectional and top views of films and multilayers deposited onto silicon stamps with P = 300 nm. **Figure 3.1d** corresponds to single layer of MgF_2 with T~300 nm, where angular growth is evident, i.e. W~77±2 nm and W´~228±6 nm, t~219±3 nm, with θ~19.1°±0.6°. Similar studies indicate that θ for Ag is close to zero. [1] This behavior in angular growth of MgF_2 directly affects the geometry of multilayer stacks of Ag (35 nm) / MgF_2 (15 nm) (**Fig. 3.1e**), where t~224±3 nm, W~117±3 nm, W´~249±15 nm, and θ ~ 15.3°±1.6°. Here, the diameters (D) of the holes in the fishnet evaluated at the top surface of the deposited multilayers are smaller than the value set by the geometry of the stamp, i.e. ~220 nm, and exhibit a large variance, i.e. between 25 nm and 85 nm (**Fig. 3.1f**). The values of θ, inferred from D, t and the geometry of the stamp, lie within the range of 16°-23° which is somewhat larger, but comparable to, those determined from the cross sections. Although these effects can be manageable in fishnets with relatively large geometries for operation in the IR and NIR, [1] they severely limiting for designs in the visible, where the period of the fishnet can be in the range of 300 nm or less. The choice of 300 nm or less period for visible operation came from linear scaling between surface plasmon induced light transmission and structure period [2-4]. For instance, the structures of **Fig. 3.1f** have an optical transmission of less than ~1% at a wavelength, λ = 650 nm, due mainly to small values of D. Experiments show that control over physical collimation and other

examined conditions associated with deposition offers only limited utility in reducing θ. In our setups, the source for evaporation has a diameter of ~2.5 cm, and the distance from source to sample is ~60 cm; for a sample size of ~2 cm placed perpendicular to the source, the incident material flux front has almost zero angular distribution over W~117±3 nm line width. Further efforts to enhance the degree of collimation using tubes placed between the source and sample dramatically reduce the deposition rates, but without significant benefits in angular growth (**Fig. S1**). Other techniques, such as ion beam assisted electron-beam deposition, also do not decrease θ appreciably (**Fig. S2**). (We note that θ can depend slightly, although not significantly, on the geometry of the relief on the substrate. See **Fig. S3**.) Other inorganic dielectrics with suitable optical properties, such as silica [5] and alumina, [2, 4] exhibit similar behavior. Organic small molecule materials, many of which can be thermally evaporated, represent alternatives.

Figure 3.2 provides top view SEM images of stamps coated with various candidate materials, including alumina (Al_2O_3; T~340 nm) (**Fig. 3.2a**), silica (SiO_2; T~300 nm) (**Fig. 3.2b**), titania (TiO_2; T~320nm) (**Fig. 3.2c**), a molecular glass (MG: 5 5' 6 6'-tetrahydroxy-3 3 3' 3'-tetramethyl-1 1'-spirobisindane; T~350 nm) (**Fig. 3.2d**) and pentacene (T~300 nm) (**Fig. 3.2e**). The results clearly show that only MG yields deposits with W~W′. Specifically, the inferred values of θ from the images of **Figure 3.2** are: ~25° for Al_2O_3; ~30° for SiO_2; ~25° for TiO_2; ~3° for the MG. The θ for pentacene is large, but difficult to estimate due to the grain structures. Such behaviors are qualitatively consistent with previous observations that dielectric materials such as SiO_2 and Al_2O_3 with polycrystalline morphologies tend to grow with

large angles on structured surfaces. [2,4-5] The results of **Figure 3.2** suggest that thermally evaporated MG systems [6,7] provide an attractive class of dielectric for NIMs formed by nTP, likely due to their lack of grain structure and non-columnar growth. Cross sectional and top view SEM images in **Figure 3.3** provide additional evidence that θ is ~2°, not only for a different MG but also for multilayer stacks with Ag. (The slight negative angle observed near the top of the stack arises from the focused ion beam preparation techniques used to enable the cross sectional views.) **Figure 3.3a** shows that with a MG thickness T~300 nm, where t~ 220 nm, W~110 nm and W´~130 nm, θ~2.2±0.2°. A multilayer stack of Ag/MG yields an even slightly smaller angle (**Fig. 3.3b**), where t~205 nm, W~115 nm, W´~125 nm, and θ~1.4±0.3°. For this geometry, the hole diameter decreases from the base to the top, from ~185 nm to ~159 nm (**Fig. 3.3c**). (We note that the value of θ inferred from D is ~3.5°). To ensure suitablity of MG as a good optical dielectric we performed spectroscopic ellipsometry and experimentally obtained refractive indices (n, κ) which verifies almost no absorption loss over the visible band (**Fig. S4**) and closely matches with previously reported (n, κ) values of such materials.

Deposits like those of **Figure 3.3** can be transferred, by nTP, to a target substrate to complete the fabrication. Here, a layer of a liquid prepolymer (Norland, NOA 63) spin-casted onto a glass plate ensures strong adhesion and high fidelty in the transfer. Photocuring the prepolymer by passing ultraviolet light through the glass and then removing the stamp yields a high quality NIMs structure, without observable defects. **Figure 3.4** shows large area SEM images of Ag/MG multilayer stacks on a stamp (**Fig.**

3.4a) and transferred to NOA/glass (**Fig. 3.4b**). NIMs with macroscopic sizes (~4 cm^2), limited only by the available overall dimensions of the stamp, and with uniform properties are routinely possible (**Fig. 3.4c**). Optical measurements indicate, however, low transmission in the range of wavelengths of interest, i.e. less than 1% at λ= 650 nm, as can be seen in **Figure 3.5a**. This low transmission is a direct consequence of the small θ because, in the absence of angular growth, the incident flux of Ag can lead to formation of grains and particles on the sidewalls of the multilayer stacks. The effect is visible in **Figure 3.3b**. Such deposits can electrically short adjacent Ag layers in the stack, thereby diminishing the excitation of strong magnetic responses that underpin the behavior in the NIMs structure. Immersing the sample in a wet chemical etchant for Ag can reduce or eliminate this problem. For etching times between 15 s to 30 s, the peak transmission increases from 18% to 40%, as shown in **Figure 3.5b**. Beyond 30 s, the etchant begins to remove significant amounts of Ag from the multilayer stacks themselves. The excess removal of Ag causes damage to the desired metal-dielectric-metal LC resonant circuit and the electro-magnetic resonance diminishes and consequently less light transmits out of the structure, thereby leading to a decrease in transmission from 23% to 12% for times of 45 s and 60 s, respectively.

Comparing experimental and FDTD results enables extraction of effective optical properties of the NIMs. It has been firmly established in the optics community that full-vectorial FDTD prediction of index is sufficiently accurate to experimental observations. [8-10] Interferometric measurements to verify FDTD predictions of negative refractive index have been previously demonstrated for similar fishnet

metamaterials. [1, 11] Transmission and reflection spectra are calculated using experimental parameters for the printed multilayered NIMs structures, with commercial FDTD software package. A Drude model was used for the dielectric parameters of silver in the FDTD simulation, with plasma frequency 9.0 eV and scattering frequency 0.054 eV. The scattering frequency is increased by a factor of three compared to that of the bulk silver in order to account for the additional surface scattering loss. [12] These simulation results were used to retrieve the impedance (z) and refractive index (n) of the samples. The retrieval exploited effective medium approaches, as described elsewhere. [8-10] For calculation, we use W=120nm, W'=140nm and T=285nm, with $\theta=2^\circ$ respectively. Optical characterization reveals a broadband transmission peak of 40.1% at 802 nm after an etching time of 30 s. The results exhibit good agreement with FDTD prediction (**Fig. 3.6a**). The origin of the shoulder at around 0.6 μm is due to the partial infiltration of polymer inside the open hole of fishnet pattern which causes plasmonic mode to split due to index contrast across the multilayer stack. **Figure 3.6b** shows the real and imaginary components of refractive index extracted by FDTD. The real part of the refractive index is negative from about 350 nm to 654 nm. The effective index of a multilayer metal/dielectric stack differs significantly from their respective bulk values. In the present case the multilayer stacks are comprised of 6 Ag and 5 MG (refractive index =1.6) alternating layers. The real component of refractive index of "bulk" Ag at around 1 μm is Re(n)~0.1 (Palik Silver) which makes the extracted stack effective index of $Re(n_{eff})$ ~0.25 consistent considering 35 nm thick Ag layers verses 15 nm MG layers. Two branches of the Re (n) which are labeled as 'Mode 1' and 'Mode 2' represent two propagating optical modes in the system as previously reported. [1,13] The loss for

these types of structure is reported in terms of FOM defined by - Re(n)/Im(n), which is high for the visible P = 300 nm Ag/MG NIMs of 7.4 at 654 nm as shown in **Figure 3.6c**, consistent with low loss. The good agreement between experiment and FDTD results that assume ideal geometries of the fishnets provides additional evidence of the high structural quality of the samples.

3.4 Conclusions

The results described here reveal some important effects of film growth in the formation of fi shnet NIMs by large area processing techniques such as nTP. A key fi nding is that the film growth characteristics in MG systems make them attractive alternatives to more widely explored inorganics for the dielectric layers. The outcomes enable fabrication of multilayered NIMs with excellent operational characteristics in the visible regime and they appear to have implications in other areas of optical application of nanotransfer printing.

3.5 Figures

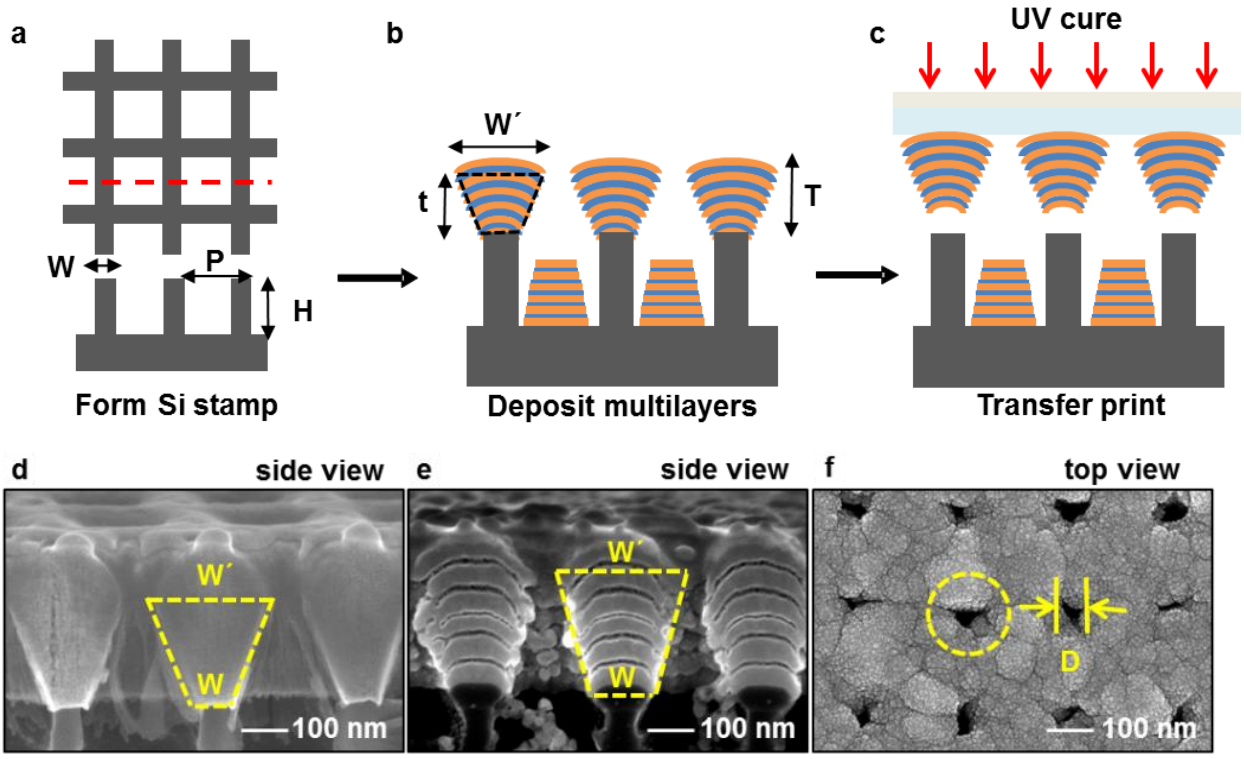

Figure 3.1 Schematic illustration of steps for fabricating multilayered fishnet NIMs by nTP. Top and Cross sectional views of (a) a silicon stamp made by nanoimprint lithography and etching, (b) this stamp after physical vapor deposition of alternating metal and dielectric films, (c) after transfer of the surface multilayer stacks onto a glass substrate coated with a photocurable polymer. Scanning electron micrographs of (d) cross sectional image of a layer of MgF_2 (300 nm) deposited by eleactron-beam evaporation onto a silicon stamp, (e) cross sectional image of alternating layers of Ag (35 nm) and MgF_2 (15 nm) on a silicon stamp, with total thickness ~300 nm, (f) top view of the stamp after deposition shown in (e). The dashed yellow boxes in (d) and (e) show the large angular profiles that develop in the films. The dashed yellow circle in (f) indicates the diameter of the periodic holes on the stamp before deposition.

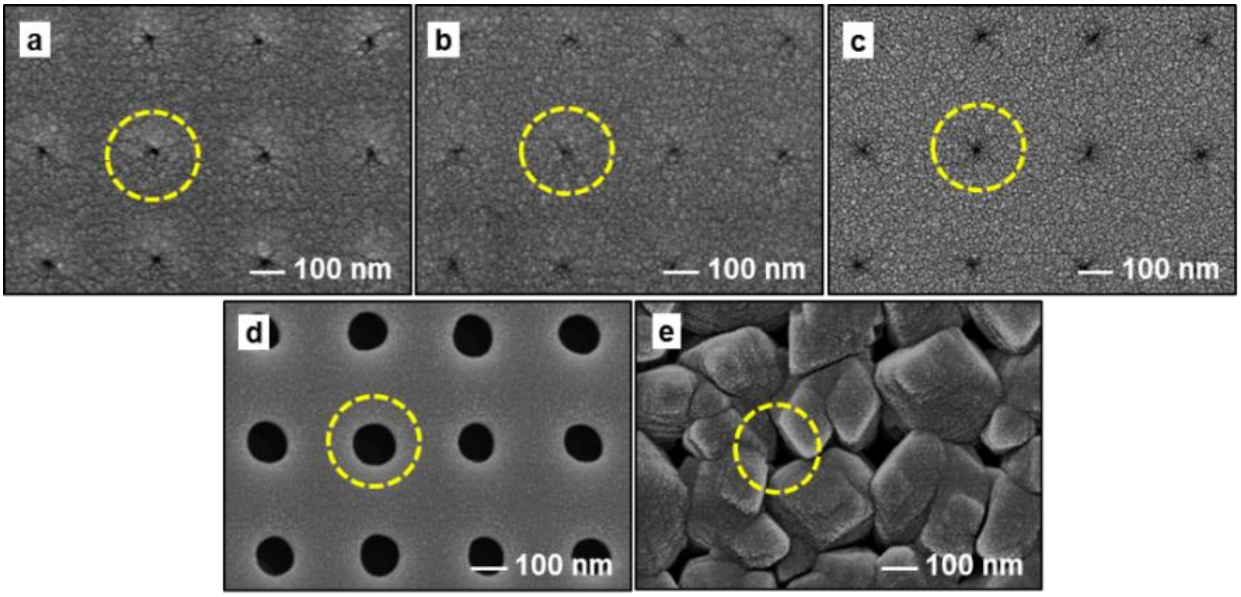

Figure 3.2 Top view scanning electron micrographs of silicon stamps after deposition of various dielectric materials. (a) Al_2O_3 (340 nm; electron-beam evaporation), (b) SiO_2 (300 nm; electron-beam evaporation), (c) TiO_2 (320 nm; electron-beam evaporation) (d) MG 5 5' 6 6'-tetrahydroxy-3 3 3' 3'-tetramethyl-1 1'-spirobisindane (350 nm; thermal evaporation) and (e) pentacene (300 nm; thermal evaporation). The dashed yellow circles illustrate the diameters of the periodic holes on the stamps before deposition.

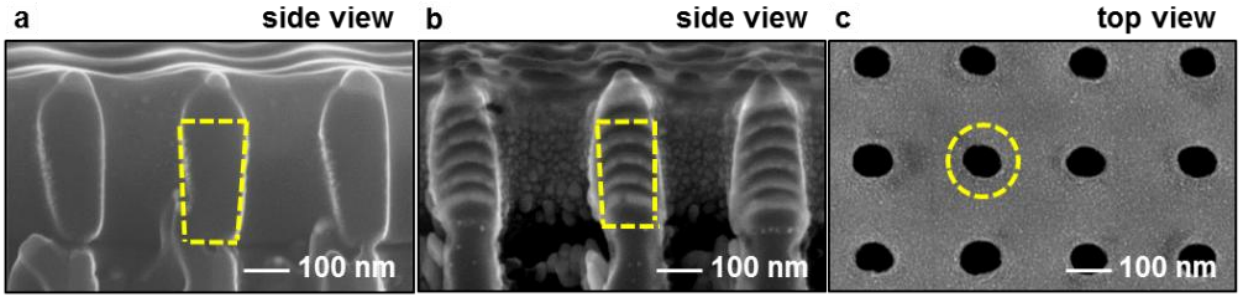

Figure 3.3 Cross sectional and top view scanning electron micrographs illustrating aspects of using MG (alpha, alpha, alpha'-tris(4-hydroxyphenyl)-1-ethyl-4-isopropylbenzene) as the dielectric. (a) Cross sectional image of a layer of MG (300 nm)

(Fig. 3.3 continued) deposited by thermal evaporation onto a silicon stamp, (b) cross sectional image of alternating layers of Ag (35 nm) and MG (15 nm) on a silicon stamp, with a total thickness ~280nm, (c) top view of the stamp after deposition shown in (b). The dashed yellow boxes in (a) and (b) show the slight angular profiles that develop in the films. The dashed yellow circle in (c) indicates the diameter of the periodic holes on the stamp before deposition.

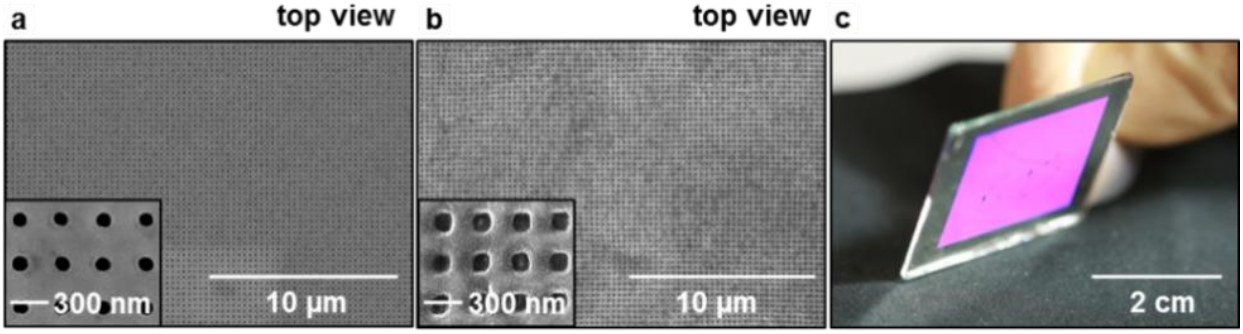

Figure 3.4 Scanning electron micrographs of large area fishnet NIMs comprised of 11 alternating layers of Ag and MG (alpha, alpha, alpha'-tris(4-hydroxyphenyl)-1-ethyl-4-isopropylbenzene). (a) Top view on the surface of a silicon stamp with an enlarged view as the bottom left inset, (b) top view after transferred to a glass substrate by nTP with an enlaregd view as the bottom left inset, (c) picture of a representative sample, which covers an area of ~4 cm^2.

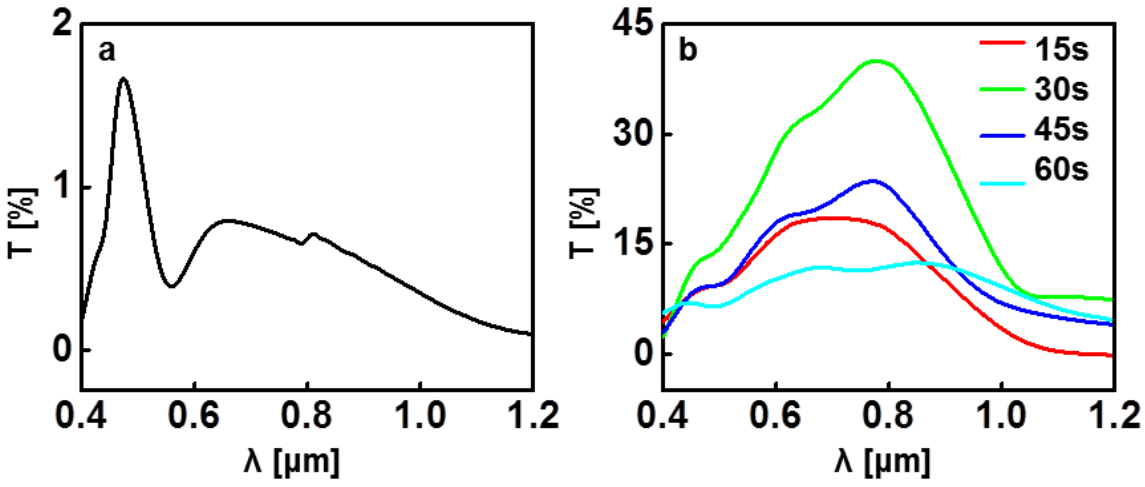

Figure 3.5 Transmission properties for (a) a stack of 11 alternating layers of Ag and MG (alpha, alpha, alpha'-tris(4-hydroxyphenyl)-1-ethyl-4-isopropylbenzene) on glass, as transferred by nTP, (b) after wet chemical etching of the Ag for different times.

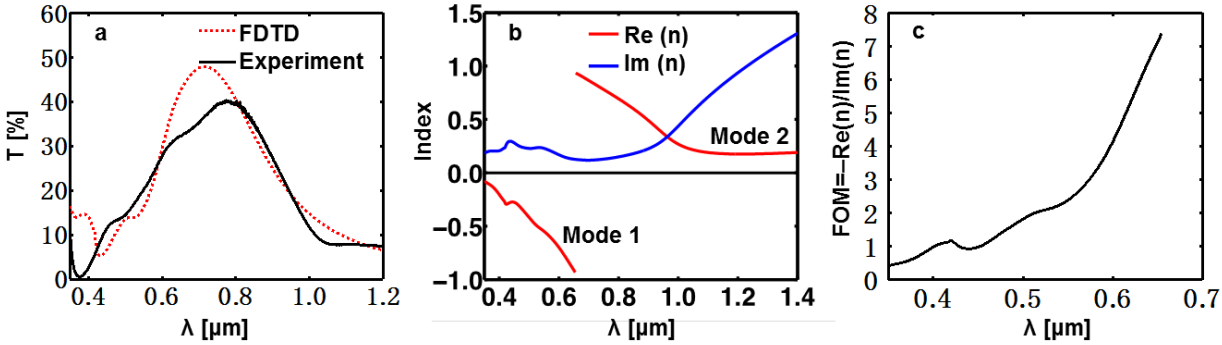

Figure 3.6 Experimental measurements and simulation results for transmission and refractive indices of Ag and MG (alpha, alpha, alpha'-tris(4-hydroxyphenyl)-1-ethyl-4-isopropylbenzene) NIMs. (a) FDTD predicted and experimentally measured transmission (with 30s Ag etch) for the chosen depth averaged fishnet line width Wav = 130 nm and the corresponding (b) retrieved refractive indices and (c) Figure-of-Merit for P = 300 nm fishnet.

3.6 References

1. Chanda, D. *et al.* Large-area flexible 3D optical negative index metamaterial formed by nanotransfer printing. *Nat. Nanotechnol.* **6**, 402-407 (2011).
2. Xiao, S. M., Chettiar, U. K., Kildishev, A. V., Drachev, V. P. & Shalaev, V. M. Yellow-light negative-index metamaterials. *Opt. Lett.* **34**, 3478-3480 (2009).
3. Dolling, G., Wegener, M., Soukoulis, C. M. & Linden, S. Negative-index metamaterial at 780 nm wavelength. *Opt. Lett.* **32**, 53-55, (2007).
4. Chettiar, U. K. *et al.* Dual-band negative index metamaterial: double negative at 813nm and single negative at 772nm. *Opt. Lett.* **32**, 1671-1673, (2007).
5. Hill, D. N., Lee, J. D., Cochran, J. K. & Chapman, A. T. Vapour deposited cone formation during fabrication of low voltage field emitter array cathodes. *J. Mater. Sci.* **31**, 1789-1796, (1996).
6. Dai, J. Y. *et al.* Molecular glass resists for high-resolution patterning. *Chem. Mat.* **18**, 3404-3411, (2006).
7. Pfeiffer, F., Felix, N. M., Neuber, C., Ober, C. K. & Schmidt, H. W. Physical vapor deposition of molecular glass photoresists: A new route to chemically amplified patterning. *Adv. Funct. Mater.* **17**, 2336-2342 (2007).
8. Smith, D. R., Schultz, S., Markos, P. & Soukoulis, C. M. Determination of effective permittivity and permeability of metamaterials from reflection and transmission coefficients. *Phys. Rev. B* **65**, 5 (2002).

9. Chen, X. D., Grzegorczyk, T. M., Wu, B. I., Pacheco, J. & Kong, J. A. Robust method to retrieve the constitutive effective parameters of metamaterials. *Phys. Rev. E* **70**, 7 (2004).
10. Smith, D. R., Vier, D. C., Koschny, T. & Soukoulis, C. M. Electromagnetic parameter retrieval from inhomogeneous metamaterials. *Phys. Rev. E* **71**, 11 (2005).
11. Garcia-Meca, C. *et al.* Low-Loss Multilayered Metamaterial Exhibiting a Negative Index of Refraction at Visible Wavelengths. *Phys. Rev. Lett.* **106**, 4 (2011).
12. Johnson, P. B. & Christy, R. W. Optical constants of noble metals. *Phys. Rev. B* **6**, 4370-4379 (1972).
13. Zhang, S. A. *et al.* Optical negative-index bulk metamaterials consisting of 2D perforated metal-dielectric stacks. *Opt. Express* **14**, 6778-6787 (2006).

CHAPTER 4

THREE-DIMENSIONAL, WIDE-BAND TUNABLE PLASMONICS WITH EXTREME STRETCHABILITY

4.1 Introduction

Three dimensional photonic structures interact with light in many extraordinary ways that yield optical properties can hardly been achieved with two dimensional planar structures. Chiral metamaterials [1], all direction [2] or planar [3, 4] stacked split ring resonators, and quasi 3D plasmonic structures [5, 6] represents a few applications. However, the fabrication techniques involved such as direct laser writing, stacked electron beam lithography and membrane projection lithography etc. are quite challenging and not large-scale applicable, which limits the wide adoption and real application of such complex photonic structures. In addition, three dimensional photonic device with reversible structural formation and wide band tunability has rarely been demonstrated. Plasmonics is one type of photonic devices that can concentrate light at the nanometer scale and amplify the electromagnetic fields through the excitation of localized surface plasmon resonances. The plasmonic signal is sensitive to the nanostructure size, shape, interparticle distance and surrounding dielectric environment, they can be used as gas molecular and biomolecular sensors with ultra-high sensitivity [5, 7-8]. Common fabrication scheme such as electron beam lithography and nanoparticle synthesis have limited the device application on a two dimensional, small area and rigid substrates which is not ideal for wearable, low cost devices. By implementing similar strategies from the stretchable, buckled semiconductor electronics [9-14], a wide band tunable, large area

plasmonic device with extreme stretchability and reversible complex three dimensional structures can be realized. With the new mechanical properties, stretchable and tunable plasmonic devices have open up the potential to enable tunable optical properties and be wearable on human skin as epidermal photonic devices [15]. There have been a few efforts in realizing flexible and stretchable plasmonic devices recently which still remains as a great challenge. The device area is limited to hundreds of square micrometers for EBL fabricated devices [16-17] or the newly developed nanostencil technique [18-19]. Self-assembled gold nanoparticle array transferred onto elastomeric substrates has larger area but the particle distribution is irregular and hard to control over long range [20, 21]. Last but not the least, the stretchability of all recent demonstrated devices only ranged from 20%-30% [18, 20] with rare cases of ~50% [16], which is still falls behind compared to the stretchable electronics applications that has extreme stretchability above 100% [22-25]. As a result, only narrowband tunability is realized for tens of nanometers and the associated mechanical properties are not compatible with potential human body integration and low cost applications. We employ simple yet robust soft lithography and transfer strategies used in large area fishnet metamaterials [26-28] to yield a large area gold nanodot array (period = 300nm, diameter=220nm) bonded to an ultra-soft elastomer substrate. Such ultra-fine and uniform plasmonic structure has a device area of $4cm^2$, an unusual stretchability beyond 100% and broadband tunability ~540nm in the transmission spectra. The nanodot geometry deformation was carefully examined under different strains, and for the first time, we observed a linear, two dimensional interparticle spacing change due to Poisson effect under smaller strains, transformed into a three dimensional, short range ordered buckling waves due to

compression at large strains. Detailed mechanical modeling including semi- analytical study and Finite Element Analysis (FEA) have been performed to explain such extraordinary structural change, while Finite Element Method (FEM) simulation results are used to compare with the experimental transmission spectra measurement. All the results describe here are highly relevant to future human body compatible optical sensors and metamaterials devices, and real time strain-tunable plasmonic devices.

4.2 Experiments

4.2.1 An Overview of Device Fabrication Scheme

We started with a soft lithographic technique (**Fig. S5a**) that creates uniform square nanopost array on silicon substrates (P=300nm, D=200nm, H=300nm) which is served as a stamp. An additional fluorination step is used to reduce the surface adhesion during which the fluoropolymer formation has caused the nanopost diamater increased to 220nm. A multilayer materials growth step (the ink) (**Fig. S5b**) is completed in electron beam evaporator, where a 40nm of gold is grown first as the functional plasmonic materials, a 5nm titanium is used to adhere the gold to the ending silicon dioxide layer (~40nm). Au nanodot layer maintains a diameter of 220nm due to vertical growth while angled growth associated in the dielectric SiO_2 layer [27] has caused the ending nanodot size enlargement to ~250nm. Ultra-violet ozone treated PDMS substrate with a thickness around 300 micrometer and modulus of 0.17 MPa has been brought into contact with the SiO_2 top surface. A mild heating promotes the condensation reaction between SiO_2 and the hydroxyl functionality on the PDMS surface and creates a strong bonding. The

nanodot array is transferred to the soft elastomeric substrate completely (**Fig. S5c**). SEM images of the silicon "stamp" and the nanodot array transferred to the soft substrate before stretching and released after stretching are shown in **Fig. S5d-f. Fig. S5g** shows a systematic stretching experiment from 0% to 107% on a homemade metal stretcher. **Figure 4.1a** compares a device without any strain applied and a 107% strain along the y direction. Under such large strain, the plasmonic array forms semi- regular three dimensional wavy patterns as shown in the schematic of **Figure 4.1b. Figure 4.1c-d** are the 45°tilted SEM images of the transformation from no strain state to a buckled state, which indicates a clear transition from two dimensional planar geometry to a three dimensional buckled geometry. **Figure 4.1e-i** shows the optical images of the fabricated large area, uniform nanodot array with different materials such as gold (**Fig. 4.1e**), silver (**Fig. 4.1f**) and aluminum (**Fig. 4.1g**). The slight color difference comes from different resonance peaks associated with different plasmonic materials. **Fig. 4.1h-i** show the gold plasmonic device in a tilted view and a bent view, with uniform color and extreme flexibility. These results demonstrate soft lithography and transfer printing techniques can yield large area nanostructures that has precise dimension control and uniformity with high throughput that no other technique can compare. Such fabrication scheme is not limited by any nanostructure size/shape and compatible with many classes of plasmonic materials.

4.2.2 Detailed Experiment Steps

The silicon nanodot array pattern was obtained by soft nanoimprint lithography and oxygen plasma dry etching (PlasmaTherm, chamber pressure = 15 mTorr, RIE power = 50 W, O_2 flow rate = 10 sccm) that forms a photoresist mask described elsewhere [27, 28], followed by etching using a Bosch process (STS Inc., chamber pressure = 94 mTorr, etch/passivation cycle time = 5 s/5 s, RIE power = 20 W/0W, SF_6/C_4F_8 flow rate = 35 sccm/110 sccm, ICP power = 600 W), to a depth ~300 nm. Remaining photoresist residue is removed by oxygen plasma dry etching again. Exposure to C_4F_8 in an ICP-RIE system (STS Inc., chamber pressure = 94 mTorr, passivation time = 15 s RIE power = 0 W, C_4F_8 flow rate = 110 sccm ICP power = 600 W) formed a cross-linked polymer on the surface of the silicon to facilitate release in the transfer process by reducing the degree of adhesion between the deposited multilayer stacks and the substrate.

The metal layer (Au,Ag and Al), titanium adhesion layer and SiO_2 bonding layer were deposited using an AJA International 6-pocket electron beam evaporator. Typical chamber base pressures of 1.0 $x10^{-8}$ Torr and deposition rates of 0.1-0.15 nm/s were found to yield the best growth quality.

A low modulus, tacky form of PDMS, created by mixing in a 35:1 ratio by weighing base and curing agent of a commercial material (Sylgard 184, Dow Corning), was used for receiving substrate. The surface of this material was activated by exposing it to ozone created by deep ultraviolet light (BHK Inc., grid lamp, model 88-9102-02) for 3.5

min. Contact with the nanodot array on the silicon stamp will initiate condensation reactions between the hydroxyl groups on the PDMS and those on the top exposed layer of SiO_2 on the substrate. A mild heating at 110 degree for 25s would lead to strong bonding between the nanodot array and PDMS substrate. Peeling the PDMS away transfers the nanodot array, in their entirety, from raised regions of the substrate.

Transmission spectra were collected using Varian Cary 5G UV-Vis-NIR spectrophotometer. The data was collected over a slit with a diameter of 3 mm, with a polarizer oriented perpendicular to the stretching direction. Transmission spectra were normalized using a bare PDMS substrate.

The Finite Element Method (COMSOL software) was employed to study the optical response of structure with increasing strain. In our simulations, structure was placed in a homogenous surrounding medium with dielectric constant as $\epsilon_0 = (1 + n^2_{PDMS})/2 = 1.48$ where $n_{PDMS} = 1.48$ is the refractive index of PDMS. Such homo-medium approximation has been widely used in theoretical simulations and it can give all optical features as real setup in experiments with similar plasmon resonance peak.

4.3 Results and Discussions

One of the key strategies here is using an ultra-low modulus PDMS substrate (170kPa) and induce a strong bonding between the soft substrate and the rigid nanodot array, unlike previous reports on nanostencil technique and Au self-assembly technique

that used more rigid elastomeric substrates which limited the stretchability. Such design has great impact on the ultimate mechanical properties of the plasmonic nanodot array which can sustain unusual large strains. We have observed the details of microscopic nanodot geometry change with the aid of high resolution SEM images. In **Figure 4.2a**, a four row by seven column nanodot array was imaged with 45° tilted view. When the uniaxial strain is applied in the y direction, the nanodot gap in the x direction decreases linearly for the case of 20% and 37% strain due to the Poisson's effect. When the strain reaches a critical value, the spacing between the SiO_2 disks in the x direction decreases to zero, the stiff dots start to squeeze each other, which then leads to the formation of buckling structures to release the relative large strain energy as seen in the 56% strain case. Short range ordered waves with five dot wavelength are observed to be the dominant buckling pattern here. When the strain continues to increase in the y direction, the spacing between the nanodots in the y direction widens, while the buckled structure remains as five dot waves as seen in 72%, 89% and 107% strain cases. The larger strain would cause bigger wave amplitudes due to the greater compression between the neighbor dots.

Figure 4.2b-c show the nanodot geometry change derived from the FEA simulation and semi-analytical method. The parameters employed for the models are shown in **Fig. S6a-b**, where we simplify the nanodot structure into a 40nm thick Au disk with 220nm diameter and 40nm thick SiO_2 disk with 250nm diameter. In the regime of non-buckling deformations under small stretching, the plasmonic dots (>59 GPa) undergo negligible deformations, as evidenced by the experiment images and FEA results (for applied strain ε_{appl}<40%) in **Fig. 4.2**, because they are much stiffer than the elastomeric substrate

(170 kPa). As a result, the stretching deformation is mainly accommodated by the soft substrate material. The accurate change of the dot-to-dot spacing $S_{horizontal}$ and $S_{vertical}$ until the neighboring nanodots touch each other can be calculated precisely, according to

$$S_{horizontal} = P_0\left(1+\varepsilon_x\right) - D_{SiO2} = \left(S_0 + D_{SiO2}\right)\left(1+\varepsilon_x\right) - D_{SiO2}$$
$$S_{vertical} = \frac{P_0}{\sqrt{1+\varepsilon_x}} - D_{SiO2} = \frac{S_0 + D_{SiO2}}{\sqrt{1+\varepsilon_x}} - D_{SiO2} \quad (1)$$

$$\varepsilon_x = 1 - \left(1+\varepsilon_{appl}\right)^{-1/2} \quad (2)$$

where ε_X is the transversely compressive strain approximated for applied strain ε_{appl}. The results have been plotted in **Fig. S6c** (P=300nm and D=200nm). The critical applied strain that induces the onset of buckling can be then solved. For the stretching larger than the critical strain, the buckled plasmonic dots would represent a more energy favorable configuration than the non-buckled configuration, as evidenced by the experimental observations. The nanodot geometry change predicted by both FEA and semi-analytical method has shown a great similarity compared to the SEM images at all strain levels. A top-down view comparison has also proved the nice fit between the experiment and theory in **Fig. S7**. **Figure 4.2d-f** shows the AFM measurement of surface profile for the case of 72% strain, as comparison, **Figure 4.2g-i** shows the surface profile predicted by FEA models. The height profile along line 1 plotted in **Fig. 4.2e** indicates the average wave amplitude found in experiment is ~ 160nm which agrees well with the predicted depth change along x direction by FEA in **Fig. 4.2h**. The height profile along line 2 plotted in **Fig. 4.2f and Fig. 4.2i** has periodic change ~100nm which also agrees with the modeling results in the y direction which corresponds to the nanodot multilayer thickness (~85nm).

Five dot wave pattern dominates when buckling appears, and different modes coexist under the same strain condition (56%) as shown in **Fig. S8**. In **Figure 4.3a-c**, the close-up view of two, three, four and five dot waves imaged by SEM with top down view have been compared to FEA results and semi-analytical results. A representative buckling mode with five dots in one period (**Fig. S9**) is taken as an example herein to illustrate the model. Under stretching along the y axis, the buckling mode observed in experiment measurements is assumed in the theoretical model, similar to the sinusoidal buckling profile used in analyses of wrinkling in wavy silicon ribbon fully bonded to prestretched elastomeric substrate [12]. Specifically, two dots in the period undergo the same rigid- body rotation (with an angle of θ), while the other three dots keep almost flat, as shown in **Fig. S9a**. It is noteworthy that two different contact modes between the rotated dot and the dot at wave valley are possible to occur, as shown in **Fig. S9b**. the rotational angle θ, can be then determined by solving the following equation:

$$\left[\frac{5P_0}{\sqrt{1+\varepsilon_{appl}}}-D_{SiO_2}\right]\tan^2\frac{\theta}{2}-4h_{SiO_2}\tan\frac{\theta}{2}+\frac{5P_0}{\sqrt{1+\varepsilon_{appl}}}-5D_{SiO_2}=0$$

for contact mode I, (3a)

$$\left[\frac{5P_0}{\sqrt{1+\varepsilon_{appl}}}-D_{SiO_2}\right]\tan^2\frac{\theta}{2}-4\left(h_{Au}+h_{SiO_2}\right)\tan\frac{\theta}{2}+\frac{5P_0}{\sqrt{1+\varepsilon_{appl}}}-3D_{SiO_2}-2D_{Au}=0$$

for contact mode II. (3b)

In addition, four and five dot waves are observed to be the major patterns at higher strains (89% and 107%) while two and three waves are hardly observed. Lower strains such as 56% have all typed of wave patterns present. Using similar model and calculation, we have summarized all the critical strain conditions that applicable to different nanodot

period-over-diameter ratios (P/D) in Figure 3d with experimental data points plotted against the analytical results. If we have a low P/D ratio which means a large nanodot diameter and small interparticle spacing, we will have a buckling occurring at much lower strain compared to a high P/D ratio case. With all the initial nanodot geometry information known beforehand, we can predict the critical strain that three dimensional buckling would appear.

Figure 4.4a shows the large area SEM images of the nanodot array with 37% strain applied in the y direction. The interparticle spacing decreases in the x direction and the nanodots almost touch each other. At a large enough strain that exceeds the critical value such as 72%, the buckling effect occurs all over the device area as shown in **Figure 4.4b**. The buckling pattern is observed to be regular in a local region such that the same wave pattern would repeat for a few wavelengths. Over the long range, the buckling waves undergo many types of change. Typical transformations are (1) buckling mode change, e.g. from five particle waves to four particle waves; (2) one wave with larger wavelength splitting into two waves with smaller wavelength, or where two small waves merge into one wave; (3) wave peak changes to wave valley or vice versa. Such long range complex pattern formation cannot be predicted by the analytical model or FEA simulation due to the complication in calculation and many factors that affect the pattern formation. Since the soft substrate has very low modulus and the rigid nanodot can rotate in any arbitrary directions, the local interaction between nanodots and whether tensile strain or compressive strain is present for a particular region cannot be predicted or controlled in the experiment. Despite that many types of geometry deformation can be found in the

experiment, we can still make reasonable assumptions in the mechanical models, as majority of the buckling pattern is five dot waves. **Figure 4.4c-d** shows the 45 °tilted SEM view along both x and y directions with 107% strained applied in y direction. It provides us a clear view on the three wave pattern transformations as discussed before, and also confirmed that the semi-regular buckling waves consist of mostly five particles. A complete set of SEM images of the nanodot array deformation at different strains in a top down view and tiled view have been shown in **Fig. S10 and S11**. **Fig. S12** has revealed the large area patterns (~10000 μm^2) under a large strain which is defect-free and forms semi-regular buckled waves all over the area. All these results have suggested that with the tool of designing initial nanostructure geometry with different sizes, shapes and interparticle spacings etc., we can form complicated three dimensional buckled patterns that can result in extraordinary plasmonic resonance beyond the critical strain value.

Figure 4.5a shows the transmission spectra measured through 3mm diameter slit opening under the seven strain conditions normalized to a bare PDMS substrate. The light source is polarized perpendicular to the stretching direction so that the effect of decreasing the dot-to-dot spacing can be revealed. The original Au nanodot array with a period of 300nm and an Au diameter of 220nm has a resonance peak located around 770nm. With uniaxial strain applied, we observed an almost uniform red shift in the plasmonic resonance peak to 1310nm at the strain of 107%. This red shift can be understood by many previous experiments on studying the effect of different interparticle spacings [29, 30]. When the polarization is aligned in the longitudinal mode (orthogonal to the stretching direction), the decrease in the dot-to-dot spacing would cause weakening of coulomb

coupling forces between neighboring nanodots, thus resulting in a lower resonance frequency and red shifts in the transmission spectra. Although a three dimensional buckled wave has formed beyond the critical strain value, we didn't observe an abrupt change in the transmission spectra features. At larger strains, the absolute transmission value increases and the plasmonic resonance broadening has been narrowed. The nanodot geometry deformation under different strains derived from the mechanical models provide the basis for the optical simulations where accurate structural information is essential. Here we have investigated the optical behavior by employing both numerical simulations and analytical analysis. The effect of linear interparticle spacing change in both x and y directions have been plotted in **Fig. S13**. A smaller structural dimension (**Fig. S13a**) is used in the simulation to avoid interference effect and make computation efficient. By taking both gap widening in the y direction and gap narrowing in the x direction into consideration, a uniform red shift in the resonance peaks has been observed with increasing strain in the y direction (**Fig. S13b**). If we keep the spacing between nanodots constant in the x direction and keep widening the gap in the y direction only, the broadening of resonance has been narrowed with increasing strain (**Fig. S13c**). On the contrary, the broadening of resonance widens at higher strain if the gap shrinks in the x direction and keeps constant in the y direction (**Fig. S13d**). The effect of nanodot rotation has also been examined for the buckling patterns in **Fig. S14**. The strain has been fixed at 80% and the rotational angles have been varied from 0 degree to 80 degree. The simulation results showed a blue shift in transmission spectra for larger rotational angles which means the red shifts with increasing strain are mainly contributed by the interparticle spacing

change in both directions, not by the nanodot angular rotation. However, the increase in the transmission value could be contributed by the change of nanodot rotation.

With all the factors examined, the simulation results based on five dot waves are presented in **Figure 4.5b** where strain ε_X varies from 0 to 107% as in experiments. The strain will result in a large red shift of plasmon resonance peak, the transmission value is enhanced with increasing strain and the broadening of plasmon resonance peak is narrower at larger strain, which agree with the real experimental measured spectra. The mismatch in the absolute value of resonance shift and transmission could be attributed by the different types of buckling modes and the deformation is semi-regular over the large area with unpredictable geometry complexity. Accordingly, the measured transmission spectra is actually averaged optical response over all possible buckling modes with unknown mode distribution function. Through our simulations, we found the lineshape of transmission spectra depends on the real buckling geometry at large strains, and for such cases, there are additional in-continuity appearing which might be due to the larger near field coupling between cell structures. We believe the lineshape of transmission spectra will be smoothed after averaging over a series of buckling modes if the mode distribution function is known. A coupling-dipole approximation method described in **Fig. S15** shows similar results that the resonance peak red shifts with increasing strain. In order to test the uniformity of the stretched sample, we have repeated the measurement over different areas for the cases of 37% and 72% as shown in **Figure 4.4a-b**. The results in **Figure 4.5c** have demonstrated the uniformity of the fabricated sample under different strains. **Figure 4.5d** has compared the transmission spectra of the sample without any strain and

released from a large strain which indicates the three dimensional buckling deformation is repeatable and reversible and it is ideal for real-time strain tunable applications.

4.4 Conclusions

All the new mechanic and optical properties generated in such large area, ultra stretchable and tunable plasmonic structures, offer strong potential in realizing different types of reversible three dimensional optical structures and epidermal photonic sensors by just introducing strain. With the capacity of mechanical and optical modeling illustrated here, complicated photonic components and structures can be designed to yield an otherwise impossible three dimensional structures upon buckling, with uniaxial, biaxial or radial strains. New, extraordinary plasmonic resonance features could be made possible, with additional real time, wide band tuning capabilities. Strain induced color change and low cost wearable plasmonic sensors would represent other opportunities.

4.5 Figures

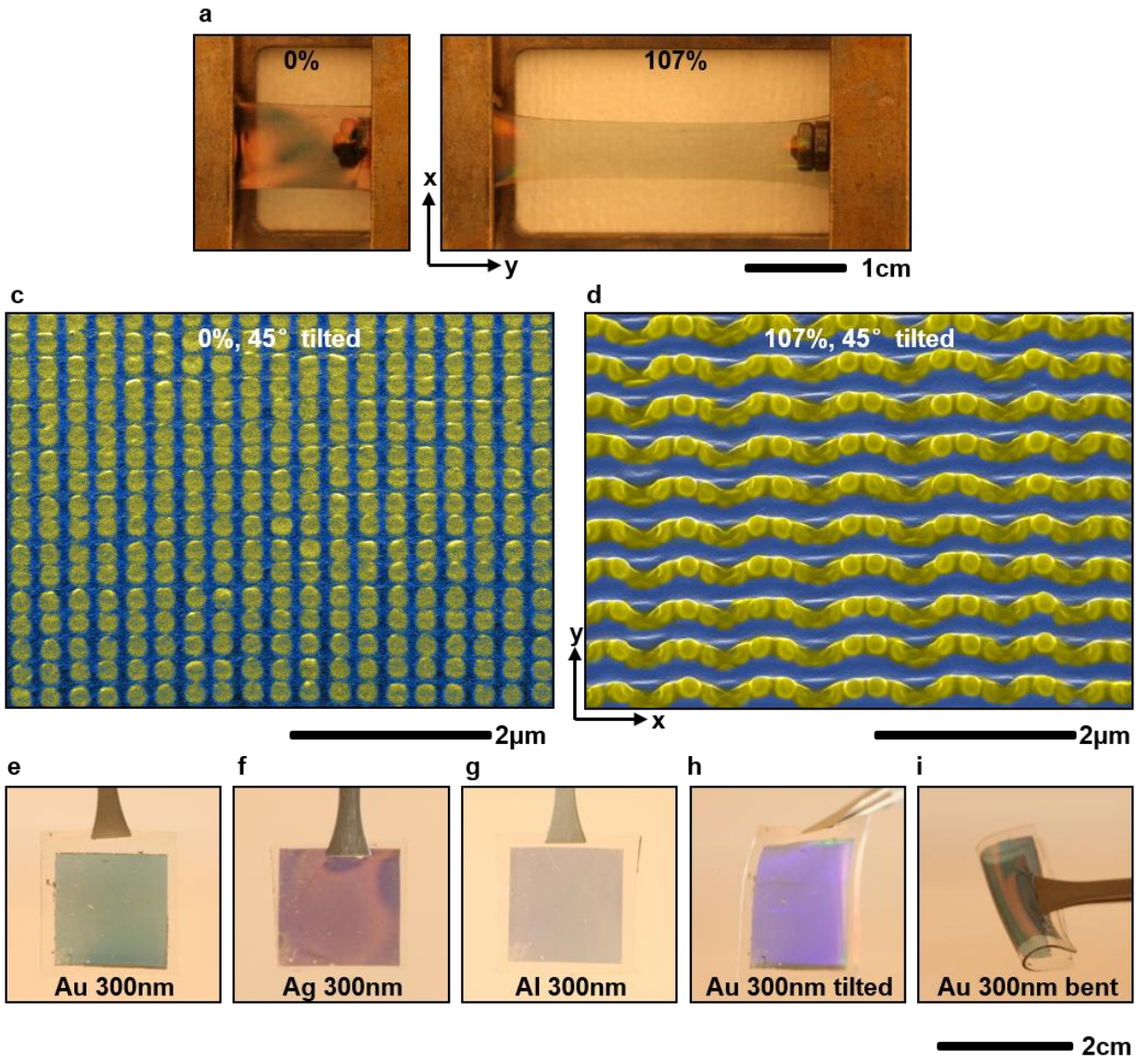

Figure 4.1 Soft, large area nanodot plasmonic device and three dimensional buckled structure formed at extreme stretching. (a) Au nanodot array (P=300nm, D=220nm) on PDMS substrate under zero strain and 107% strain. (b) Au nanodot plasmonic array with zero strain imaged under 45 ºtilted (along y) SEM. (c) Au nanodot plasmonic array with 107% strain (applied in y direction) imaged under 45 ºtilted (along y) SEM. (d) Optical

(Fig. 4.1 continued) image of a gold plasmonic device. (e) Optical image of a silver plasmonic device. (f) Optical image of a aluminum plasmonic device. (g) Optical image of a tilted gold plasmonic device. (h) Optical image of a bent gold plasmonic device.

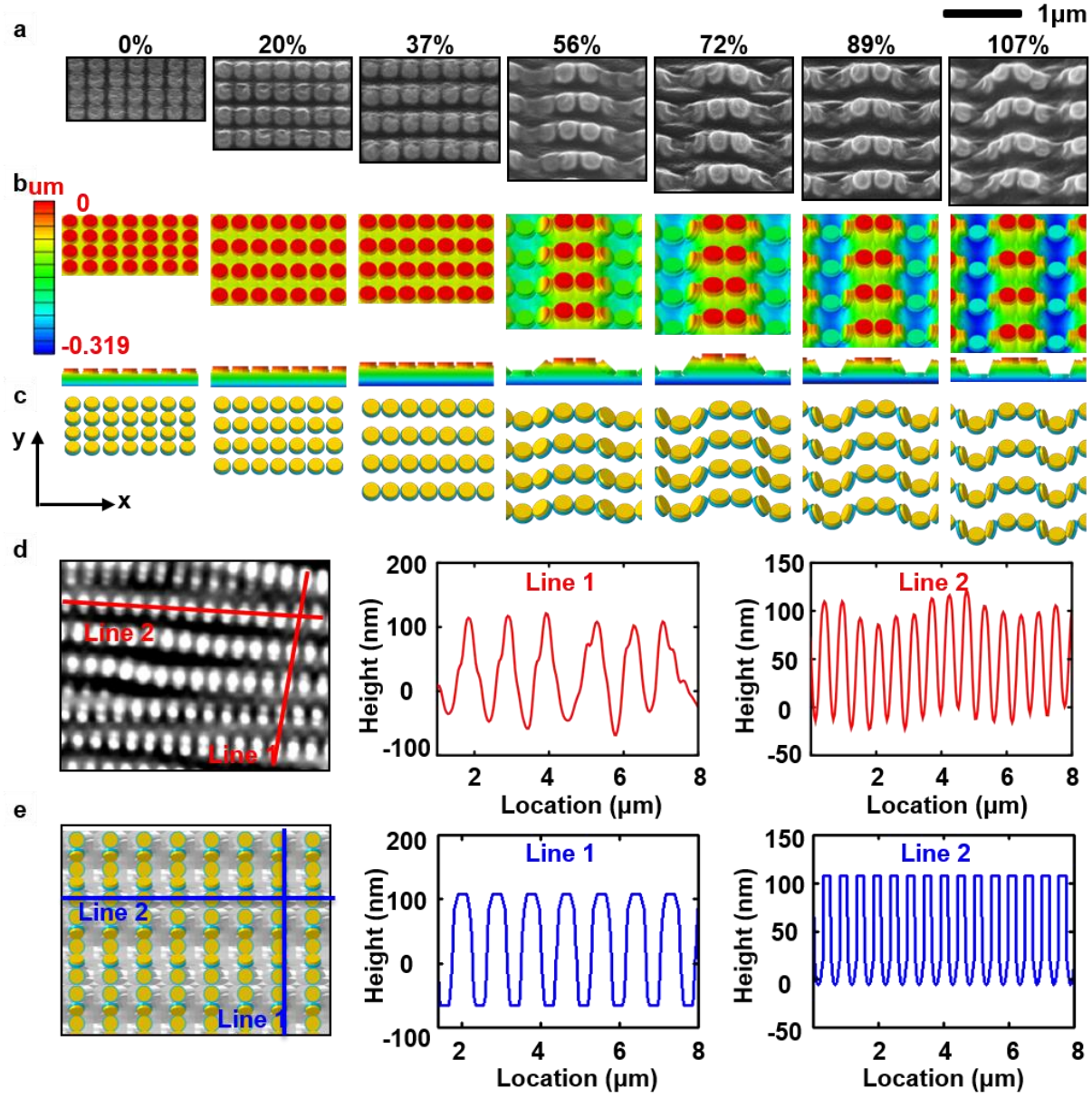

Figure 4.2 Comparison of the SEM images and mechanical model results under different strains. (a) Au nanodot array (P=300nm, D=220nm) on PDMS substrate

(Fig. 4.2 continued) under seven strains applied in the y direction imaged with 45 °tilted angle. (b) FEA results of the Au nanodot array deformation under seven strains shown with 45 °tilted angle, the color bar represent height change. (c) Semi-analytical results of the Au nanodot array deformation under seven strains shown with 45 °tilted angle. (d) AFM results of the height profile under the 72% strain, with the exact wave amplitude plotted along line 1 and line 2. (e) FEA results of the height profile under the 72% strain, with the exact wave amplitude plotted along line 1 and line 2 as a comparison to those shown in d.

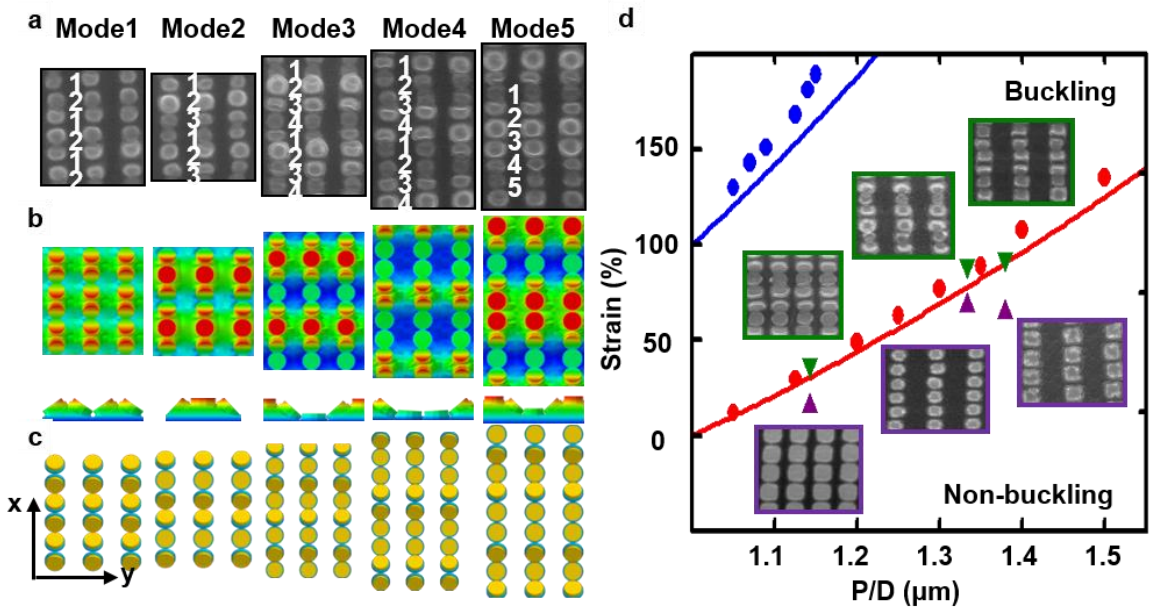

Figure 4.3 Comparison of the SEM images and mechanical model results of different buckling modes. (a) Top down SEM images of five different buckling modes coexisting under 56% strain applied in the y direction, which have two, three, four and five dots in a wavelength. (b) Top down view of the FEA results that have five different buckling modes. (c) Top down view of the semi-analytical results of the five different buckling

(Fig. 4.3 continued) modes. (d) Theoretical prediction and experimental verification of creating buckling pattern beyond critical strain withdifferent nanodot array geometry.

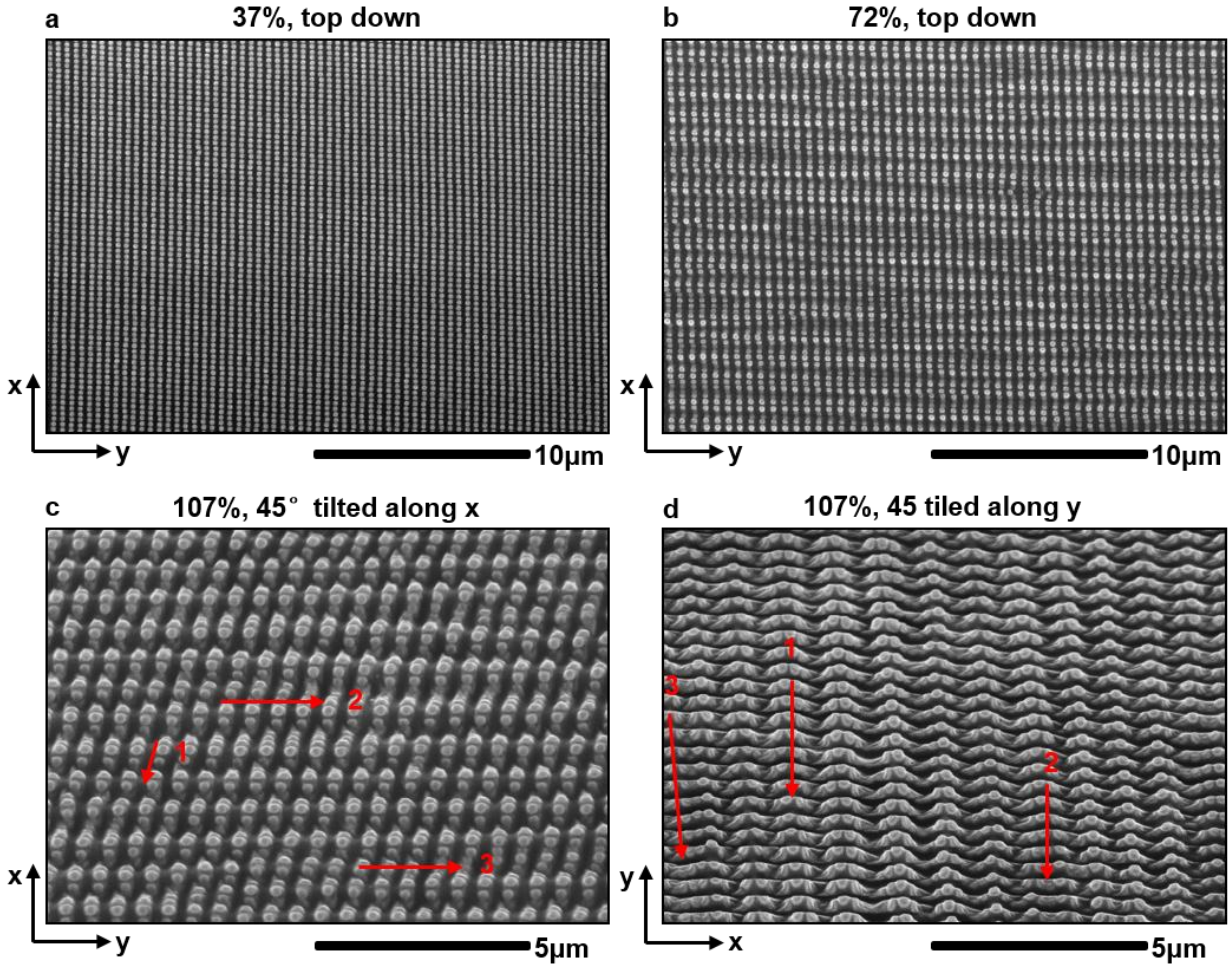

Figure 4.4 Large area SEM images before and after the appearance of three dimensional buckled structure. (a) Top down SEM of Au nanodot array (P=300nm, D=220nm) before critical strain. (b) Top down SEM of Au nanodot array under 72% strain with buckling waves formed. (c) 45 °tilted SEM (along x) of Au nanodot array under 107% strain applied in the y direction, the arrows show three long range buckling transformation. (d)) 45 °tilted SEM (along y) of Au nanodot array under 107% strain

(Fig. 4.4 continued) applied in the y direction, the arrows show three long range buckling transformation.

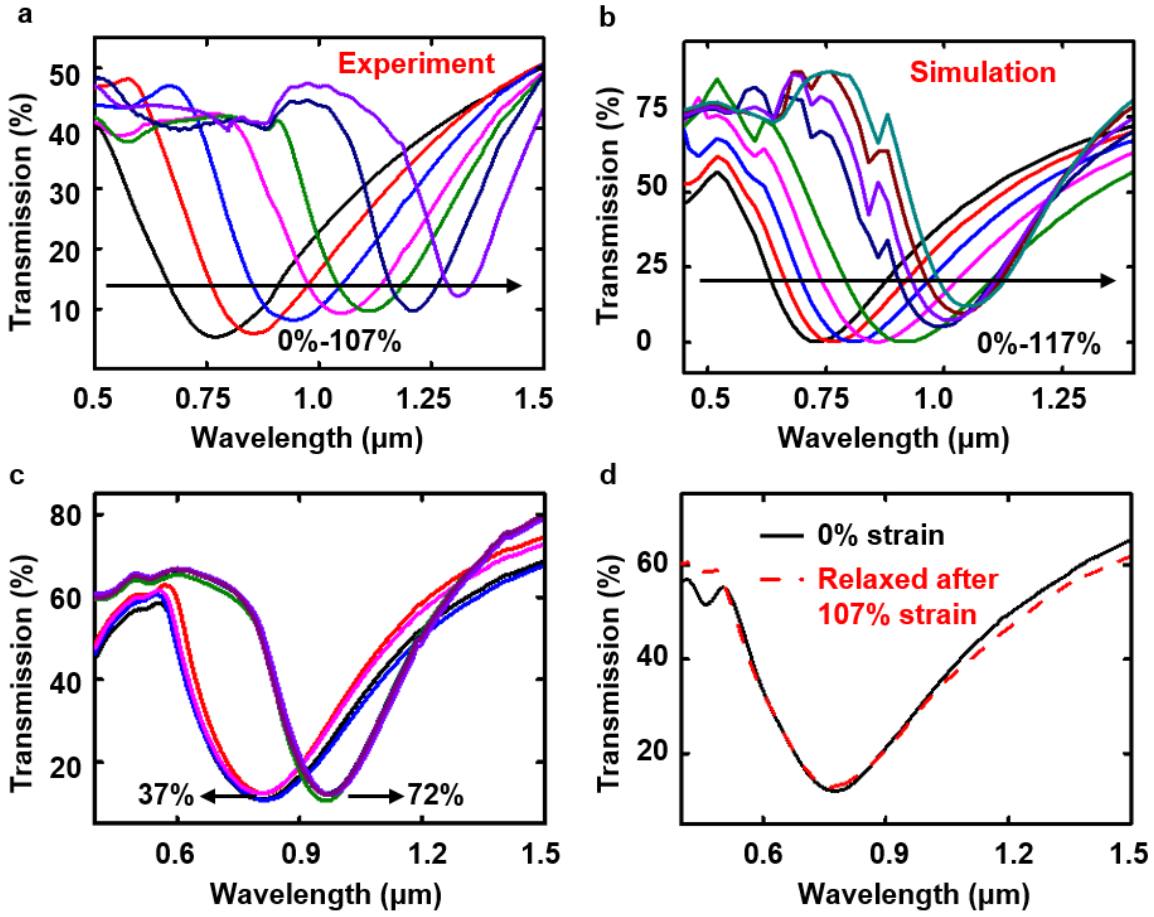

Figure 4.5 Transmission spectra of the Au nanodot array under different strains. (a) Experimental transmission spectra of the Au nanodot array under seven strains as shown in Fig. 2. (b) Simulated transmission spectra of the Au nanodot array under seven strains as shown in Fig. 2. (c) Four transmission spectra measurement of the Au nanodot array under 37% and 72% strains. (d) Transmission spectra of the Au nanodot array before stretching and after releasing from 107% strain.

4.6 References

1. Gansel, J. K. *et al.* Gold helix photonic metamaterial as broadband circular polarizer. *Science* **325,** 1513–1515 (2009)
2. Burckel, D. B. *et al.* Micrometer-scale cubic unit cell 3D metamaterial layers. *Adv. Mater.* **22,** 5053–5057 (2010).
3. Liu, N. *et al.* Three-dimensional photonic metamaterials at optical frequencies. *Nature Mater.* **7,** 31–37 (2008).
4. Decker, M., Zhao, R., Soukoulis, C. M., Linden, S. & Wegener, M. Twisted split‐ring ‐resonator photonic metamaterial with huge optical activity. *Opt. Lett.* **35,** 1593–1595 (2010).
5. Stewart, M.E. *et al.* Quantitative Multispectral Biosensing and 1D Imaging Using Quasi-3D Plasmonic Crystals. *P. Natl. Acad. Sci USA.*, **103**(46), 17143–17148 (2006).
6. Chanda, D. *et al.* Coupling of Plasmonic and Optical Cavity Modes in Quasi-Three-Dimensional Plasmonic Crystals," *Nat. Communications* **2**, 479 (2011).
7. Lal, S., Link, S., Halas, N. J. Nano-optics from Sensing to Waveguiding. *Nat. Photonics* **1**, 641–648 (2007)
8. Liu, N. *et al.* Infrared Perfect Absorber and Its Application as Plasmonic Sensor. *Nano Lett.* **10**, 2342—2348 (2010).
9. Khang, D.Y., Jiang, H., Huang, Y. and Rogers, J.A. A Stretchable Form of Single Crystal Silicon for High Performance Electronics on Rubber Substrates. *Science* **311**, 208-212 (2006).

10. Sun, Y., Choi, W.M., Jiang, H., Huang, Y.Y. and Rogers, J.A. Controlled Buckling of Semiconductor Nanoribbons for Stretchable Electronics. *Nature Nanotechnol.* **1**, 201-207 (2006).
11. Sun, Y., Kumar, V., Adesida, I. and Rogers, J.A. Buckled and Wavy Ribbons of GaAs for High-Performance Electronics on Elastomeric Substrates. *Adv. Mater.* **18**, 2857-2862 (2006).
12. Jiang, H., Khang, D.-Y., Song, J., Sun, Y., Huang, Y., and Rogers, J.A. Finite Deformation Mechanics in Buckled Thin Films on Compliant Supports. *P. Natl. Acad. Sci. USA.* **104**(40), 15607–15612 (2007).
13. Choi, W.M., Song, J., Khang, D.-Y., Jiang, H., Huang, Y.Y. and Rogers, J.A. Biaxially Stretchable "Wavy" Silicon Nanomembranes. *Nano Lett.* **7**(6), 1655-1663 (2007).
14. Sun, Y. and Rogers, J.A. Structural Forms of Single Crystal Semiconductor Nanoribbons for High-Performance Stretchable Electronics. *J. of Mater. Chem.* **17**, 832-840 (2007).
15. Gao, L. *et al.* Epidermal Photonic Devices for Quantitative Imaging of Temperature and Thermal Transport Characteristics of the Skin. Nat. Communications **5**, 4938 (2014).
16. Pryce, I. M. Highly Strained Compliant Optical Metamaterials with Large Frequency Tunability. *Nano Lett.* ***10***, 4222–4227 (2010)
17. Xu, X, *et al.* Flexible Visible-Infrared Metamaterials and Their Applications Highly Sensitive Chemical and Biological Sensing. *Nano Lett.* **11**, 3232–3238 (2011)
18. Aksu, S. Flexible Plasmonics on Unconventional and Nonplanar Substrates. *Adv.*

Mater. **23**, 4422–4430 (2011).

19. Vazquez-Mena, O. *et al.* High-Resolution Resistless Nanopatterning on Polymer and Flexible Substrates for Plasmonic Biosensing Using Stencil Masks. *ACS Nano* **6** (6), 5474–5481 (2012).
20. Millyard, M. G. Stretch-induced Plasmonic Anisotropy of Self-assembled Gold Nanoparticle Mats. *Appl. Phys. Lett.* **100**, 073101 (2012).
21. Kang, H. Durable Plasmonic Cap Arrays on Flexible Substrate with Real-Time Optical Tunability for High-Fidelity SERS Devices. *ACS Appl. Mater. Interfaces* **5** (11), 4569−4574 (2013).
22. Kim, D.-H. *et al.* Ultrathin Silicon Circuits With Strain-Isolation Layers and Mesh Layouts for High-Performance Electronics on Fabric, Vinyl, Leather, and Paper. *Adv. Mater*. 21, 3703–3707 (2009).
23. Kim, D.-H. *et al.* Materials for Multifunctional Balloon Catheters With Capabilities in Cardiac Electrophysiological Mapping and Ablation Therapy. *Nat. Mater*. **10**, 316- 323 (2011).
24. Xu, S. *et al.* Stretchable Batteries With Self-Similar Serpentine Interconnects and Integrated Wireless Recharging Systems. *Nat. Communications* **4**, 1543 (2013).
25. Jang, K.-I. *et al.* Rugged and Breathable Forms of Stretchable Electronics with Adherent Composite Substrates for Transcutaneous Monitoring. *Nat. Communications* **5,** 4779 (2014).
26. Chanda, D. *et al.* Large-area Flexible 3D Optical Negative Index Metamaterial Formed by Nanotransfer Printing. *Nat. Nanotechnol.* **6**, 402-407 (2011).

27. Gao, L. *et al.* Materials Selections and Growth Conditions for Large-Area, Multilayered, Visible Negative Index Metamaterials Formed by Nanotransfer Printing. *Adv. Opt. Mater.* **2**, 256-261 (2014).
28. Gao, L. *et al.* Nanoimprinting Techniques for Large-Area Three-Dimensional Negative Index Metamaterials with Operation in the Visible and Telecom Bands. *ACS Nano* **8**(6), 5535-5542 (2014).
29. Rechberger, W. *et al.* Optical properties of two interacting gold nanoparticles. *Opt. Commun.* **220**, 137–141(2003)
30. Maier, S. A. *et al.* Observation of near-field coupling in metal nanoparticle chains using far-field polarization spectroscopy. *Phys. Rev. B* **65**, 193408 (2002)

CHAPTER 5

EPIDERMAL PHOTONIC DEVICES FOR QUANTITATIVE IMAGING OF TEMPERATURE AND THERMAL TRANSPORT CHARACTERISTICS OF THE SKIN

5.1 Introduction

Characterization of temperature and thermal transport properties of the skin can yield important information of relevance to both clinical medicine and basic research in skin physiology. Here we introduce an ultrathin, compliant skin-like, or 'epidermal', photonic device that combines colorimetric temperature indicators with wireless stretchable electronics for thermal measurements when softly laminated on the skin surface. The sensors exploit thermochromic liquid crystals patterned into large-scale, pixelated arrays on thin elastomeric substrates; the electronics provide means for controlled, local heating by radio frequency signals. Algorithms for extracting patterns of colour recorded from these devices with a digital camera and computational tools for relating the results to underlying thermal processes near the skin surface lend quantitative value to the resulting data. Application examples include non-invasive spatial mapping of skin temperature with milli-Kelvin precision (±50 mK) and sub-millimetre spatial resolution. Demonstrations in reactive hyperaemia assessments of blood flow and hydration analysis establish relevance to cardiovascular health and skin care, respectively.

5.2 Experiments

5.2.1 An Overview of Device Fabrication Scheme

The e-TLC thermal imagers use a multilayer design that includes (1) a thin (20 μm) black elastomeric membrane that serves as a mechanical support and an opaque background for accurate colorimetric evaluation of the TLC materials, (2) an array of dots of TLC (i.e. pixels, with 25 μm thicknesses, and diameters of either 250 or 500 μm, spaced by 250 or 500 μm), with an optional interspersed array of dots with fixed colors (with diameters of 400 μm, spaced by 600 μm) for calibration, both delivered to the surface of the black elastomer by transfer printing, (3) a thin (30 μm) overcoat of a transparent elastomer for encapsulation and (4) optional electronics in thin, stretchable configurations mounted on the back surface for active functionality described subsequently. (Details appear in **Fig. S16**.) The TLC material consists of microencapsulated chiral nematic liquid crystals. The small sizes and large spacings of the TLC and calibration pixels, taken together with the low modulus, elastic properties of the substrate, encapsulation layer and electronics, yield soft, compliant mechanics in the overall e-TLC system. These properties are well suited for mounting on the skin.

5.2.2 Detailed Experiment Steps

Device calibration and test for noise level. An e-TLC device was placed on a metal plate with black matt finish on a hotplate. Two white fluorescent light sources were

placed on opposite sides of the device for illumination in a manner that avoided specular reflection. A digital camera (Canon Mark II 5D) and an infrared camera (FLIR ExaminIR) placed side-by-side were focused on the same area of the device at a distance of B30 cm. The angle between the cameras and each of the light sources was 90 degree. The device was heated to 40 ℃ on the hotplate and then the hotplate was turned off. During the cooling process, high-resolution images were collected every 10 s with the digital camera; the infrared camera captured frames at a rate of 12.5 s^{-1}. The process of cooling from 40 ℃ to 32 ℃ lasted about 20 min. The colour information of the TLC was extracted from 33 ℃ to 39 ℃ with steps of 0.5 ℃. The set of algorithms developed to accomplish this task are based on computer vision OpenCV (http://opencv.org/) library. The main functions are (in alphabetic order) as follows: 'adaptiveThreshold', 'cvtColor', 'dilate', 'drawContours', 'erode', 'findContours', 'GaussianBlur', 'getStructuringElement', 'imread', 'inRange', 'matchShapes', 'minEnclosingCircle' and 'threshold'. In HSV colour space, the light intensity information is stored in the 'value' channel and is completely separated from the colour information, which is encoded in the 'hue' and the 'saturation' channels. Hue and saturation are, therefore, a natural basis for temperature calibration, as they are not strongly affected by the change in illumination intensity. Temperature calibration was constructed by means of two-dimensional linear fit. The core function used in the process was 'lstsq' from the linear algebra module of Numerical Python (http://www.numpy.org/). Any combination of hue/saturation values can be assigned to a temperature value. Even for materials that are not temperature sensitive, such as the calibration colour pixels, their hue/saturation can be treated as a specific temperature for consistency of analysis. To test the noise level and precision of the system, the hotplate

temperature was set at a fixed value; temporal fluctuations of TLC colour, calibration dot colour and infrared emission were recorded using the two cameras over a period of 15 min. The colour changes were converted to temperature fluctuation and compared with infrared fluctuation directly.

A volunteer (female, 27 years old) reclined in a chair with her left forearm secured gently to an arm rest using Velcro strips to reduce movement. A pressure cuff was secured around the subject's left bicep. An e-TLC device was placed on the skin of the left wrist approximately above the ulnar artery. Applying puffs of compressed air ensured full, conformal contact. Infrared and digital cameras placed 30 cm above the subject's left wrist were focused on the location of the device while illuminated with white fluorescent lights. The subject was instructed to relax for 5min. The cuff was inflated to a pressure of 250mm Hg for 160 s. Continuous high-resolution colour images and infrared temperature measurements were then collected with the two cameras as the occlusion started and was then released. The total duration of the measurement was 300 s.

Thermal conductivity was determined by analysing the spatial distribution of temperature for a few seconds immediately after activation of a Joule heater in an active e-TLC device. To validate the computational models, an active e-TLC device was floated on the surface of a mixture of ethylene glycol/water preheated to 33 ℃. A constant voltage supplied to the e-TLC Joule heating element created a steady-state temperature rise of a few degrees at the location of the heater. Images were then collected with a digital and infrared camera set up above the device with only white fluorescent light

sources. The spatial decay of temperature in the e-TLC was recorded by analysis of images from the infrared camera and from colour images of the device. The same experiment was performed on a volunteer's forearm skin. Here, different hydration levels were achieved by applying various amounts of lotion to the measurement location, before application of the active e-TLC device. Immediately after image capture, the e-TLC device was removed and a hydration meter was used to determine the actual moisture level (averaged from five readings). Measurements of thermal diffusivity used a wireless, active e-TLC, with a transmission antenna located ~10 cm away and adjusted to achieve a peak change in temperature of a few degrees (RF power below 2.5Wkg^{-1} at frequencies between 1.95 and 2.35 GHz, tuned to match the response of the receiver antenna on the e-TLC). Both digital and infrared cameras were focused on the device with a distance of 30 cm. Videos with 60-s duration recorded the changes in temperature associated with activation and de-activation of the heater. The experiment was validated using the ethylene glycol/water system and then repeated on skin with different hydration levels, in procedures otherwise similar to those for the thermal conductivity measurements.

5.3 Results and Discussions

Figure 5.1a shows an e-TLC on the skin of the forearm when twisted and gently poked with a mildly heated rod. Small interfacial stresses that follow from the low effective modulus and small thickness of the device enable adequate adhesion through van der Waals interactions alone. The collapse of a free-standing device under its own weight, as shown in the right frame, provides qualitative evidence of these

mechanical characteristics. **Figure 5.1b** shows a pair of magnified images of e-TLC devices; those on the bottom include interspersed color calibration pixels consisting of red, green and blue dye in a non-toxic acrylic base (aqueous dispersion of organic pigment and acrylic polymer, Createx). A completed device of this latter type placed on the curved surface of the back of the hand appears in **Figure 5.1c**. As previously mentioned, the backside of the black elastomer substrate provides a mounting location for stretchable electronics. The image in **Figure 5.1d** shows an example of an e-TLC device with a wireless system for remote delivery of controlled levels of heat, integrated in this way. The folded configuration reveals part of the serpentine antenna structure (inset). An illustration of this system, in the form of three dimensional finite element analysis (3D-FEA), appears in Fig. 1e. The antenna captures incident radio frequency (RF) energy to power a Joule heating element (inset, **Fig. 5.1e**). The result provides well-defined, localized increases in temperature, as revealed in the pattern of colors in the TLC pixels of **Figure 5.1f** and the infrared images of **Figure 5.1g**. As described subsequently, the results from measurements under such conditions allow determination of the thermal conductivity and thermal diffusivity of the skin.

A key design goal is to produce e-TLC systems that induce minimal perturbations to the skin, thereby avoiding irritation, enhancing wearability and ensuring accurate measurement capabilities. The mechanical and thermal properties are particularly important in this context. Experimental and theoretical studies of the former reveal low modulus, elastic characteristics over large ranges of strain. **Figure 5.2a** shows the stress/strain responses of an e-TLC device under static uniaxial testing. The results agree

well with the predictions of 3D-FEA. In particular, the TLC pixels (~221 MPa) and elastomeric substrate (~131 kPa) yield an effective modulus (~152 kPa and 178 kPa from 3D-FEA and experiment, respectively) that is only slightly larger (by 16-35%) than the intrinsic value associated with the bare elastomer, and is comparable to that of the epidermis itself. The TLC pixels experience ultra-low strain (e.g., <2%) even under extreme stretching (e.g., 200%), as shown in **Figure 5.2b**. The resulting stretchability (>200%) of the device is >40 times larger than that (~5%) of the TLC material. Negligible deformations of the TLC pixels, as observed in experiment and FEA (**Fig. 5.2b**), allow approximations for simple, but quantitatively accurate, analytical solutions of the mechanics (**Fig. S17a**). The thicknesses, bending stiffnesses, effective moduli and stretchability of these devices are 50 μm, 3.0 nN·m, 178 kPa and beyond 200%, respectively; these characteristics are superior than those of typical, commercially available TLC sheets (Hallcrest) whose corresponding properties of ~125 μm, 570,000 nN·m, 3.3 GPa and ~5% (Hallcrest). The differences are significant, at a qualitative level of importance for deployment on the skin. The collective mechanical characteristics allow largely unconstrained natural motions of the skin, including wrinkling and stretching even in challenging regions such as the knees and elbows. Addition of calibration pixels reduces the stretchability and increases the modulus (**Fig. S17b**), but nevertheless enable elastic strain levels (50%) that exceed those that can be tolerated by the epidermis (linear response to tensile strain up to 15%, nonlinear to 30%, and rupture at >30% [1, 2]). Incorporating a wireless electronic heating system further reduces the accessible strain, but with an elastic stretchability of nearly 20%, which is useful for many applications (see **Fig. S18**) [2, 3]. Although the characteristics of the antenna change with

mechanical deformation, experiments indicate that uniaxial stretching (up to 50%) does not disrupt the overall function or the efficiency of power harvesting (see **Fig. S19**); bending decreases the efficiency only slightly.

The thermal characteristics of the systems define the thermal load on the skin, as well as the overall time response. For an active e-TLC device, the thermal mass per unit area is ~7.7 $mJ \cdot cm^{-2} \cdot K^{-1}$. This value corresponds to an equivalent of skin thickness of ~20 μm, which corresponds to only 25% of the thickness of the epidermis itself [4]. The small thermal mass minimizes changes in skin temperature and hydration level induced by presence of the device. Temperatures measured with an infrared camera on the forearm adjacent to an e-TLC and directly underneath it (**Fig. S20a-c**) show minimal differences. The effects of the device on skin hydration (**Fig. S20d**) are also small. For monitoring of transient processes, the time response of the system is important. For geometries and materials investigated here, the response time for an e-TLC device is dominated by the thickness and thermal properties of the black elastomer substrate. Transient measurements reveal response times of less than ~30 ms, consistent with estimates developed using analytical models (**Fig. S21**). The intrinsic switching times for most TLC materials are ~3-10 ms. [5-8]

Reflection mode spectroscopic characterization (Zeiss Axio Observer D1) of the stead-state response of the TLC material to changes in temperature between 32 ℃ - 39 ℃ show expected behaviors, as in **Figure 5.3a**. With proper calibration, described next, the temperature extracted from the hue and saturation values determined using a typical

digital camera (Canon 5D Mark II) with the e-TLC device held at a nominally constant temperature exhibits a standard deviation of ~30 mK over a measurement time of 760s in **Figure 5.3b**. This value is comparable to that observed from temperature readings simultaneously determined with an infrared camera (~50 mK). Equivalent temperatures extracted from analysis of color recorded at the calibration pixels (red, green, blue) show fluctuations with similar magnitudes, as summarized in **Figure 5.3c**. These observations suggest that the process of image capture and color analysis enables levels of precision that are comparable to those of infrared cameras, not limited by the physics of the TLC. Detailed calibration plots and information on temperature extraction appear in **Figure S22**.

Analysis of hue/saturation/value obtained from the digital camera represents the simplest and most straightforward analysis approach. Sophisticated algorithms based on computer vision techniques are advantageous, not only for color determination but for full pixelized analysis of complete e-TLC devices. **Figure 5.3d** illustrates an example of a process that exploits computer vision code (OpenCV), in which an image of an e-TLC device that consists of a 7x7 pixel array undergoes a set of color extraction and data transformation steps. A Gaussian filter first reduces noise through smoothing to yield a gray scale rendering for use with an adaptive threshold that compensates for illumination non-uniformities. The output is a binary mask containing value "1" at bright areas and "0" elsewhere. A two-step erode/dilate process eliminates small speckles that arise from defects. A full list of contours can be extracted from this "clean" image, in which each contour bounds a single pixel in the array. An enclosing circle function uses the contours as

inputs to define the pixel positions, for extraction of color information from the original, unprocessed image. A typical calibration that relates hue and saturation values extracted in this manner to temperature evaluated with an infrared camera appears in **Figure 5.3e**. The biggest advantage of using hue/saturation/value (HSV) color space instead of RGB is that color information is encoded only in two (hue and saturation) channels. They are resilient to the change in lightning conditions since that information is stored separately in value channel. Any possible hue/saturation combination can be represented by a point in polar coordinates where radial coordinate corresponds to saturation and angular one to hue. The positions of the calibration set are marked with the dots painted with corresponding hue value. These points were used to construct temperature calibration by means of two dimensional linear fit. Now for any hue/saturation combination can be assigned temperature value which is shown in the plot with color gradient.

Scaled implementation of this process is summarized in **Figure 5.3f**. Here, a full e-TLC device on a portion of the wrist where near-surface veins are located reveals associated variations in temperature of the epidermis. The hue values across the e-TLC yield three dimensional temperature contour plots that reflect the blood vessels with high spatial resolution (**Fig. 5.3g**). A direct comparison with temperature distributions measured in the same region using an infrared camera (**Fig. 5.3h**) exhibits excellent correspondence. Plots of the temperature extracted from these two sets of results at the locations indicated by the dashed red lines in **Figure 5.3g, h** appear in **Figure 5.3i**. These results suggest suitability of e-TLC systems for mapping of vascular distributions in applications

such as screening for deep venous thrombosis, without the need for costly infrared camera systems.

In such practical situations, the lighting conditions can strongly affect the precision and accuracy of the temperature determination [9-12]. In particular, the hue and saturation depend on the type of light source used for illumination. The color calibration pixels provide a means to compensate for such effects, since their known colors are influenced by the lighting in the same way as the TLC. As a result, algorithms that account for shifts in the apparent colors of these calibration pixels yield a set of numerical compensations that can restore their actual, known colors. Applying the same compensations to the TLC pixels yields a temperature evaluation process that is independent of illumination conditions, within some reasonable range. Effects of three different lightning conditions appear in **Figure 5.4**. Red, green and blue color calibration pixels, interspersed across the entire device, are present in this active e-TLC sample. **Figure 5.4a** presents an image of the device, with circles that indicate the positions of the TLC pixels. A Joule heating element is present in the center region. Fluorescent, light emitting diode (LED) and halogen (Figs. 13c, 13d and 13e) light sources provide a range of practical examples. The corresponding temperature calibration data appear in **Figure 5.4b**, the circles correspond to the hue/saturation values of TLC pixels at different temperatures used to create calibration fits for specific lightings. The stars mark the illumination effect on solid color pixels. Red pixels are located at ~5 °, green are at ~100 ° and blue are at ~240 °. Since the solid colors are known it should be possible to extract the compensation factor for random light condition. Applying it to TLC pixels should make the temperature

detection process much less dependent on specific calibration corresponding to particular lightning. This will be subject of future research. **Figure 5.4f** presents computed temperatures evaluated along lines that pass through the central region while the Joule element is activated. The results are comparable for all three lighting sources. To demonstrate the importance of proper calibration, **Figure 5.4g** summarizes data that exploit the fluorescent sources. Significant discrepancies occur, as might be expected due to the different color temperatures of the halogen and LED sources. The resulted discrepancies in temperature reading are reflected not only in the temperature maxima, but also the temperature profile shape and noise level, which again emphasizes the importance of proper calibration and compensation system.

As suggested by the active e-TLC results in **Figure 5.4**, the local Joule heating element enables additional measurement capabilities. In particular, spatial and temporal variations in temperature at locations near this heater can be used, with thermal models, to extract the thermal conductivity and diffusivity of the skin. Increases in temperature of a few ℃ can enable accurate evaluation. The thermal conductivity (*k*) can be determined by comparing measured steady state distributions in temperature to axis-symmetric thermal conduction models (**Fig. S23a, b, e**). The skin layer (homogenized from real skin and the underlying tissues, with the thickness >2 mm) are usually much thicker than the PDMS layer (with a thickness of ~60 μm), such that it can be considered as infinitely thick. The steady-state heat conduction equation is $\partial^2 T/\partial x^2 + \partial^2 T/\partial y^2 + \partial^2 T/\partial z^2 = 0$ for both the PDMS and skin, where T is the temperature. The square shaped resistor ($a_{Resistor} \times b_{Resistor}$) serves as the heat source,

with the heat generation Q that pumps into the PDMS and skin. This can be modeled as a surface heat flux ($q_0 = Q/\left(a_{Resistor} b_{Resistor}\right)$) for the bilayer system, i.e. $q_0 = q_{zPDMS}\big|_{z=-H_{PDMS}} - q_{zSkin}\big|_{z=-H_{PDMS}}$, for the region occupied by heat source. The free, top surface of the PDMS has natural convection with the surrounding air (T_∞), i.e. $q_{zPDMS}\big|_{z=0} = h\left(T - T_\infty\right)$, with h denoting the heat transfer coefficient. The continuity conditions include [T] = 0 and [qz] = 0 across the PDMS/skin interface. By adopting the approach of double Fourier transform, the temperature at the sensor plane ($z = -H_{Sensor}$) is obtained as

$$T_{Sensor-layer} = T_\infty + \frac{4q_0}{\pi^2 k_{PDMS}} \cdot \int_0^\infty \cos\left(\omega x\right) \mathrm{d}\omega \int_0^\infty \frac{\sin\frac{a_{Resistor}\omega}{2} \sin\frac{b_{Resistor}\zeta}{2} \left(\mathrm{e}^{\eta H_{Sensor}} + \frac{k_{PDMS}\eta - h}{k_{PDMS}\eta + h} \mathrm{e}^{-\eta H_{Sensor}} \right) \cos\left(\zeta y\right) \mathrm{d}\zeta}{\omega\zeta\eta \left[\left(1 + \frac{k_{Skin}}{k_{PDMS}}\right) \mathrm{e}^{\eta H_{PDMS}} - \frac{k_{PDMS}\eta - h}{k_{PDMS}\eta + h} \left(1 - \frac{k_{Skin}}{k_{PDMS}}\right) \mathrm{e}^{-\eta H_{PDMS}} \right]} \quad (3)$$

Equation (3) corresponds to the temperature solution of the forward thermal conduction problem, given the thermal conductivity of the skin layer. The parameters adopted in experiments include $a_{Resister}$=$b_{Resister}$=0.5 mm, h=5 W•m^{-2}•K^{-1}, H_{sensor}=30 μm, H_{PDMS}=60 μm, k_{PDMS}=0.16 W•m^{-1}•K^{-1}, and the thermal diffusivity α_{PDMS}=1.07 m^2•s^{-1}. For a representative value of k_{skin}=0.31 W•m^{-1}•K^{-1} and Q=3.8 mW, the distribution of temperature at the sensor plane, as given by Eq. (3), is shown in Fig. S8c, which agrees reasonably well with FEA results (**Fig. S23d**). The temperature profile along the x axis (in **Fig. S23e**) is in quantitative agreement with the FEA results. The relatively large discrepancy at the center region is mainly attributed to the assumption of homogeneous heat generation q_0 through the entire

heater, adopted for the aim of model simplification. **Figure S23e** also shows the temperature gradient is obvious in the region within a distance of ~4 mm from the heater center. For the sensors far from the heater (0.5 by 0.5 mm), the temperature distribution can be approximated by the simple solution of a point heat source, i.e.

$$T_{sensor-layer} \approx T_{\infty} + \frac{Q}{2\pi kr} \tag{4}$$

where r is the distance from the heat source, Q is the heat generated by the Joule heating element, and T_{∞} is the temperature of surrounding air. An example appears in **Figure 5.5a**, calibration can be performed through measurements of materials with known thermal conductivity (**Fig. 5.5b**). **Figure 5.5c** indicates excellent correspondence between thermal conductivity of the skin evaluated with an active e-TLC and hydration levels determined with a moisture meter (Delfin MoistureMeterSC) that relies on electrical impedance. The quantitative values of k fall within a range that is consistent literature values determined by subcutaneous thermocouples and high speed radiometer etc. [13] By simplifying the heating element as a point heat source turning on the t=0, the transient temperature variation can be analytically solved as

$$T_{Sensor-layer}(t) \approx T_{\infty} + \frac{Q}{2\pi kr} erfc\left(\frac{r}{\sqrt{4\alpha t}}\right) \tag{5}$$

where α is the thermal diffusivity of the skin, and $erfc(x)$ is the complementary error function. Therefore, transient temperature data associated with activation or deactivation of the Joule heating element can be used to determine thermal diffusivity, α, as illustrated in **Figure 5.5d** (see **Fig. S23a,b,f**). For the representative value of k_{skin}=0.31 $W \cdot m^{-1} \cdot K^{-1}$,

α_{skin}=1.14 $m^2 \bullet s^{-1}$, and Q=3.8 mW, the time dynamic temperature given by Equation 5 agree remarkably well with FEA results, as shown in **Fig. S23f**, for three different points (with a distance of 0.5, 1.0 and 2.0 mm from the origin). Based on Equation 5 we can determine the thermal diffusivity based on the transient temperature data from the e-TLC device. Here, a wireless active e-TLC system serves as the measurement vehicle. The time dependence of the temperature, rather than the absolute values, is sufficient for extraction of diffusivity. **Figure 5.5d** gives an example of temperature profile at the sensor with a distance of 0.5 mm from the heater, where the analytic curve with the thermal diffusivity of 0.43×10^{-7} m^2/s gives the best match with the experimental data. As with conductivity, the device can be calibrated using samples with known diffusivity (**Fig. 5.5e**). The device operates at frequencies of ~2 GHz with maximum power inputs of ~2.5 W/kg for the subject of the studies described here (i.e. one third of the power limit recommended by the Federal Communications Commission's guidelines). The values also correspond closely to the hydration level, as shown in **Figure 5.5f**. As with k, the values of α are consistent with literature reports based on techniques such as opto-thermal measurement. [14] The values of k and α can be combined to yield the product of the density (ρ) and heat capacity (c) of skin, based on the relation ($c\rho=k/\alpha$). The calculations (See **Fig. S23g**) show that the heat capacity increases slightly with the increase of hydration level (assuming that ρ is approximately constant), which is consistent with expectation since the heat capacity (~4.2 J/g/K) of water is larger than the human tissue (e.g., ~3.7 J/g/K for dermis, ~2.3 J/g/K for fat). [15]

Spatio-temporal mapping even with passive e-TLC systems yields useful information on blood circulation [16, 17], maximal percentage increase in blood flow rate after occlusion

[18], and duration of reactive hyperaemia [19]. Measurements of temperature fluctuations above the ulnar artery and adjacent veins serve as an important part of a reactive hyperaemia protocol. Here, the flow of blood is temporarily occluded by a pressure cuff on the upper arm, followed by abrupt release. **Figure 5.6a** and **5.6b** summarize results of measurements performed with an e-TLC device and an infrared camera. **Figure 5.6c** presents representative frames of temperature distributions captured at 20 s intervals throughout the experiment. Occlusion, which begins at t=0 s, causes the temperature of the skin above the ulnar artery and adjacent areas to decrease drastically owing to lack of incoming blood flow and loss of heat to the environment. The minimum temperature is achieved at t=160 s; at this time, the occlusion is released and blood flow resumes. Sharp temperature increases occur in areas above the blood vessels, as shown in **Figure 5.6c**, until the temperature stabilizes. The responses of pixels across the array of the e-TLC vary widely depending on their distance from the blood vessels. The maximum temperature fluctuations are ~1.2 ℃ and occur immediately above the ulnar artery; the minimum temperature fluctuations are ~0.4 ℃ and occur at locations away from near-surface blood vessels. Direct comparisons of spatio-temporal variations in temperature obtained from the e-TLC show quantitative agreement with results from an infrared camera (Fig. S13). Fig. 6d and 6e show temperature variations along horizontal and vertical lines illustrated in the right image of **Figure 5.6a**. A thermal model of the human wrist (**Fig. S25**) that accounts for both the time-dynamic effect of occlusion and the thermal diffusion from the ulnar artery can capture the effects revealed in the measurements (**Fig. 25f, g**) and enable extraction of additional physiological information.

A two-dimensional (2D), transient, heat transfer model of human wrist was developed, which considers the various tissues surrounding the ulnar artery, and quantitatively characterizes the heat exchange between the blood flow and the surrounding tissues. **Figure S25a** and **S25b** show the schematic illustration of the tissue geometry, in which a circular cross section is adopted for the wrist to simplify the analyses. The blood at body temperature flows through the circular artery embedded in the fat layer, heating the surrounding tissues. The heat exchange between the blood flow and the fat layer across the artery wall is described with a heat convection model, [16, 17] which assumes the exchanged heat flux (q) to be proportional to the blood flow rate, i.e.

$$q = \frac{\rho_b c_{pb} \omega_b(t)}{\pi D_{artery}} \left(T_{body} - T_s \right) \tag{6}$$

The temporal variation of blood flow can be described with a piecewise, exponential type function [20, 21], corresponding to the three stages of the process: pre-occlusion, vascular occlusion, and reperfusion.

$$\begin{aligned}
&\omega_b^I(t) = \omega_0, \ t \le t_{occ,st} \\
&\omega_b^{II}(t) = (\omega_0 - \omega_s)\exp(-t/\tau_0) + \omega_s, \ t_{occ,st} < t \le t_{occ,end} \\
&\omega_b^{III}(t) = \begin{cases} (\omega_{\max} - \omega_s)\sin^2\left[\pi\left(t - t_{occ,end}\right)/\left(2t_{dw}\right)\right] + \omega_s, \ t_{occ,end} < t \le \left(t_{occ,end} + t_{dw}\right) \\ (\omega_{\max} - \omega_f)\exp\left[-\left(t - t_{occ,end} - t_{dw}\right)/\tau_h\right] + \omega_0, \ t > \left(t_{occ,end} + t_{dw}\right) \end{cases}
\end{aligned} \tag{7}$$

Except for $t_{occ,st}$ and $t_{occ,end}$, which are known in experiments ($t_{occ,st}$ = 0 s, $t_{occ,end}$ = 160 s), there are six parameters in this model of reactive hyperemia which can be varied to simulate the temperature history of blood perfusion. The aim of the thermal analyses is to obtain an optimized set of parameters that can minimize the average difference between the simulations and experiment data of temperature-time profile at those sensors with a distance

≤7 mm from the artery (**Fig. 5.6g**). **Figure 5.6g** shows that the calculated temperature history based on the thermal model agrees with experiment at all six of the pixels near the artery (i.e., distance <6 mm). Discrepancies at the two most distant sensors can be attributed to the neglect of heating associated with a nearby vein (~13 mm from the artery) in the model. For vessel diameters and depths that lie within reported ranges, the peak blood flow velocity after occlusion is calculated to be 58.8 cm/s, representing a three-fold increase over the baseline of 19.6 cm/s, with a reactive hyperemia duration of 144 s. These values match those reported in the literature for a person with low cardiovascular risk [18, 19].

5.4 Conclusions

Epidermal photonic systems, as embodied by the e-TLC devices introduced here, offer strong potential for characterization of the skin and, by extension, important parameters relevant in determining cardiovascular health and physiological status. These same capabilities can be useful in wound treatment and monitoring during a healing process, cancer screening, core body temperature assessments and others of clinical relevance. In all cases, the ability to wear the devices continuously, over days or weeks, and to perform readout and power delivery via a conventional smartphone, represent uniquely enabling features. Photonic operation in the red and near infrared could enable use in near-surface implantable diagnostics.

5.5 Figures

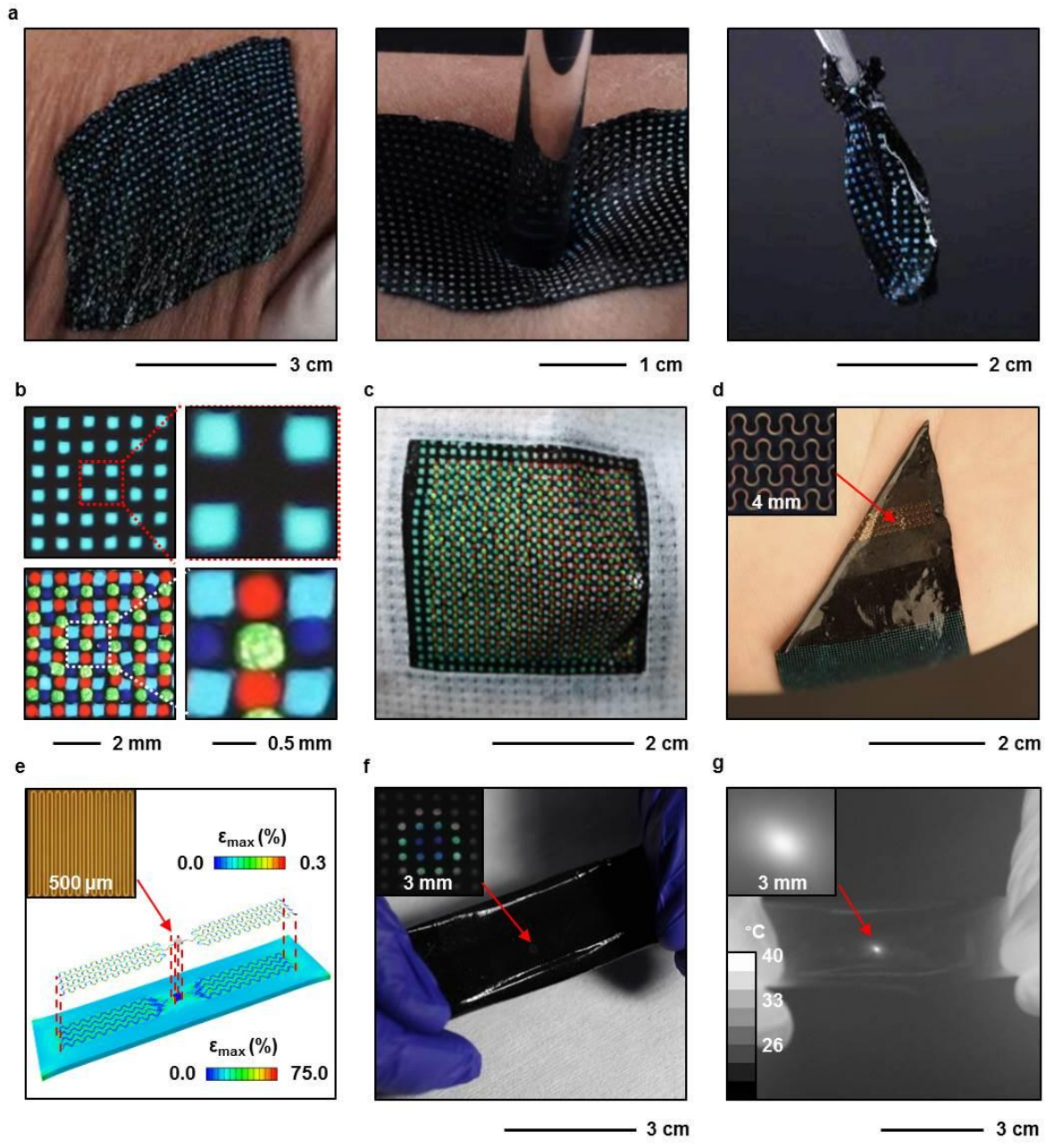

Figure 5.1 Pictures, micrographs and design features of an 'epidermal' thermochromic liquid crystal (e-TLC) thermal imaging device. (a) Picture of devices deformed by pinching the skin in a twisting motion (left), poking with a warm glass rod while on skin

(Fig. 5.1 continued) (middle) and collapsing under its own weight while free-standing (right). (b) Magnified view of a device operating in the blue region of the spectrum, without (top) and with (bottom) integrated patterns of dots that have fixed colors for calibration. (c) Picture of an e-TLC device with calibration system, operating the curved surface of the skin. (d) Picture of a device that includes a radio frequency antenna and Joule heating element on its back surface, folded over and resting on palm, with an enlarged view of the serpentine antenna structure (inset). (e) Schematic illustration of finite element modeling results for an e-TLC device with wireless heater under tensile strain, with magnified view of the Joule heating element (inset). (f) Image of an active, wireless e-TLC device collected while exposed to RF power in air, with magnified view of the color changes induced by the heater (inset). (g) Infrared image of the same device under similar conditions, with magnified view in the region of the heater (inset).

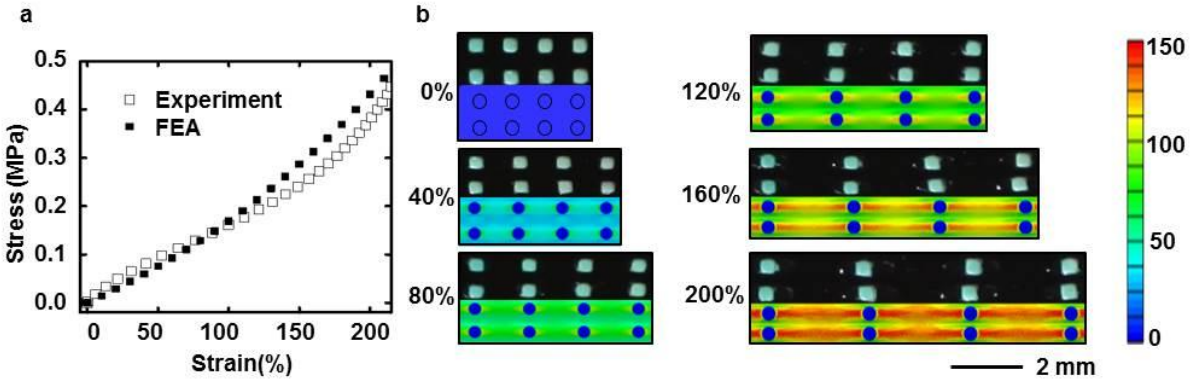

Figure 5.2 Experimental and computational studies of the mechanical properties of e-TLC devices. (a) Measurements and analytical computations of stress-strain responses of a device. (b) Comparison between images and three dimensional finite element modeling of a representative region of e-TLC device under different levels of tensile strain.

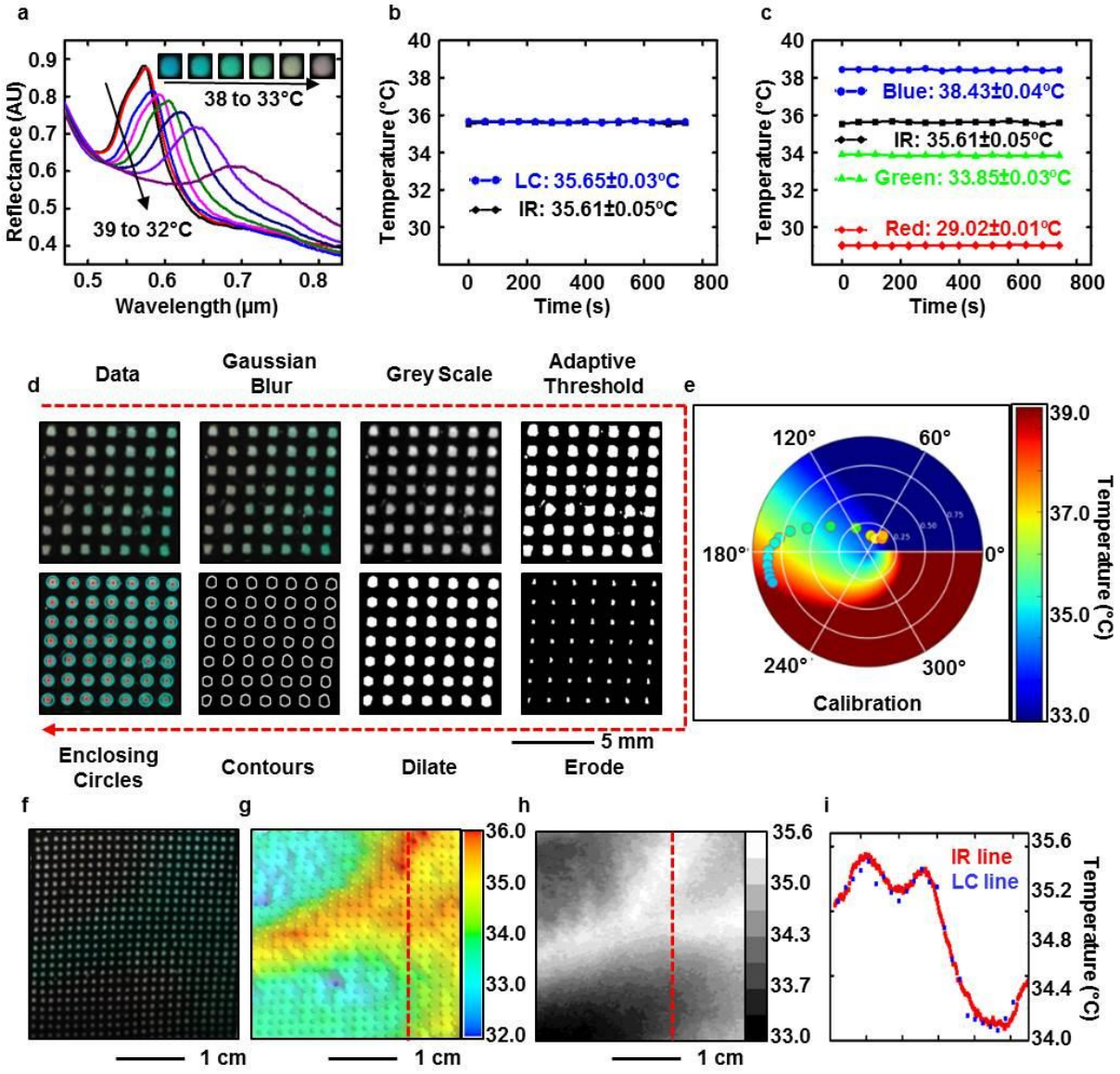

Figure 5.3 Calibration and use of e-TLC devices for precision thermal imaging on the skin. (a) Reflectance measured at a single pixel from 32 ℃ to 39 ℃ and corresponding images for 33 ℃ to 38 ℃ (inset). (b) Temporal variations in temperature extracted from digital color analysis of an e-TLC held, nominally, at a constant temperature. (c) Temporal variations in apparent temperature determined from color analysis of calibration pixels in an e-TLC device.

(Fig. 5.3 continued) Frames b and c also show results obtained with an infrared camera. (d) Illustration of the steps for processing digital images of e-TLC devices, demonstrated on a representative 7x7 array of pixels. (e) Color-temperature calibration determined using hue analysis. (f) Images of an e-TLC device that consists of a 26x26 array of pixels, conformally mounted on the wrist. (g) 3D rendering of the temperature distribution extracted from the color information obtained by hue value analysis of digital images of the device. (h) 2D rendering of temperature captured by an infrared camera at the same time and at the same location as in g. i, Line-cut temperature profiles extracted from the data of g and h.

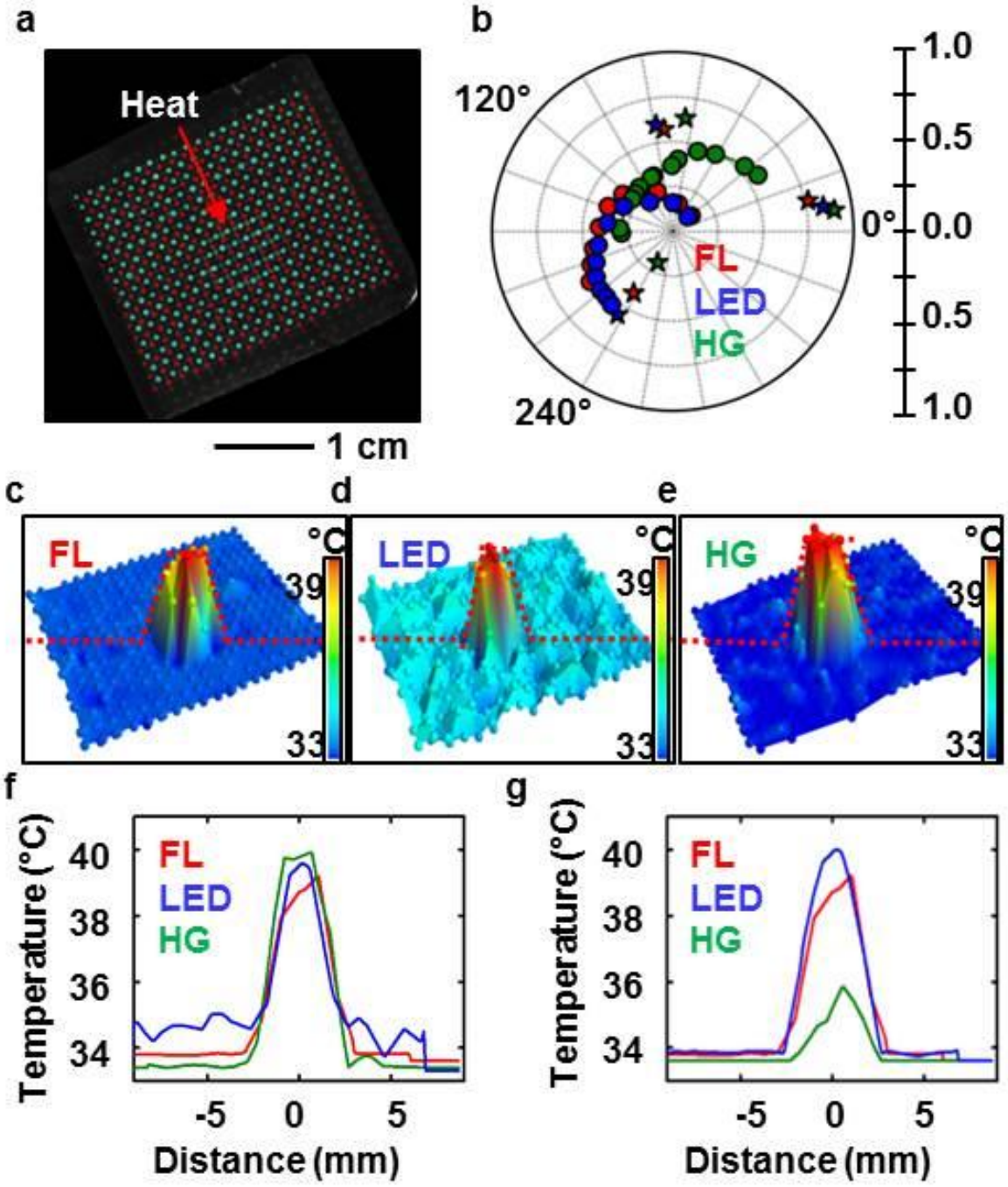

Figure 5.4 Temperature analysis with an e-TLC device that incorporates an array of color calibration pixels co-located with sensing pixels, evaluated under different illumination conditions. (a) Image of a device immediately after local heating at the center of the array. (b) Hue and saturation values extracted for the calibration (stars) and sensing pixels

(Fig. 5.4 continued) (dots; red –illumination with a fluorescent light; blue – illumination with a light emitting diode; green – illumination with a halogen lamp). 3D rendering of color-corrected temperatures determined with (c) white fluorescent light (FL), (d) white light-emitting diode (LED), (e) halogen light (HG). (f) Line graphs of results collected along the dashed lines shown in c-e. (g) Results similar to those in f, but without color correction.

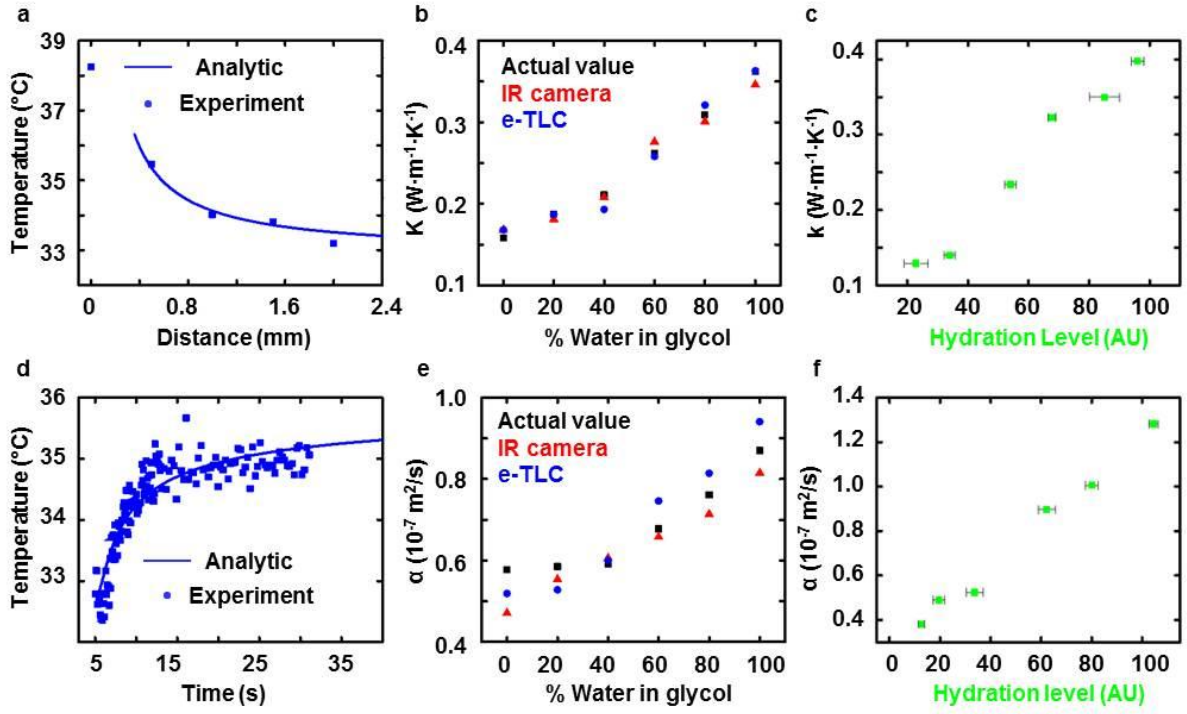

Figure 5.5 Determination of thermal conductivity and thermal diffusivity of the skin using active e-TLC devices. (a) Example of temperatures (symbols) as a function of distance from the position of local heating in an active e-TLC device and corresponding best fit modeling results (analytic; line), for determining the thermal conductivity. (b) Thermal conductivity of water/ethylene glycol solutions evaluated using an active e-TLC device, with comparison to values obtained from the literature and from analysis of temperatures

(Fig. 5.5 continued) determined with an infrared camera. (c) Thermal conductivities measured with an active e-TLC device on the skin at different levels of hydration, separately measured with a commercial moisture meter. The error bars represent average standard deviations of measurements obtained with the moisture meter. (d) Example of temperatures (symbols) as a function of time for a location near a wireless heater in an active e-TLC device, and corresponding best fit modeling results (analytic; line) for determining the thermal diffusivity. (e) Thermal diffusivity of water/ethylene glycol solutions evaluated using an active e-TLC device, with comparison to values obtained from the literature and from analysis of temperatures determined with an infrared camera. (f) Thermal diffusivities measured with an active, wireless e-TLC device on the skin at different levels of hydration, separately measured with a commercial moisture meter. The error bars represent average standard deviations of measurements obtained with the moisture meter.

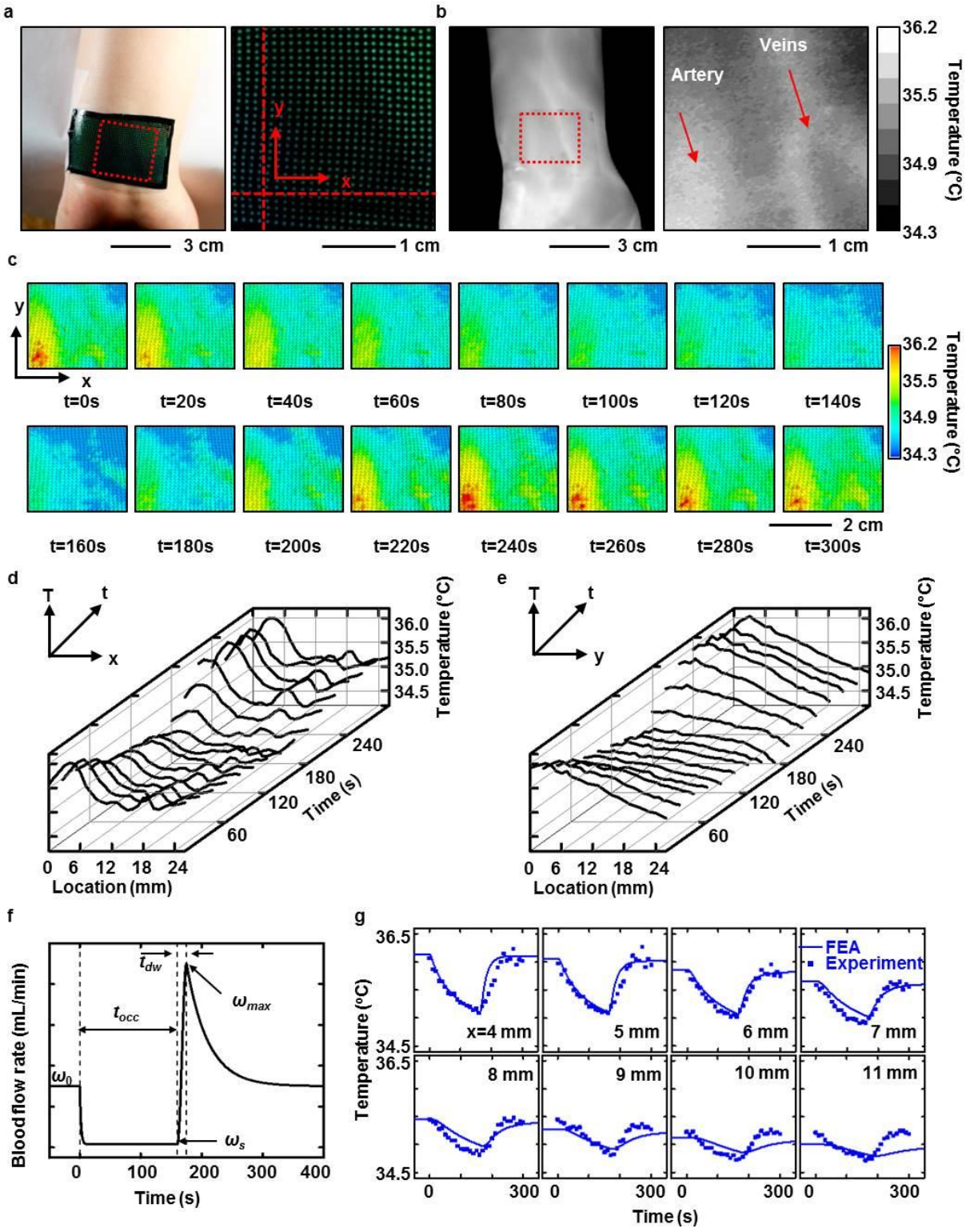

Figure 5.6 Application of an e-TLC thermal imaging device in a reactive hyperaemia test.

(a) Optical images of an e-TLC device on the wrist during an occlusion test after blood is

(Fig. 5.6 continued) released (left) with magnified view (right). (b) Infrared image of the device (left) with magnified view (right). (c) 3D rendering of spatial distributions of temperature determined with the e-TLC device at different times during and after occlusion (occlusion starts at t = 0 s and ends at t = 160 s). (d) Line graphs of temperatures along the horizontal dashed red line in the right frame of a, at various times. (e) Line graphs of temperatures along the vertical dashed red line in the right frame of a, at various times. (f) Rate of blood flow through the ulnar artery determined by comparison of thermal models to experimental results. The key parameters include: the occlusion time (t_{occ}) = 160 s; time-to-peak-flow (t_{dw}) = 15 s; the baseline flow rate (ω_0) = 30 mL/min; the occluded flow rate (ω_s) = 1.5 mL/min; and the peak flow rate (ω_{max}) = 90 mL/min. (g) Measured temperature rise at the surface of the skin above the ulnar artery during the occlusion along with results from finite element analyses (FEA) using the blood flow rate in frame f. The eight sub-frames correspond to the temperature histories of different points at the horizontal dashed red line in the right frame of a.

5.6 References

1. Arumugam, V., Naresh, M. D. & Sanjeevi, R. Effect of strain-rate on the fracture-behavior of skin. *J. Biosciences* **19**, 307-313, (1994).
2. Davis, J. R. *ASM Specialty Handbook: Copper and Copper Alloys*. (ASM International, 2001).

3. William, F. R., Leroy, D. S. & Don, H. M. *Mechanics of Materials*. (Jon Wiley & Sons, 1999)
4. Sandby-Moller, J., Poulsen, T. & Wulf, H. C. Epidermal thickness at different body sites: Relationship to age, gender, pigmentation, blood content, skin type and smoking habits. *Acta Derm.-Venereol.* **83**, 410-413 (2003).
5. Ireland, P. T. & Jones, T. V. The response-time of a surface thermometer employing encapsulated thermochromic liquid-crystals. *J. Phys. E Sci. Instrum.* **20**, 1195-1199 (1987).
6. Kakade, V. U., Lock, G. D., Wilson, M., Owen, J. M. & Mayhew, J. E. Accurate heat transfer measurements using thermochromic liquid crystal. Part 1: Calibration and characteristics of crystals. *Int. J. Heat Fluid Fl.* **30**, 939-949 (2009).
7. Rao, Y. & Zang, S. Calibrations and the measurement uncertainty of wide-band liquid crystal thermography. *Meas. Sci. Technol.* **21** (2010).
8. Stasiek, J., Stasiek, A., Jewartowski, M. & Collins, M. W. Liquid crystal thermography and true-colour digital image processing. *Opt. Laser Technol.* **38**, 243-256 (2006).
9. Anderson, M. R. & Baughn, J. W. Liquid-crystal thermography: Illumination spectral effects. Part 1 - Experiments. *J. Heat Trans.-T. of the Asme* **127**, 581-587 (2005).
10. Farina, D. J., Hacker, J. M., Moffat, R. J. & Eaton, J. K. Illuminant invariant calibration of thermochromic liquid-crystals. *Exp. Therm. Fluid Sci.* **9**, 1-12 (1994).
11. Kodzwa, P. M., Jr. & Eaton, J. K. Angular effects on thermochromic liquid crystal thermography. *Exp. Fluids* **43**, 929-937 (2007).

12. Sabatino, D. R., Praisner, T. J. & Smith, C. R. A high-accuracy calibration technique for thermochromic liquid crystal temperature measurements. *Exp. Fluids* **28**, 497-505 (2000).
13. Cohen, M. L. Measurement of thermal-properties of human-skin - review. *J. Invest. Dermatol.***69**, 333-338 (1977).
14. Xiao, P., Cui, Y., Ciortea, L. I., Berg, E. P. & Imhof, R. E. in *15th International Conference on Photoacoustic and Photothermal Phenomena* Vol. 214 *J. Phys. Conf. Ser.* (eds C. Glorieux & J. Thoen) (2010).
15. Fiala, D., Lomas, K. J. & Stohrer, M. A computer model of human thermoregulation for a wide range of environmental conditions: the passive system. *J. Appl. Physiol.* **87**, 1957-1972 (1999).
16. Gorbach, A. M. *et al.* Infrared imaging of nitric oxide-mediated blood flow in human sickle cell disease. *Microvasc. Res.* **84**, 262-269 (2012).
17. Holowatz, L. A., Thompson-Torgerson, C. S. & Kenney, W. L. The human cutaneous circulation as a model of generalized microvascular function. *J. Appl. Physiol.* **105**, 370-372 (2008).
18. Huang, A. L. *et al.* Predictive value of reactive hyperemia for cardiovascular events in patients with peripheral arterial disease undergoing vascular surgery. *Arterioscl. Throm. Vas.* **27**, 2113-2119 (2007).
19. Ishibashi, Y. *et al.* Short duration of reactive hyperemia in the forearm of subjects with multiple cardiovascular risk factors. *Circ. J.* **70**, 115-123, (2006).
20. Akhtar, M. W., Kleis, S. J., Metcalfe, R. W. & Naghavi, M. Sensitivity of Digital Thermal Monitoring Parameters to Reactive Hyperemia. *J. Biomech. Eng.-T. Asme* **132**, 051005 (2010).

21. Deshpande, C. *Thermal analysis of vascular reactivity*, MS thesis, Texas A&M Univ. (2007).

CHAPTER 6

CONCLUSION AND OUTLOOK

The practical ease and wide availability of the NIL procedures and the liftoff processes, their ability to accommodate both critical feature sizes deep into the nanometer range and macroscale areas, suggest a strong potential for use in both engineering development and exploratory research in fishnet and other emerging classes of metamaterials. On the other hand, the results described with the nTP technique reveal some important effects of film growth in the formation of fishnet NIMs by large area processing techniques. Molecular glass systems make them attractive alternatives to more widely explored inorganics for the dielectric layers. The outcomes enable fabrication of multilayered NIMs with excellent operational characteristics in the visible regime and they appear to have implications in other areas of optical application of methods such as nTP, NIL and others. Epidermal thermochromic liquid crystal devices have enabled precise spatio-temporal temperature mapping through advanced color analysis. All the data acquisition and analysis can be potentially completed with a smartphone device and allow much cheaper, faster, more portable and accessible devices that are available for patients. Last but not the least, ultra-stretchable plasmonic nanoparticle array is observed to have great tuning capability induced by stretch, its non-linear buckling behavior has revealed the fundamental mechanics associated with the nanoscale, non-continuous array structures. We can use the mechanical and optical modeling tools to design advanced nanoparticle array geometry, where unusual three dimensional architecture can be formed by strain introduction. Such uncommon structures could provide extraordinary optical resonance features and tuning capability that other techniques could not possibly achieve. The wide-band tuning characteristics in this system can

also be utilized in tunable aluminum color pixels which can be applied in advanced display technology. Future device thickness reduction and mechanics modification can also make the plasmonics conformal to the human skin, and be used as strain sensors that detect strain change and surface morphology on epidermis by optical resonances signals. Wearable chemical and biosensors that rely on plasmonics signals can also be possible.

APPENDIX

SUPPLEMENTARY FIGURES

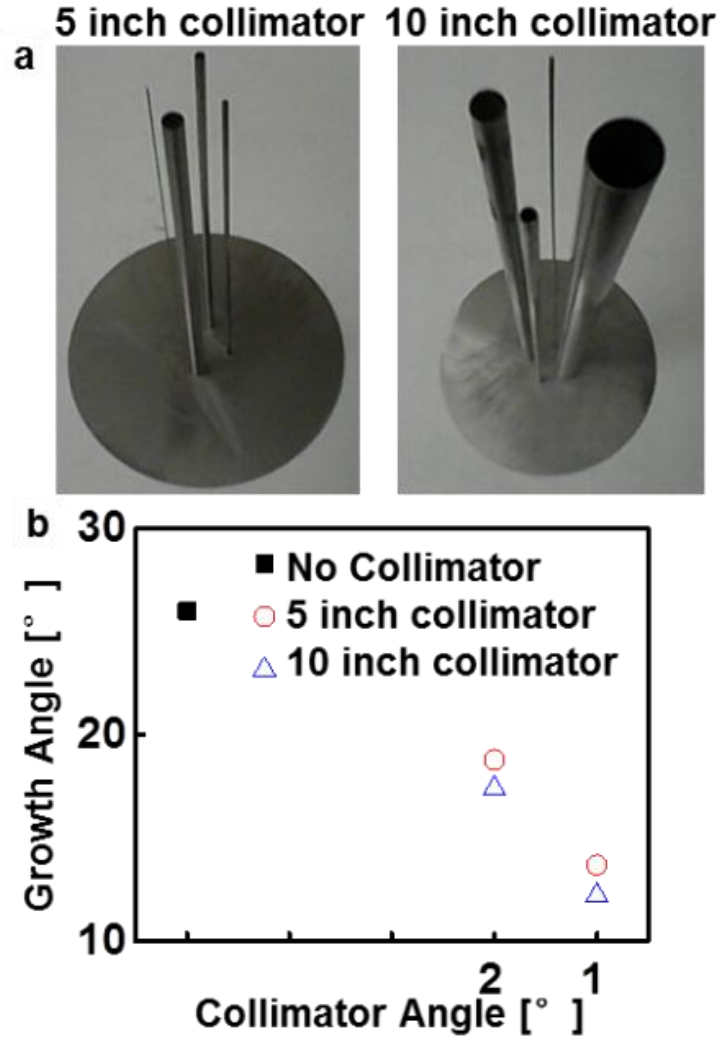

Figure S1. (a) Images of electron-beam collimator tubes and (b) experimental result of different growth angles obtained from collimator tubes in physical vapor deposition.

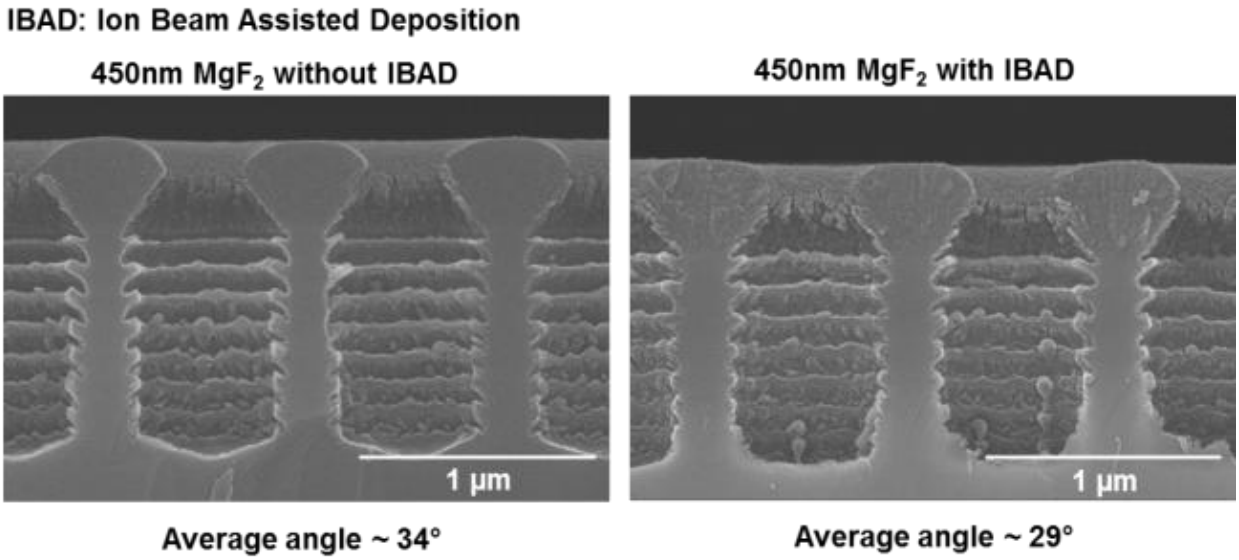

Figure S2. Electron-beam depositon of single layer MgF2 with and without ion beam.

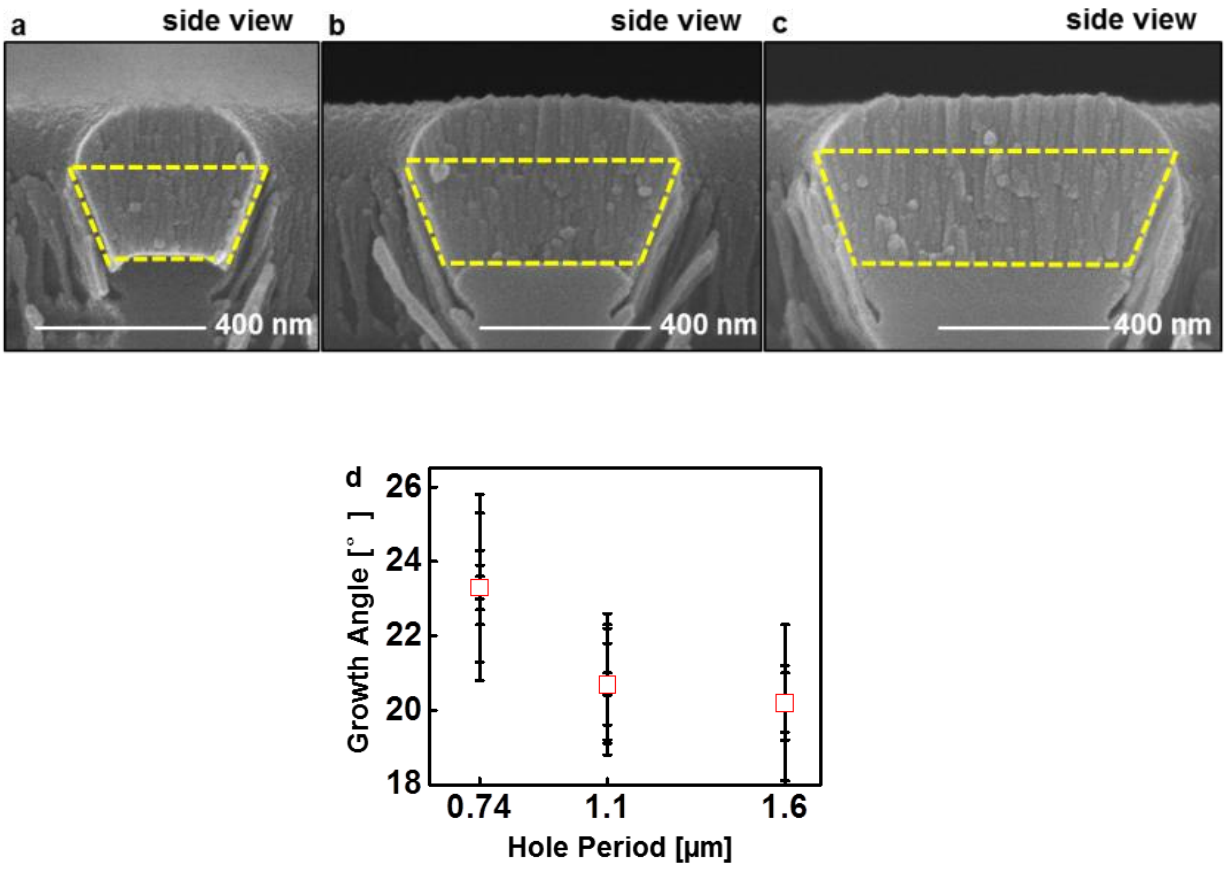

Figure S3. Growth angle dependence on different fishnet hole periods. 350nm MgF2 deposition on (a) period=0.74μm, (b) period=1.1 μm, (c) period=1.6 μm and (d) shows growth angles calculated for different fishnet hole periods.

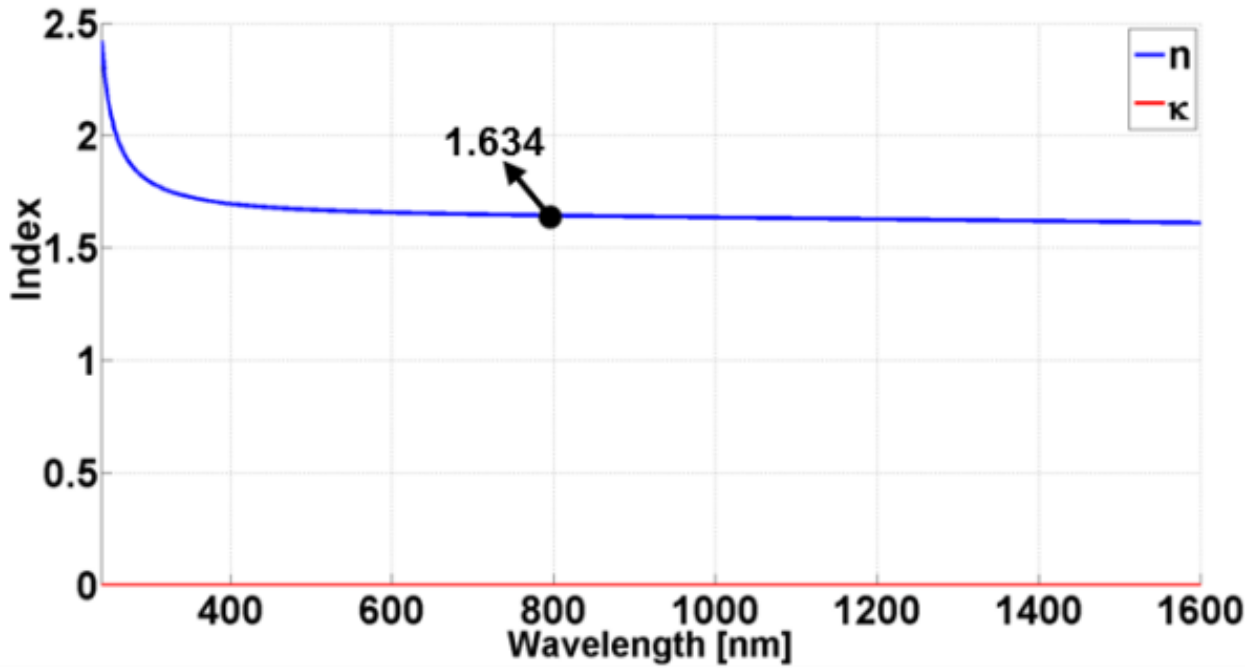

Figure S4. Experimentally measured refractive indices (n, κ) values of MG (alpha, alpha, alpha'-tris(4-hydroxyphenyl)-1-ethyl-4-isopropylbenzene).

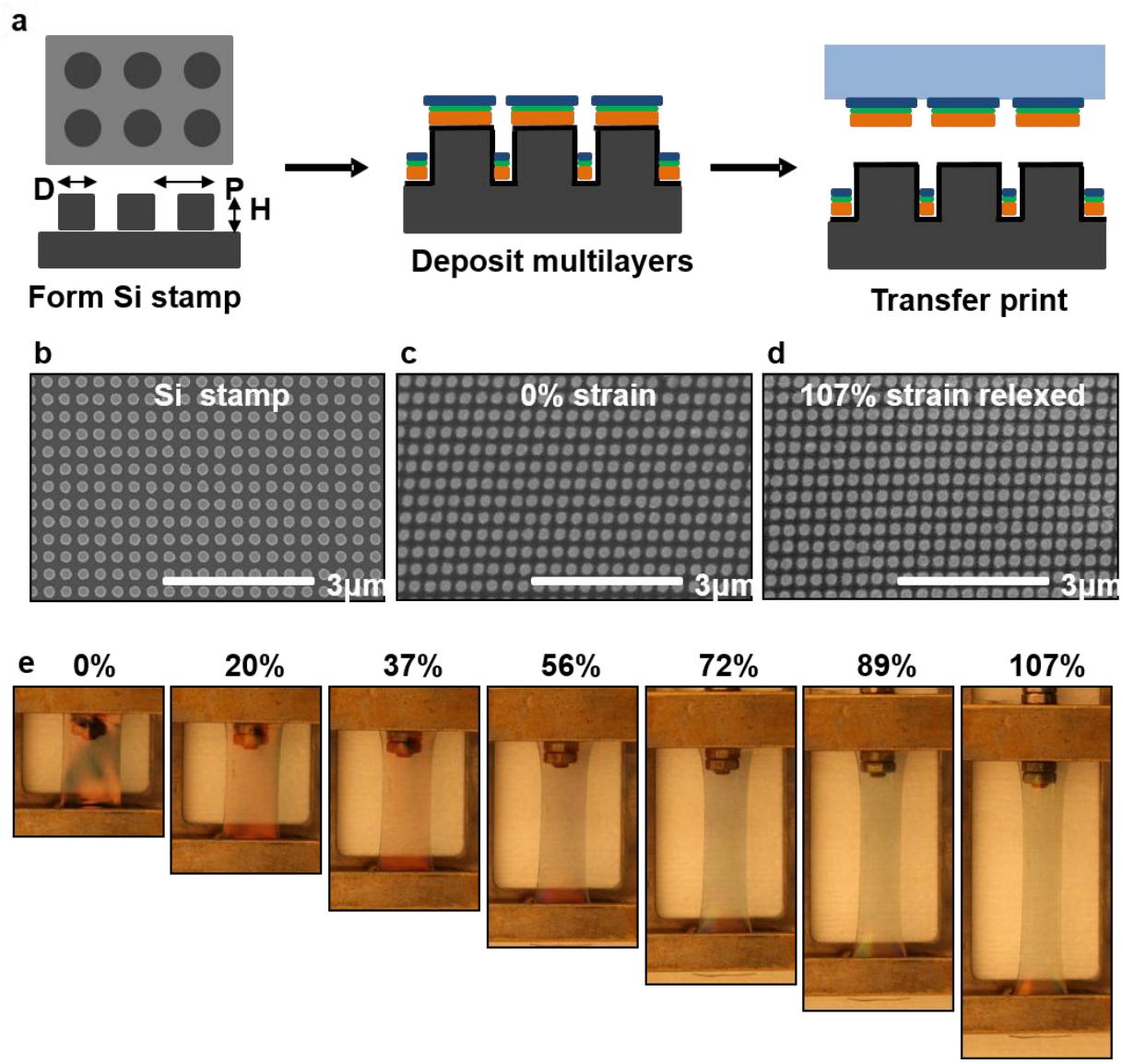

Figure S5 Device fabrication and stretching experiments. (a) Schematics of the major fabrication steps. (b) Top down SEM of the silicon stamp. (c) Top down SEM of Au nanodot array transferred to PDMS substrate. (d) Top down SEM of Au nanodot array released from 107% strain. (e) Stretching experiment of a device placed on a metal stretcher

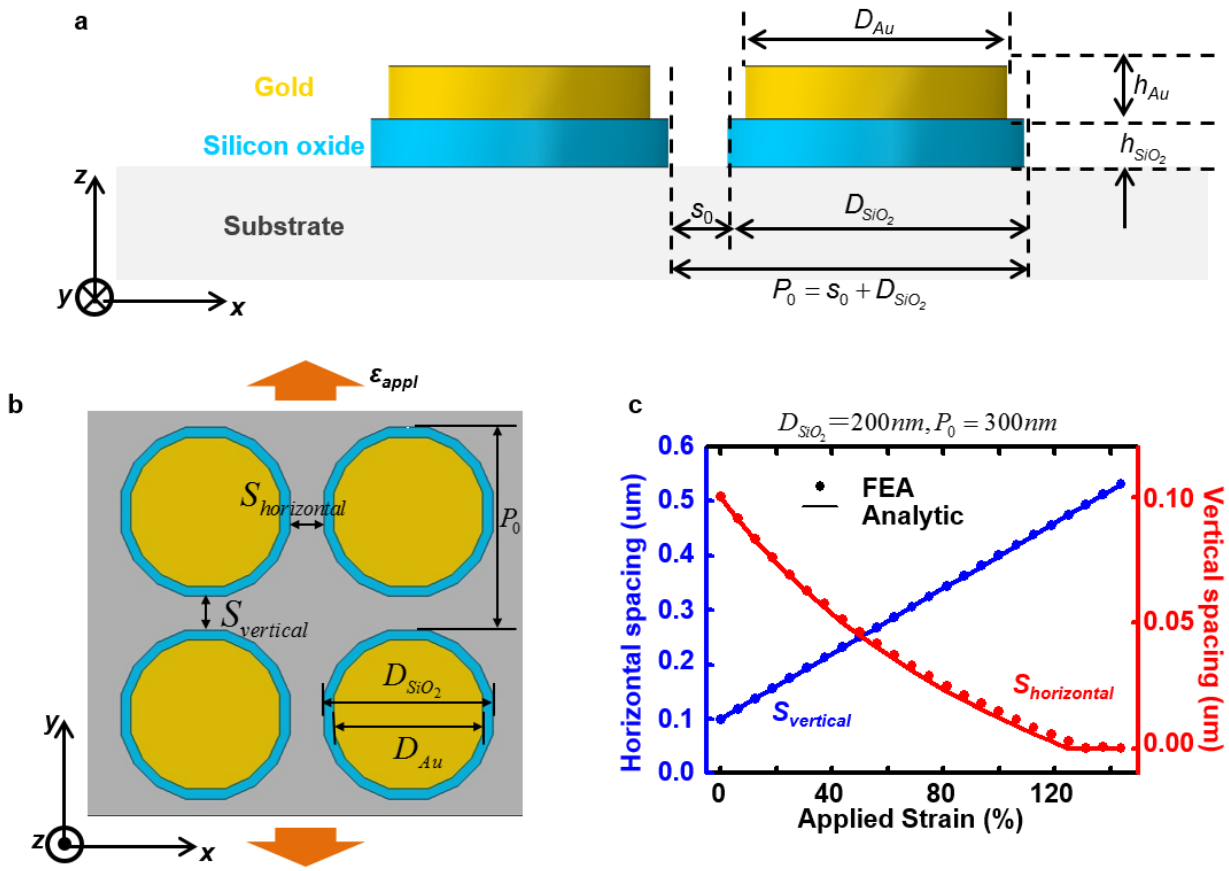

Figure S6 FEA and analytical models for the nanodot array geometry change under uniaxial strain. (a) Cross sectional view of the parameters used in the models. (b)) Top down view of the parameters used in the models.. (c) FEA and analytical results of the horizontal and vertical spacing change under different strains for the case of P=300nm, D=200nm.

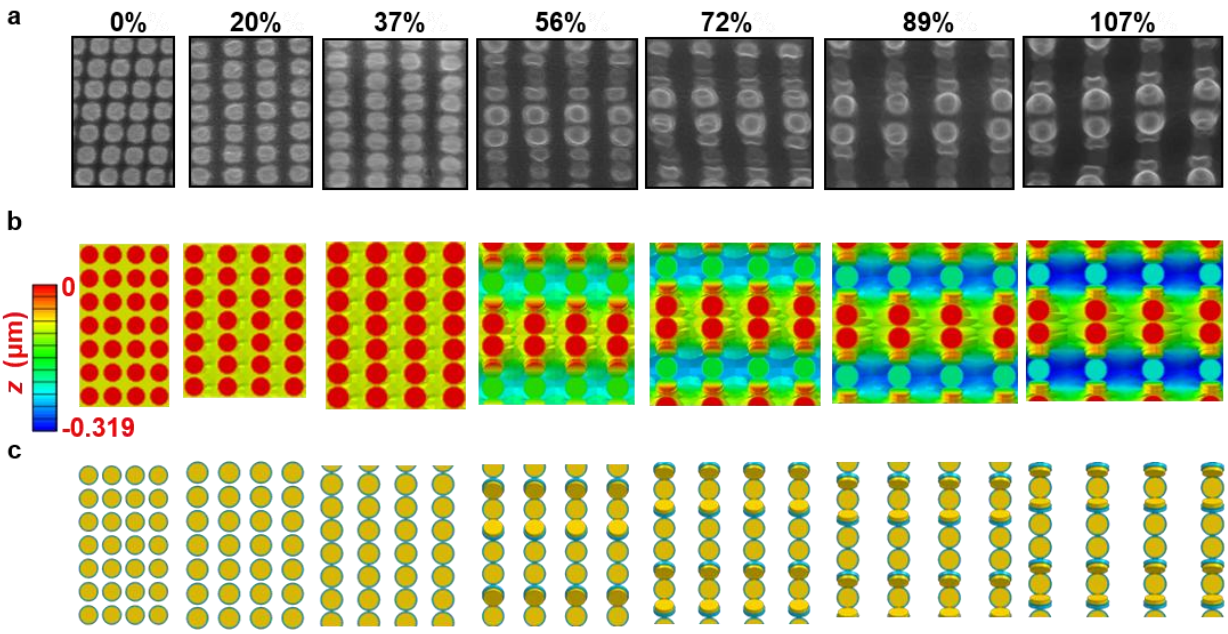

Figure S7 Comparison of the Top Down SEM images and mechanical model results under different strains. (a) Au nanodot array (P=300nm, D=220nm) on PDMS substrate under seven strains applied in the y direction. (b) FEA results of the Au nanodot array deformation under seven strains, the color bar represent height change. (c) Semi- analytical results of the Au nanodot array deformation under seven strains.

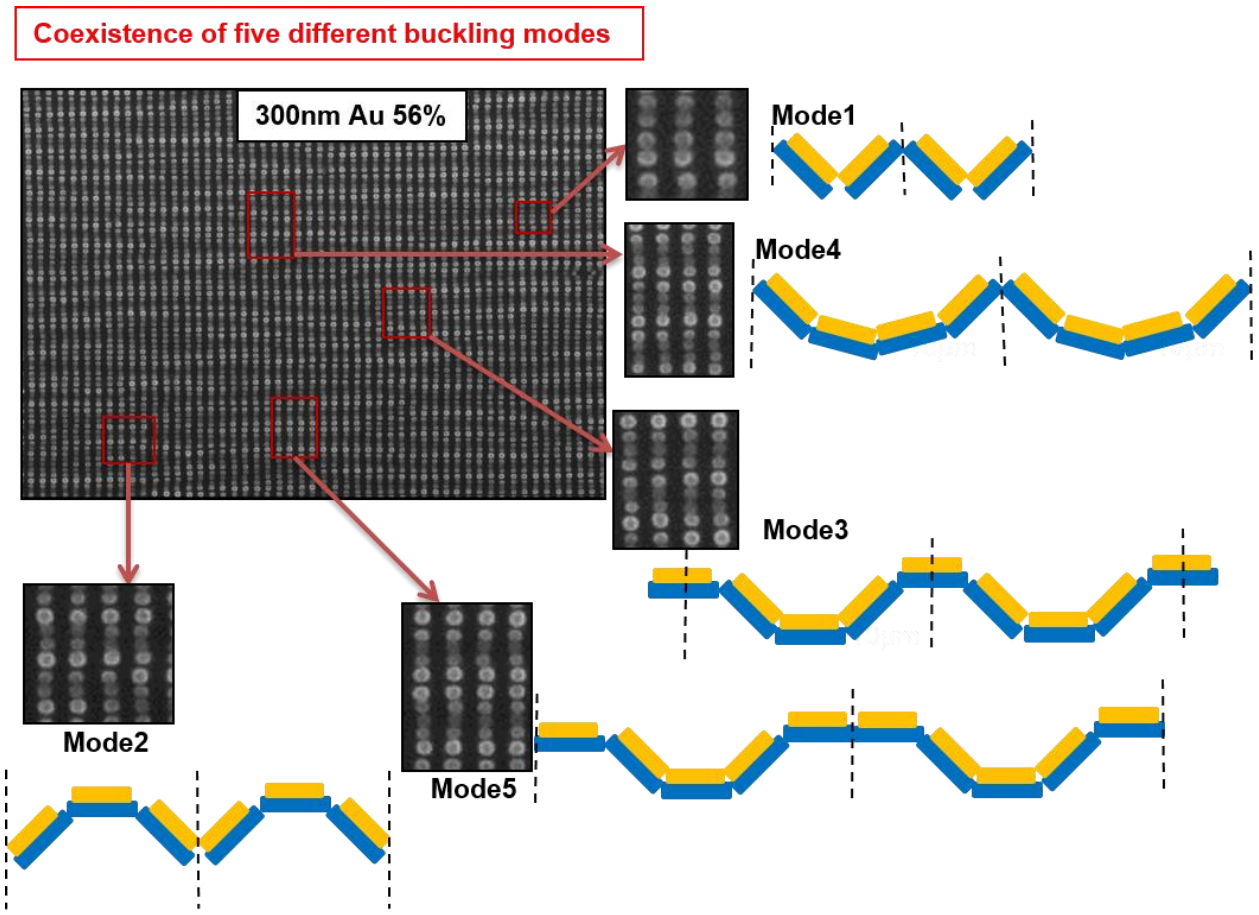

Figure S8 Coexistence of five different buckling modes under 56% strain with the cross sectional schematic views.

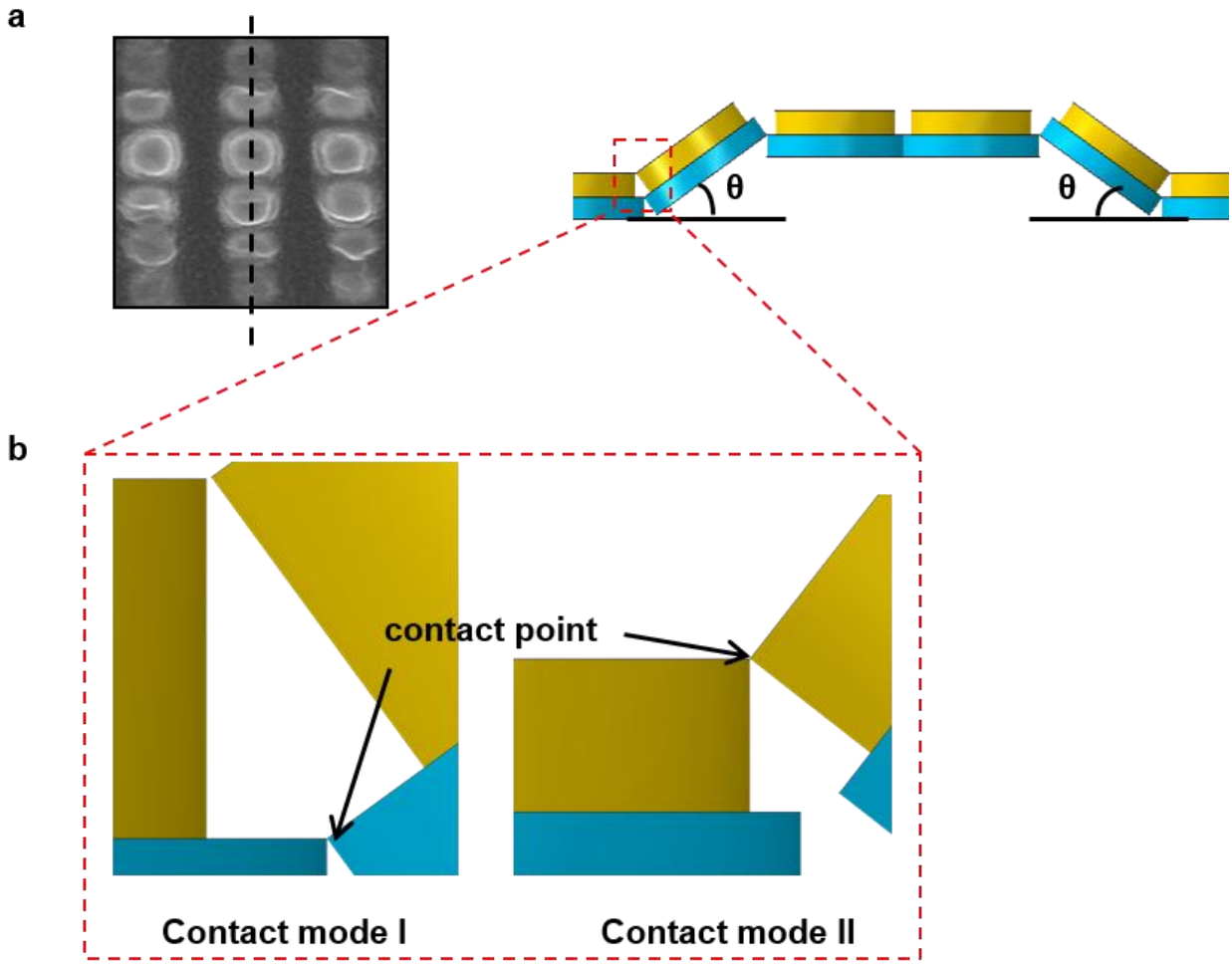

Figure S9 Example of one buckling mode. (a) The most typical buckling mode that has five nanodots in a wavelength, with the rotation angle θ as a variable. (b) Two different contact modes that can be found in the buckling mode.

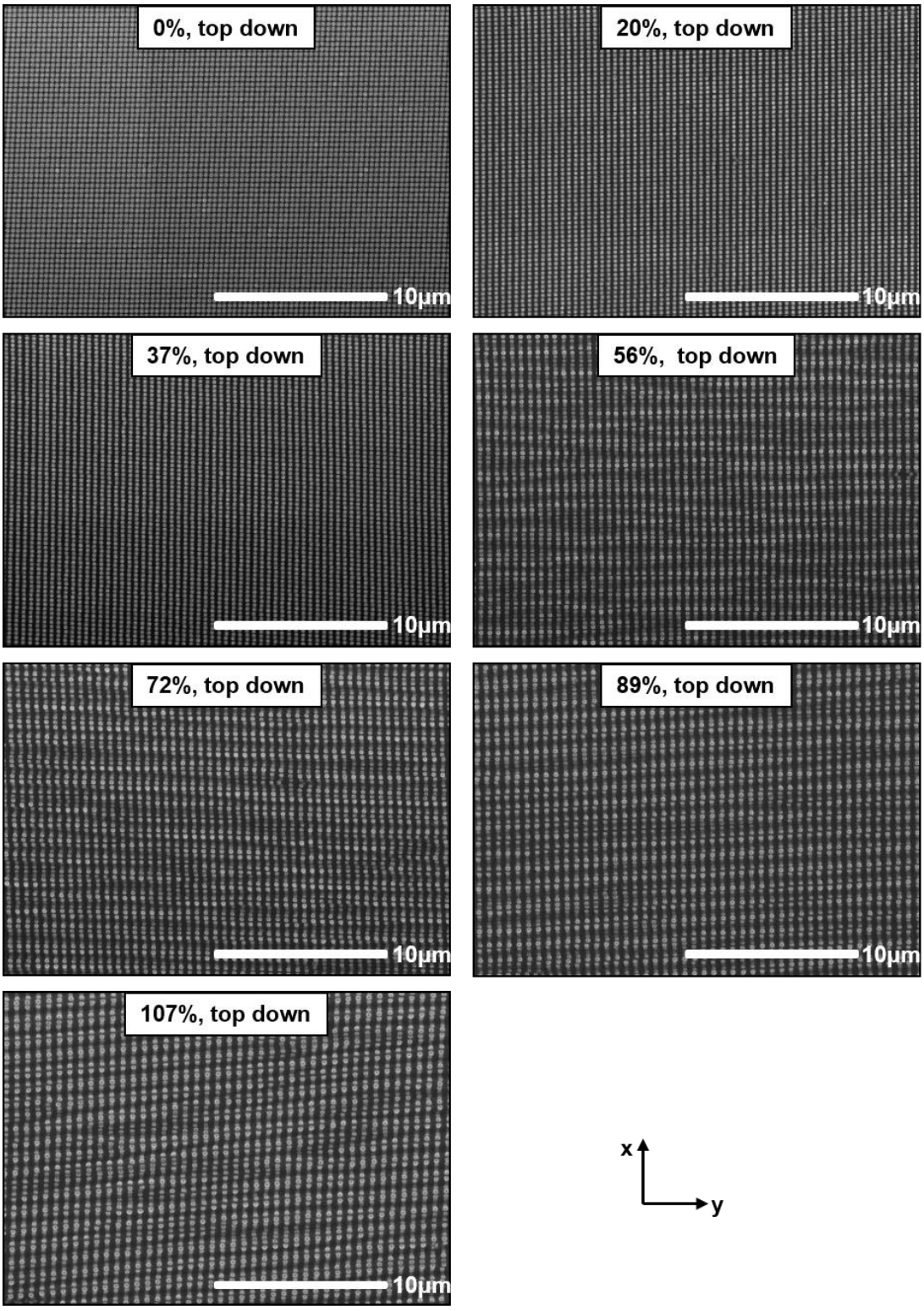

Figure S10 Comparison of the top down SEM images and geometry deformation under different strains applied in the y direction.

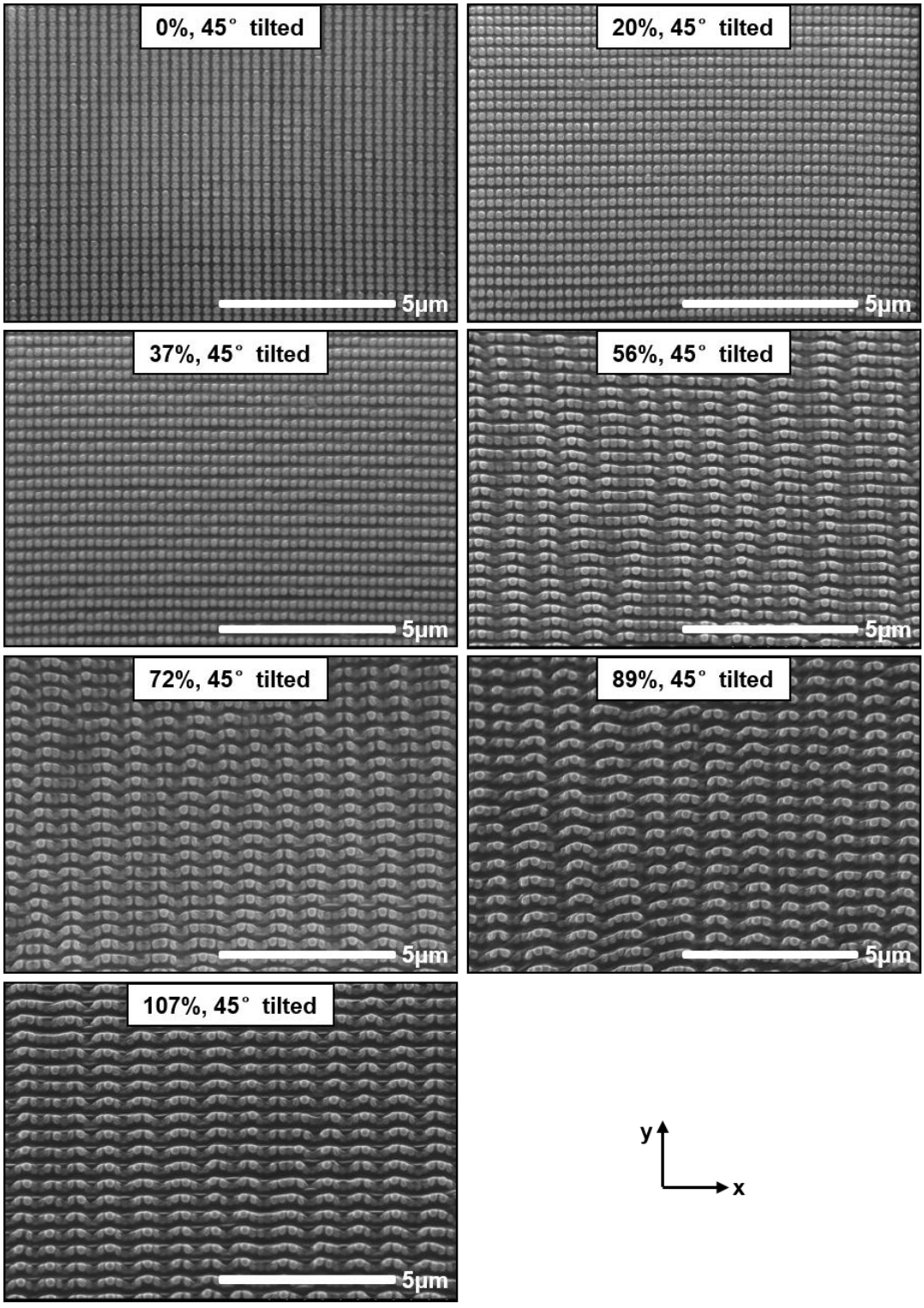

Figure S11 Comparison of the 45°tiltedSEM images and geometry deformation under different strains applied in the y direction.

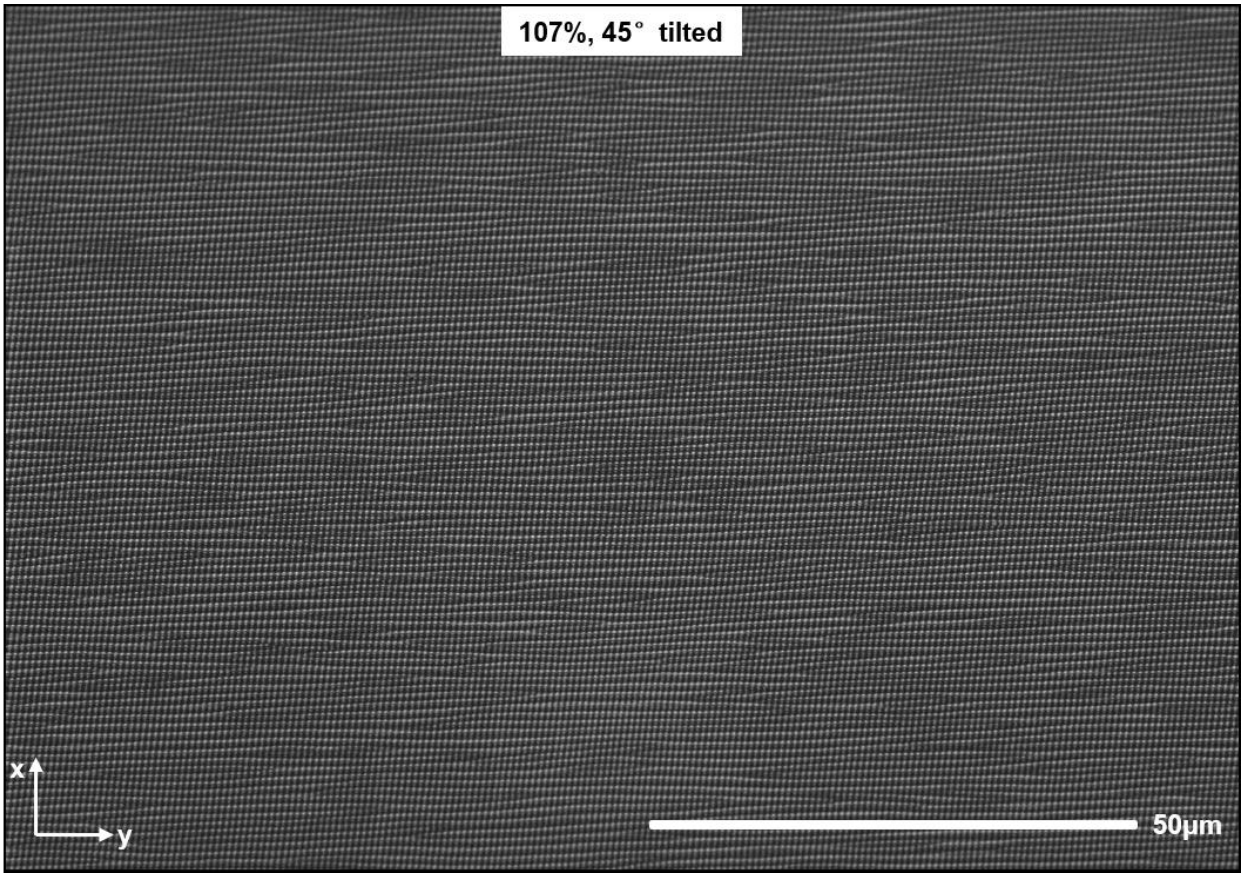

Figure S12 SEM image of the buckled waves under 107% strain with area size over 10^4 μm^2.

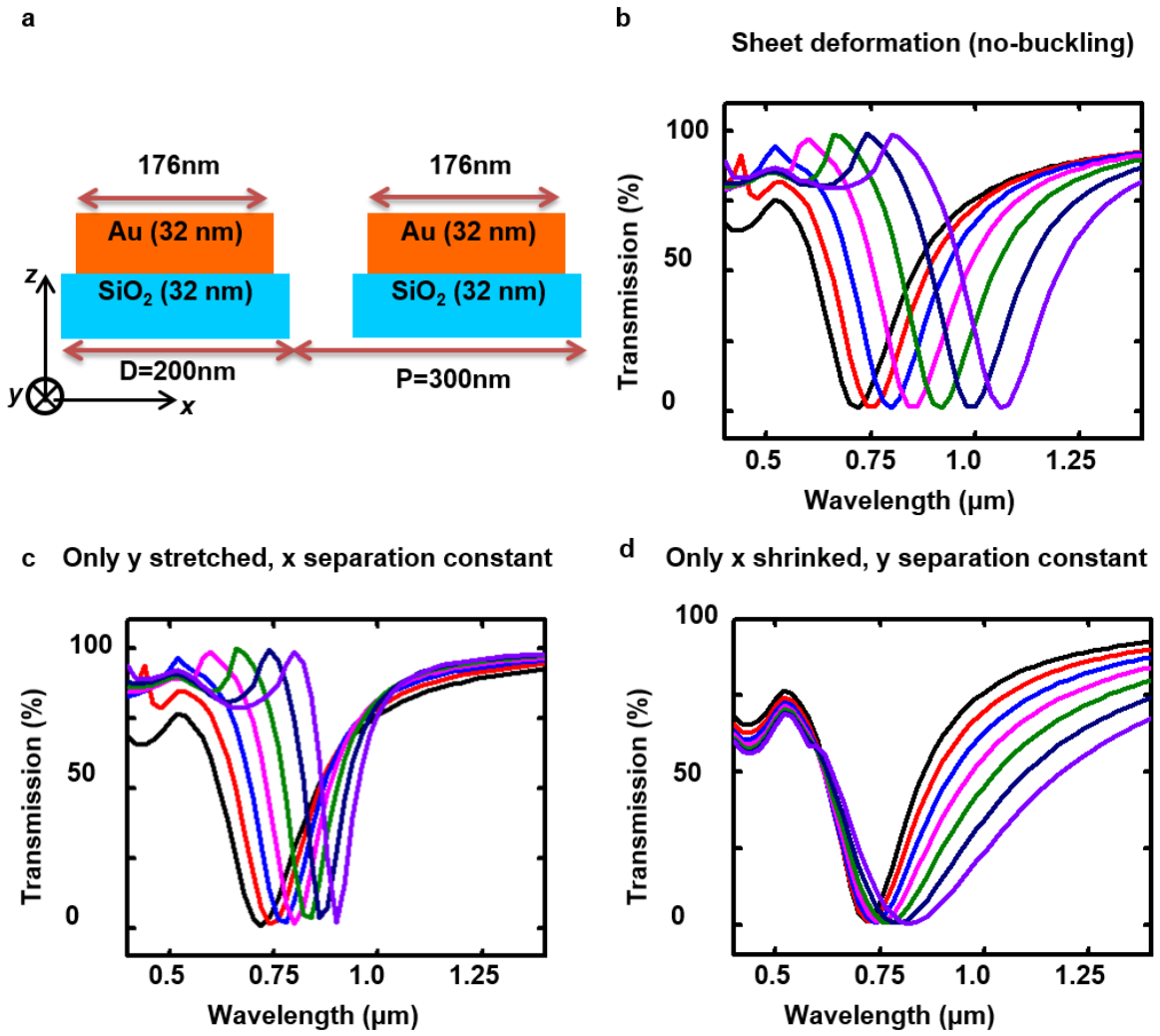

Figure S13 FEM optical simulation for the linear nanodot array geometry change under uniaxial strain. (a) The nanodot geometry parameter used in simulation which is slightly smaller than those in experiement. (b) Simulated spectra shows red shifts when nanodot array widen in y direction and narrow in x direction. (c)) Simulated spectra shows red shifts when nanodot array widen in y direction and kept constant in x direction. (b) Simulated spectra shows red shifts when nanodot array kept constant in y direction and narrow in x direction.

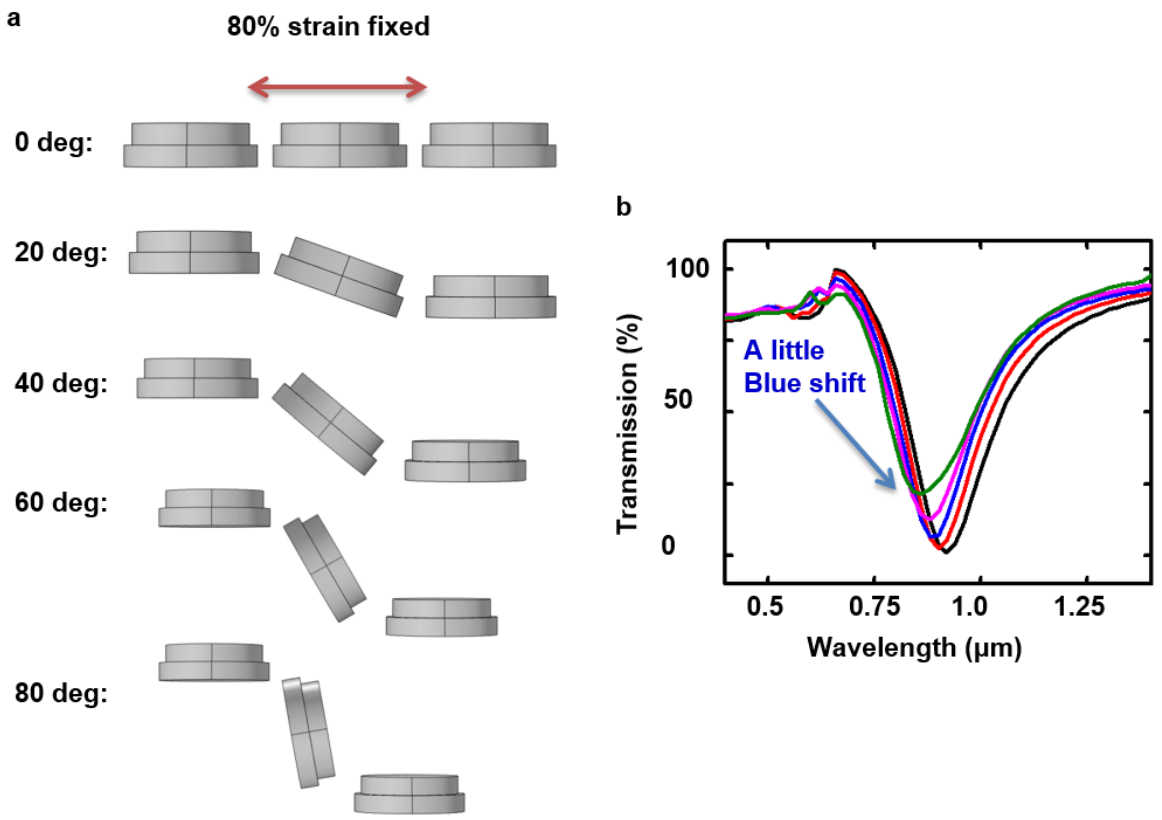

Figure S14 FEM optical simulation for the buckled nanodot array geometry change under uniaxial strain. (a) The model assumption used in simulation with strain fixed at 80% and different rotation angles. (b)) Simulated spectra shows blue shifts at bigger rotation angles.

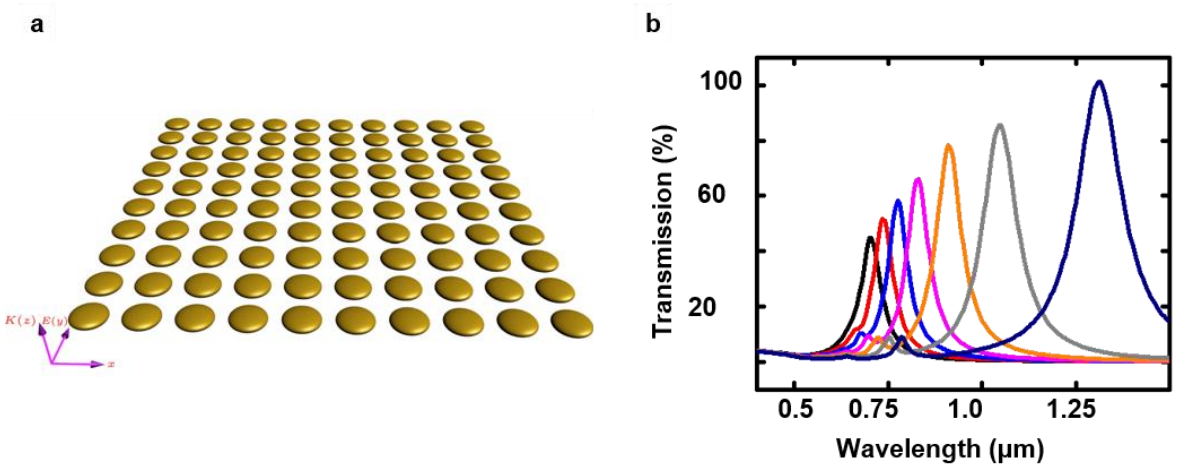

Figure S15 Coupling-dipole approximation method for the linear nanodot array geometry change under uniaxial strain. (a) The model assumption used in simulation.(b) Simulated spectra shows red shifts with increasing strains.

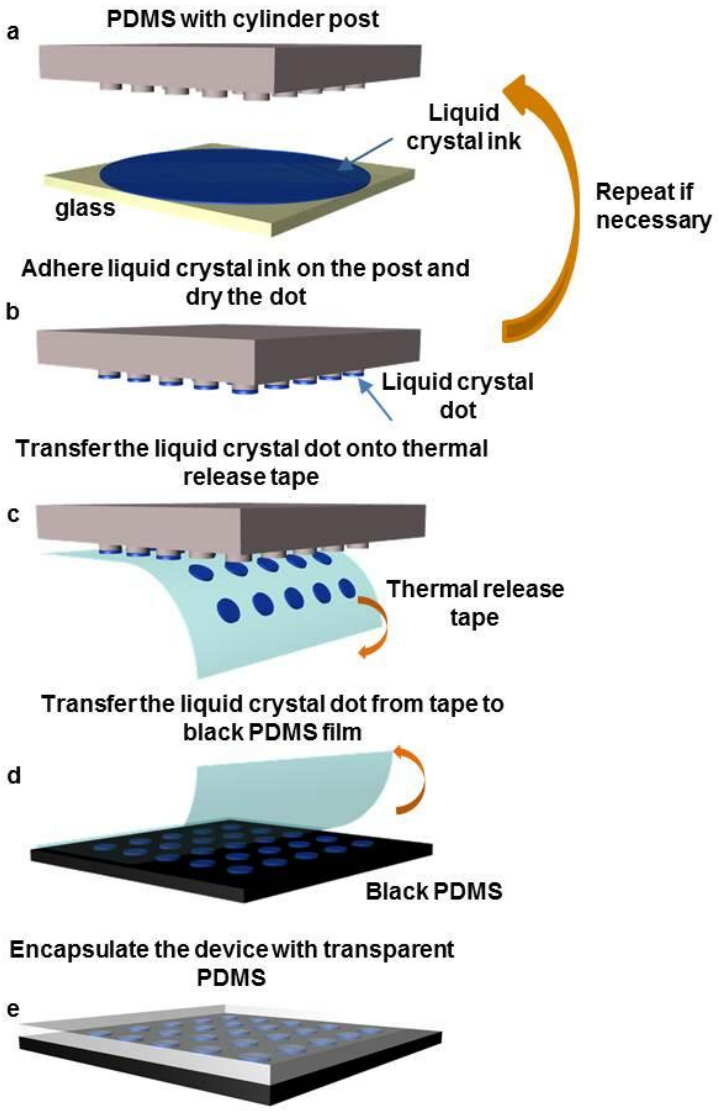

Figure S16: Process for fabricating e-TLC devices. (a) A PDMS stamp with an array of posts embossed on its surface is 'inked' by bringing it into contact with a uniform layer of TLC aqueous slurry spin cast on a glass slide while still in wet state. The thickness of the ink was ~100 μm to ensure that the ink contacts on the top surfaces of the posts. (b) The inked TLC material on the PDMS stamp was allowed to dry in air for 15 minutes. The thickness of the dried film is ~15 μm. Additional 'inking' processes are repeated to achieve a final thickness of 25-30μm. A typical TLC pixel is thickest in the center due to the hydrophobic nature of the PDMS

(Fig. S16 continued) surface and the large contact angle formed during the inking process. (c) Transfer printing allows delivery of the TLC to a piece of thermal release tape. (d) Transfer to the black PDMS substrate is enabled by heat activated release from the tape. (e) The device is encapsulated with a transparent layer of PDMS by spin casting.

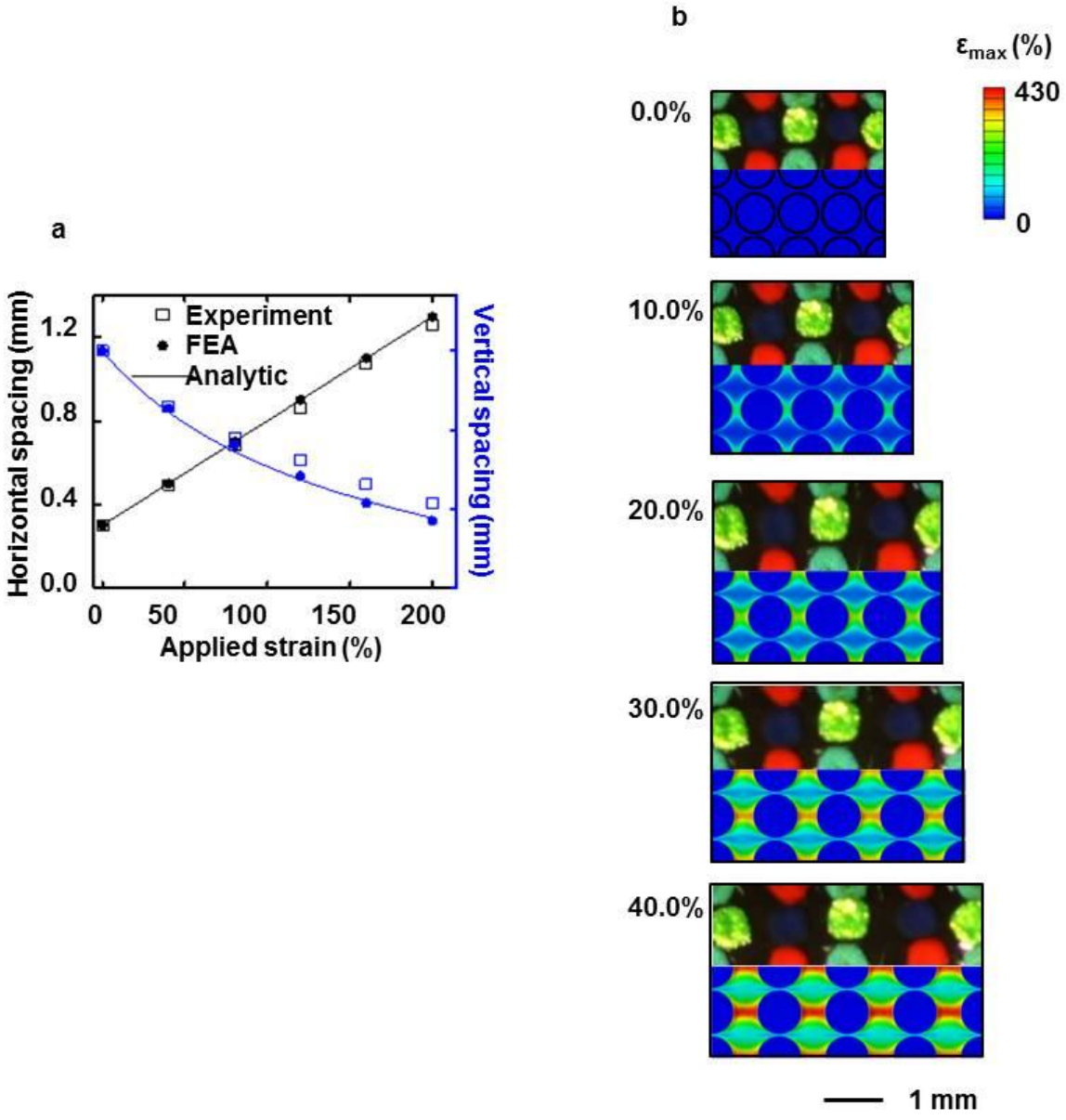

Figure S17: Mechanical response of an e-TLC device to uniaxial strain. (a) Experimental, analytical and finite element modeling results for the change in horizontal and vertical spacing

(Fig. S17 continued) between adjacent pixels under different levels of tensile strain. (b) Comparison between images and three dimensional finite element modeling of a representative region of an e-TLC device that incorporates color calibration pixels under different levels of tensile strain.

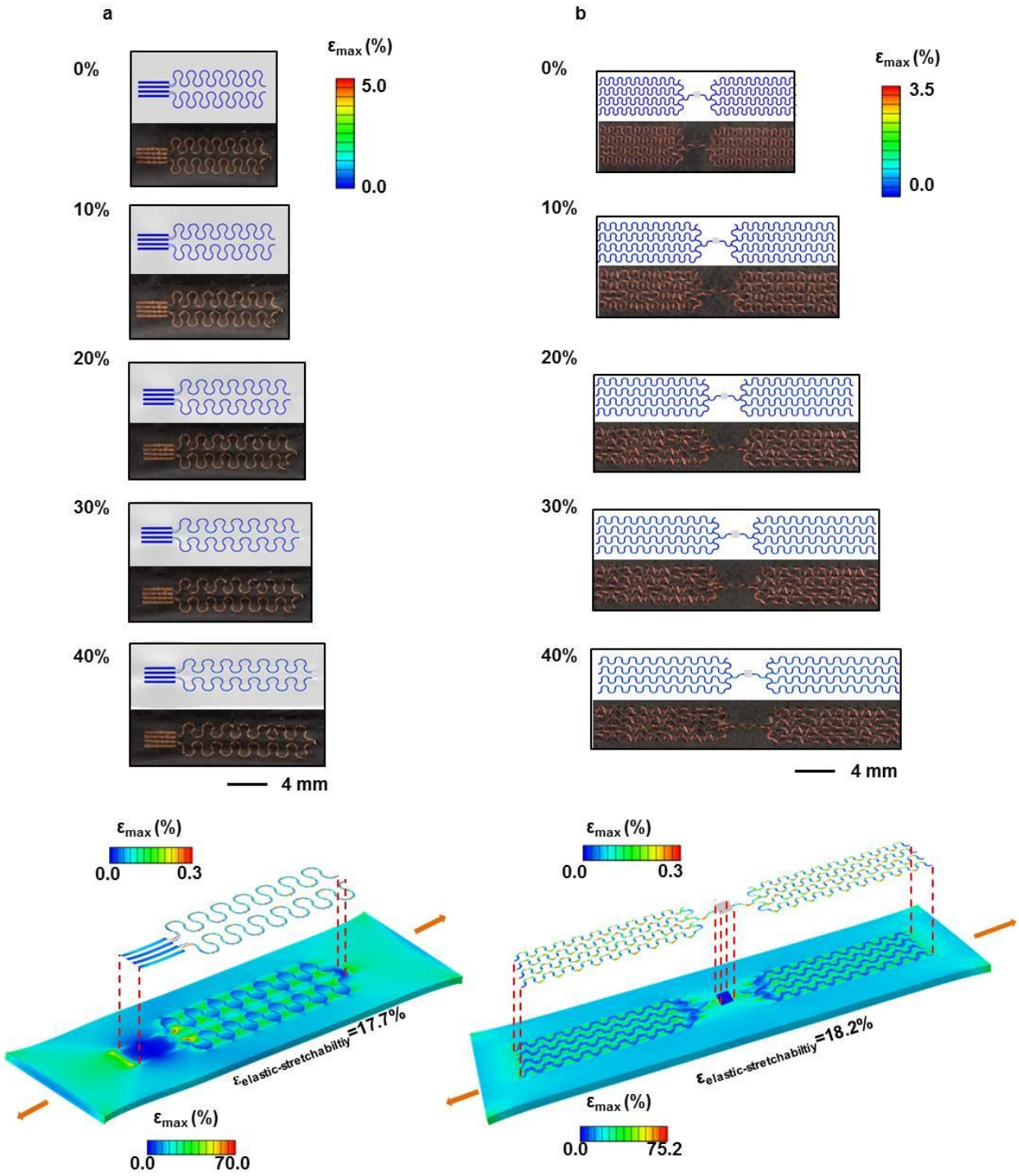

Figure S18: Experimental and computational studies of the mechanical properties of Joule heater element. (a) Comparison between experimental images and three dimensional finite element modeling of a wired Joule heating element under different levels of tensile strain, and

(Fig. S18 continued) strain distribution computed for the case of stretching to 50%. (b) Comparison between experimental images and three dimensional finite element modeling of a wireless Joule heater under different levels of tensile strain, and strain distribution computed for the case of stretching to 50%.

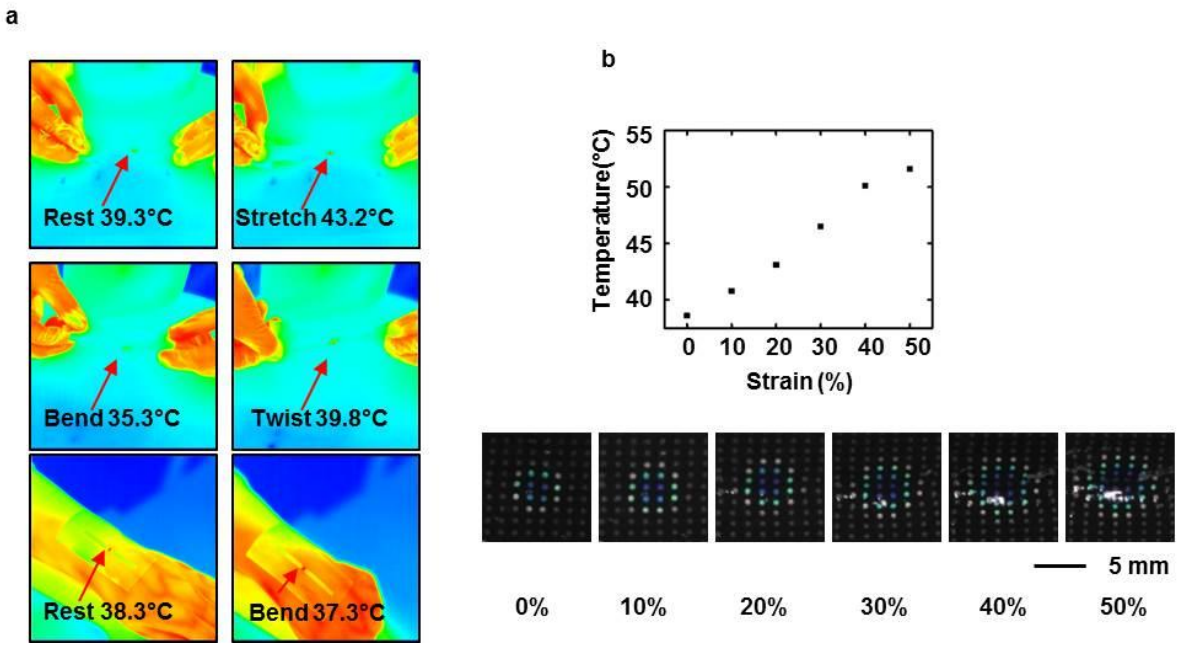

Figure S19: Experimental studies of the effect of strain on the efficiency of wireless Joule heating. (a) Infrared temperature measurements for a wireless Joule heater under exposure to RF energy while mechanically deformed in different ways, both in air and on skin. (b) Measurements at different levels of tensile strain with corresponding images.

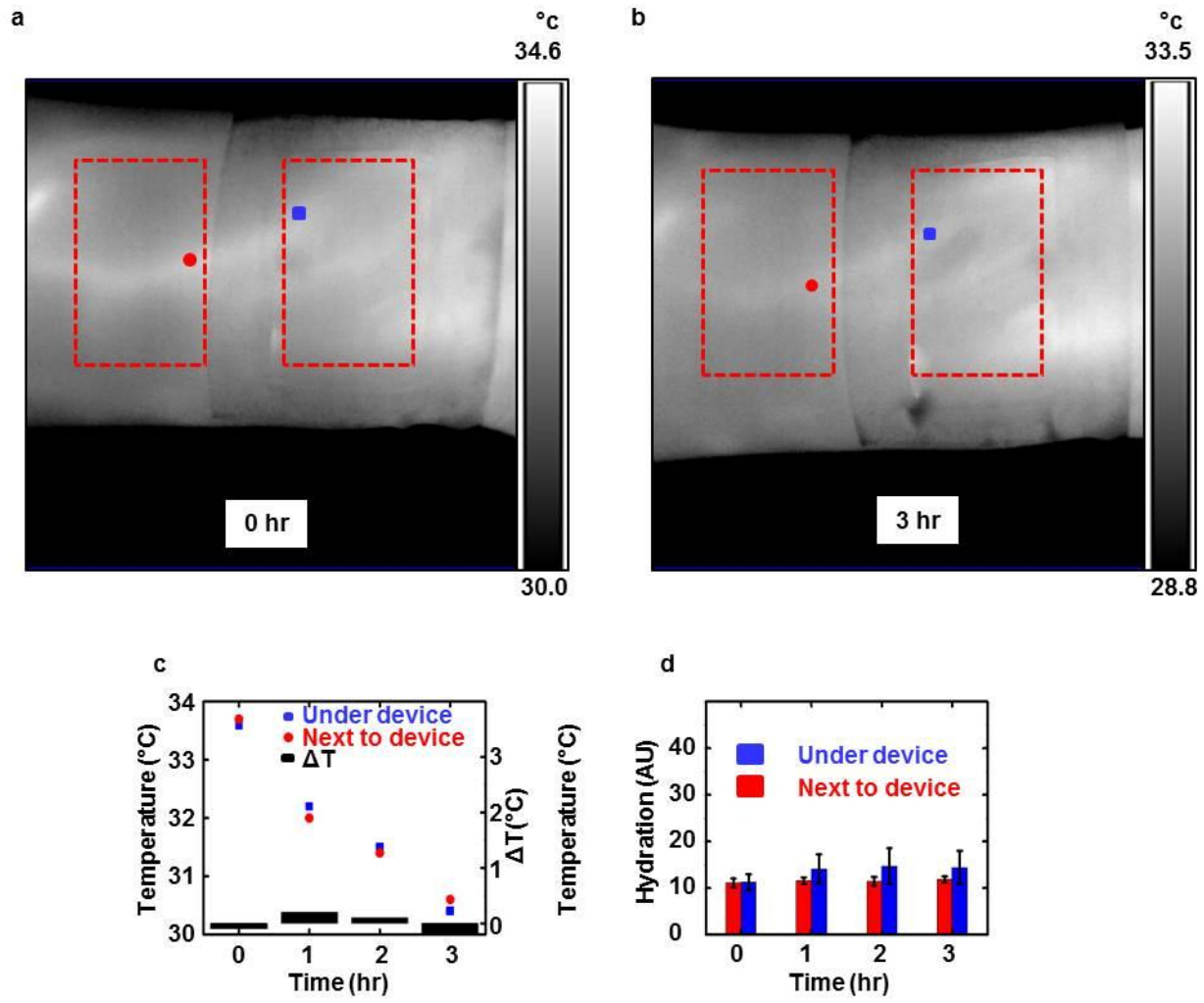

Figure S20: Effect of e-TLC operation on temperature and hydration of the skin. (a) Infrared image captured immediately after mounting an e-TLC device on the wrist. (b) Infrared image captured 3 hours after mounting. For both (a) and (b), the data indicate that the average temperatures at the regions of the device are the same as those adjacent to the device. (c) Temperature difference between a point near the device and a point underneath the device shows no obvious increase during the three hour operation. (d) Hydration level read from a commercial hydration meter shows a maximum increase of about 25% after 3 hours operation on a very dry skin.

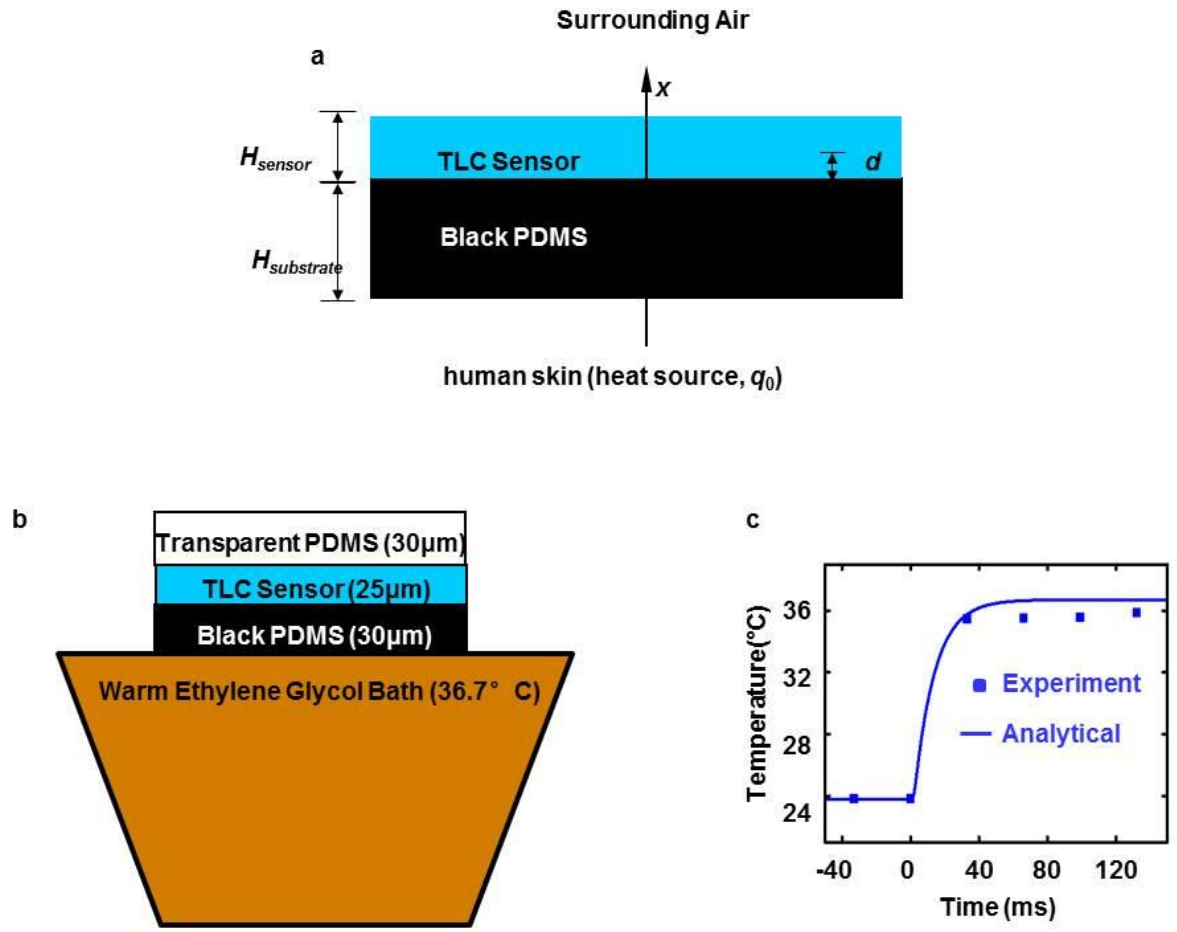

Figure S21: Sensor response time. (a) Layers used in analytical modeling to determine sensor response time on skin. (b) Experimental setup for measuring sensor response time. A warm ethylene glycol bath, which has similar thermal properties to skin, is in contact with the e-TLC device from the back surface. (c) Experimental sensor response time captured by high speed camera, and corresponding analytic predictions based on a one-dimensional heat conduction model. In experiment, the time required for the sensor to reach 90% of the total temperature change is achieved in one frame which is approximate 33 ms for the case of 30μm black PDMS and 25μm liquid crystal.

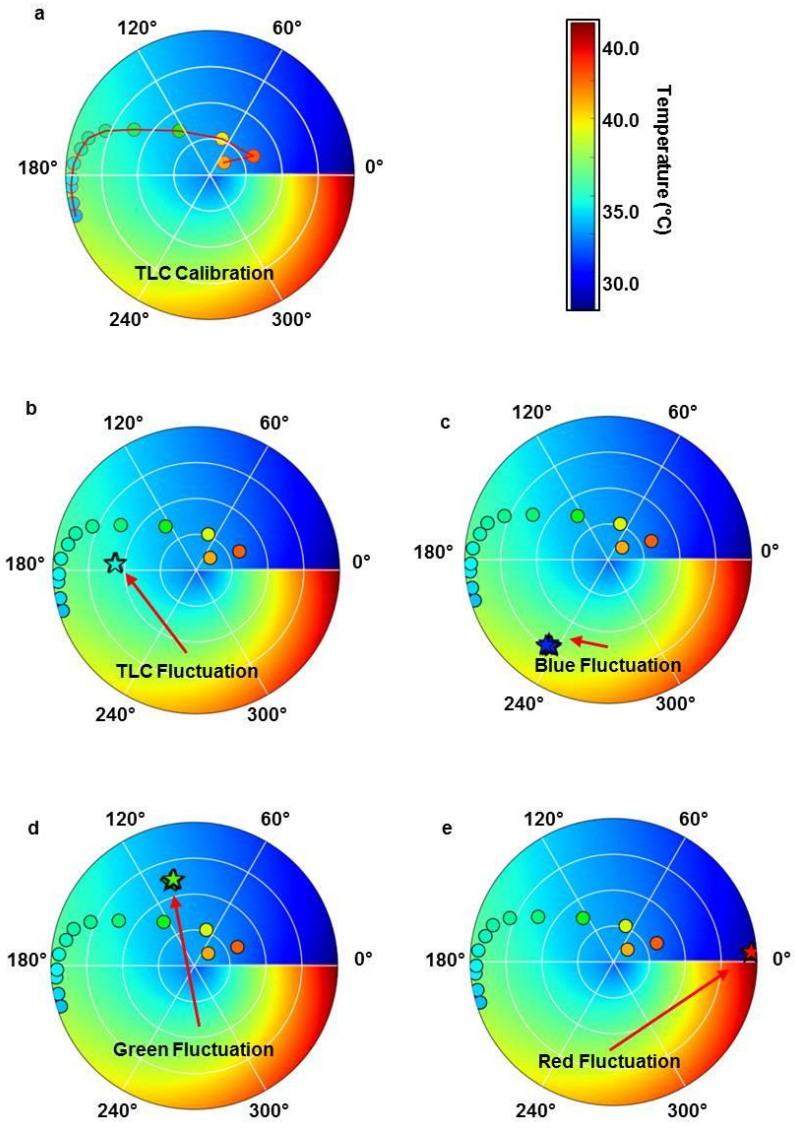

Figure S22: Noise and uncertainty examined using temperature insensitive acrylic colors. (a) TLC color-temperature calibration plotted in the hue/saturation space. Dots are at the positions of corresponding to hue/saturation values of TLC during calibration run and painted with their hue values. Temperatures are calculated with two dimensional linear fit and represented by color gradient. (b) Temporal TLC color fluctuation at fixed temperature. (c) Temporal blue solid color dot fluctuation at fixed temperature. (d) Temporal green solid color dot fluctuation at fixed temperature. (e) Temporal red solid color dot fluctuation at fixed temperature.

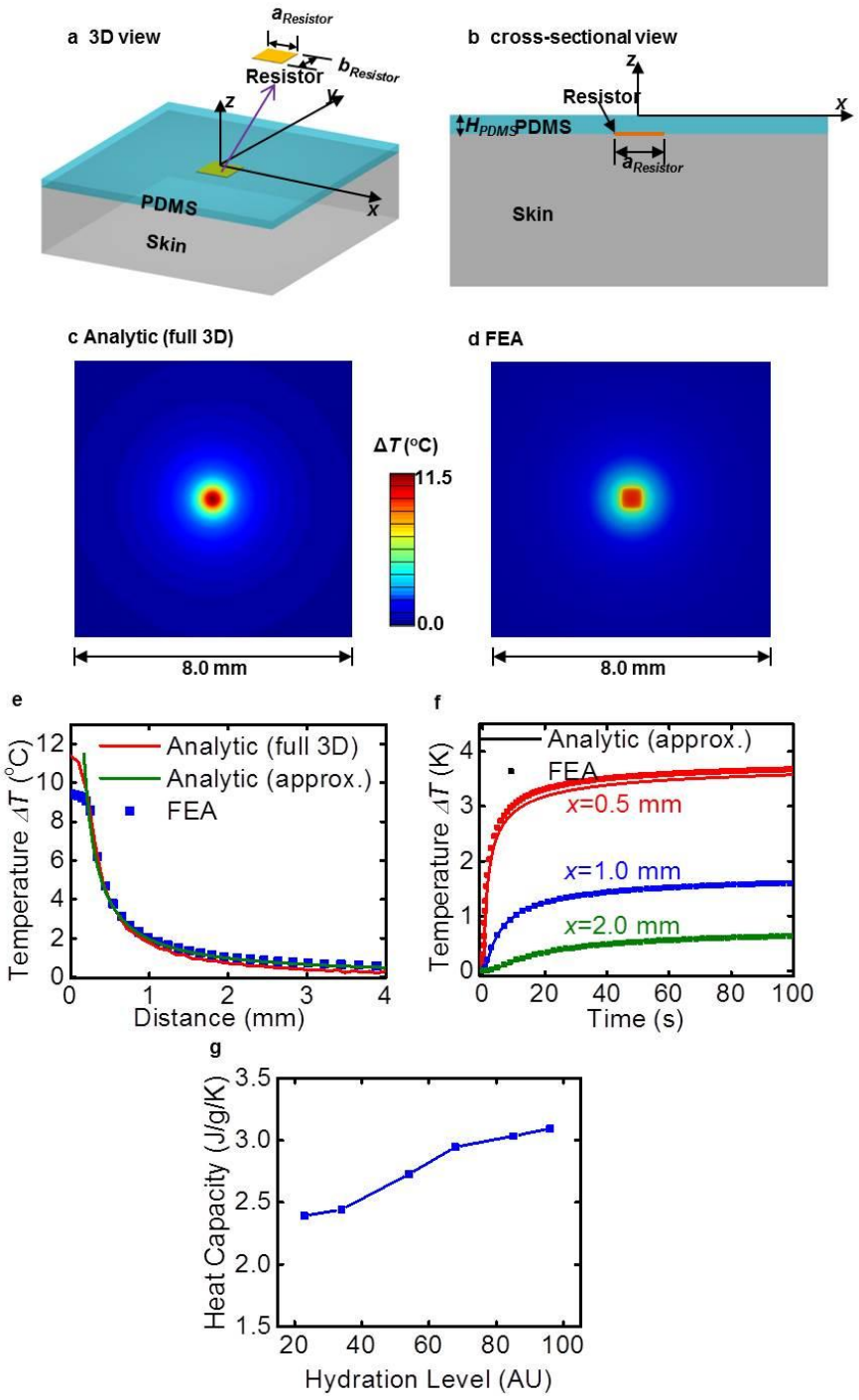

Figure S23: Finite element models that allow determination thermal conductivity and diffusivity from data collected using active e-TLC devices. (a) A 3D view of a model with a Joule heater embedded between an e-TLC device and the skin. (b) A cross-sectional view of a

(Fig. S23 continued) model with a Joule heater embedded between an e-TLC device and the skin. (c) Analytical model of the spatial decay in temperature at steady state during operation of the Joule heater. (d) Corresponding finite element modeling results. (e) Analytical and finite element model of the spatial temperature decay with a wired Joule heater operation along one dimension. (f) Analytical and finite element model of the temporal temperature rise with a wireless Joule heater operation for locations away from the heater. (g) Skin heat capacity inferred from the skin thermal conductivity and diffusivity values in Figure 14.

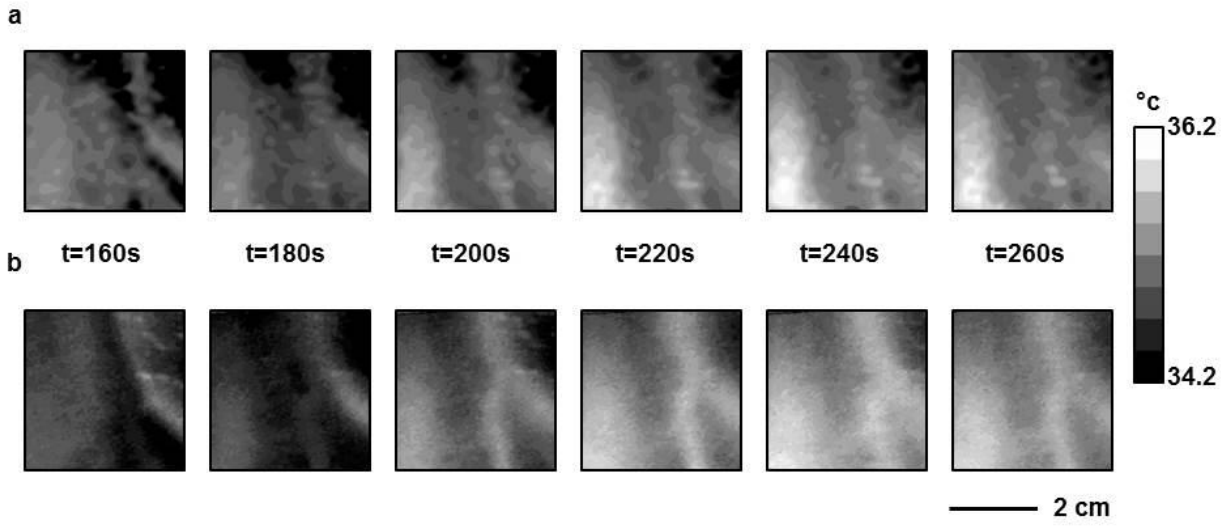

Figure S24: Comparison of an e-TLC thermal imaging device and infrared camera measurement in a reactive hyperaemia test. (a) Spatial distributions of temperature determined with the e-TLC device at representative times from t=160s to t=260s at an interval of 20s. (b) Spatial distributions of temperature determined with the infrared camera at representative times from t=160s to t=260s at an interval of 20s.

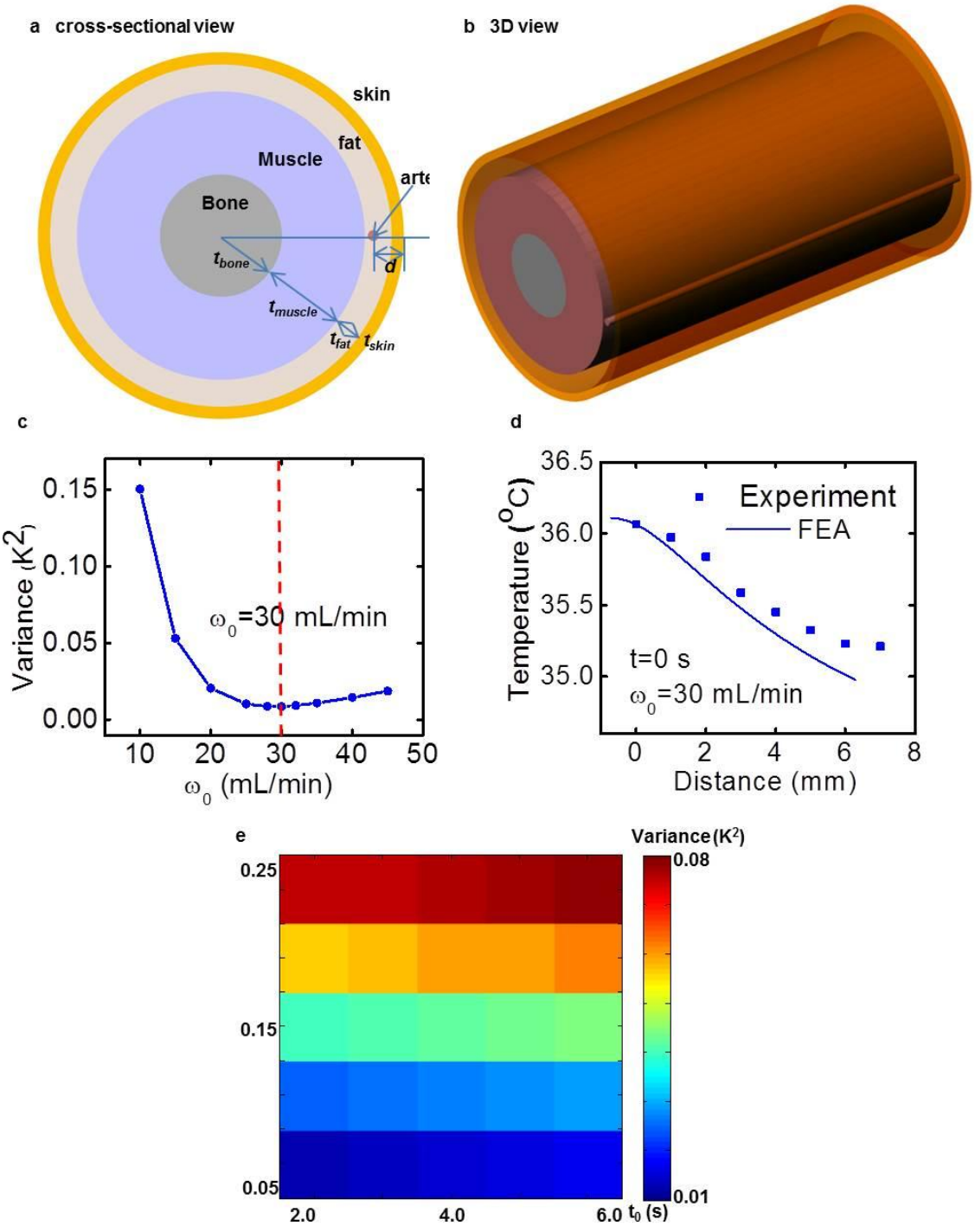

Figure S25: Schematic illustration of the thermal conduction model that determines the blood flow rate during occlusion. (a) Cross-sectional view and (b) three-dimensional view of the wrist model; (c) Temperature variance of FEA and experiment versus the baseline flow rate;

(Fig. S25 continued) (d) Experimental results of the steady-state temperature as a function of the distance from the artery, as compared to the FEA calculations using the baseline flow rate of 30 mL/min; (e) Distribution of temperature variance in the space of parameters, α and $\tau 0$, during stage II of occlusion.